Quantum interfaces based on single photons from parametric down-conversion

Dissertation
zur Erlangung des Grades
des Doktors der Naturwissenschaften
der Naturwissenschaftlich-Technischen Fakultät II
– Physik und Mechatronik –
der Universität des Saarlandes

von

José M. Brito Rozas

Saarbrücken
2016

Tag des Kolloquiums: 04.04.2016

Dekan: Univ.-Prof. Dr.-Ing. Georg Frey

Mitglieder des Prüfungsausschusses:

Prof. Dr. Frank Wilhelm-Mauch
Prof. Dr. Jürgen Eschner
Prof. Dr. Christoph Becher
Dr. Ettore Bernardi

Abstract

In the recent years a technological revolution is underway: transmission and processing of quantum information will change the ways the human beings handle and process information. For this, the implementation of a quantum communication network where quantum states from different systems are distributed over long distances is necessary.

In this thesis we present a series of experiments for interfacing different quantum systems using heralded photons generated by spontaneous parametric down-conversion (SPDC). We explored the composite functioning of SPDC with quantum frequency conversion (QFC) and a single trapped $^{40}Ca^{+}$ ion. While trapped ions are a paradigmatic platform for information processing and storage, frequency conversion of photons into telecommunication band expands the possibilities of these systems for long-haul quantum communication, representing altogether a set of powerful tools for the implementation of an atom-photon quantum network.

In particular, we present the doubly-heralded absorption of SPDC photons by a single ion, a set of measurements featuring a SPDC-QFC interface to demonstrate the preservation of quantum properties of SPDC in the telecom band, and furthermore its use for heralding in the telecom O-band the absorption of a single SPDC photon by a single ion. Finally, we demonstrate the absorption by a single ion of a photon generated by an optical parametric oscillator (OPO) SPDC source whose heralds are generated directly in the telecom E-band.

Zusammenfassung

In den letzten Jahren ist eine technologische Revolution Im Gange: Die Übermittlung und Verarbeitung von Quanteninformation wird den Umgang und die Verarbeitung des Menschen mit Informationen verändern. Hierfür ist die Implementierung eines Quantenkommunikationsnetzwerks, in dem Quantenzustände von verschiedenen Systemen verteilt werden, notwendig.

In dieser Arbeit wird eine Reihe von Experimenten zur Kopplung verschiedener Quantensysteme vorgestellt. Es wird die Kombination von angekündigten Einzelphotonen, welche durch spontane parametrische Abwärtskonversion (SPDC) hergestellt werden, mit Quanten-Frequenzkonvertern (QFC) und einzelnen $^{40}Ca^{+}$ Ionen untersucht. Während gefangene Ionen eine etablierte Plattform zur Speicherung und Verarbeitung von Informationen darstellen, eröffnet die Frequenzkonversion in das Telekommunikationsband die Möglichkeit, diese Systeme zur langreichweitigen Quantenkommunikation zu nutzen. Damit steht ein leistungsfähiges Werkzeug zur Implementierung eines Atom-Photon-basierten Quantennetzwerkes zur Verfügung.

Im Besonderen zeigen wir die doppelt-angekündigte Absorption von SPDC-Photonen durch ein einzelnes Ion, eine Reihe von Messungen einer SPDC-QFC-Schnittstelle, um die Erhaltung der Quanteneigenschaften bei der Konversion der SPDC-Photonen in das Telekommunikations-O-Band nachzuweisen, sowie die Eignung der konvertierten Photonen, die Absorption eines einzelnen SPDC-Photons durch ein einzelnes Ion anzukündigen. Zuletzt zeigen wir die Absorption eines Photons, das durch einen optischen parametrischen Oszillator (OPO), welcher als SPDC-Quelle betrieben wird, und dessen Partner direkt im Telekommunikations-E-Band erzeugt wird, durch ein einzelnes Ion.

Resumen

En los últimos años una revolución tecnológica está en curso: la transmisión y procesamiento de información cuántica cambiará las formas en que los humanos manjean y procesan la información. Para este fin, la implementación de una red de comunicación cuántica en la cuál estados cuánticos de diferentes sistemas son distribuidos es necesaria.

En ésta tésis se presentan una serie de experimentos para la interfáz de diferentes sistémas cuánticos usando fotones generados a través de conversión espontánea paramétrica descendente (SPDC). Se ha estudiado el funcionamiento conjunto de SPDC con conversión de frequencias cuántica (QFC) y un ión de $^{40}Ca^{+}$ individual atrapado. Mientras que lo iones atrapados son una plataforma paradigmaticca para el procesamiento y almacenamiento de información, la conversión de frequencia de fotones a la banda de telecomunicaciones amplía las posibilidades de estos sistemas para comunicación cuántica a largas distancias, representando en conjunto una serie de poderosas herramientas para la implementación de una red cuántica atomo-fotón.

En particular, se presenta la absorción doblemente anunciada de fotones SPDC por un ión dinividual, un set de mediciones protagonizadas por una interface SPDC-QFC para demostrar la conservación de propiedades cuánticas de SPDC en la banda de telecomunicaciones y además su uso para el anuncio en la banda O de telecomunicaciones de la absorción de un fotón individual SPDC por un ión individual. Finalmente, demostramos la absorción de un fotón SPDC generado por un oscilador óptico paramétrico por un ión individual, anunciado por un fotón directamente generado en la banda E de telecomunicaciones.

Contents

Introduction

Since the invention of the laser, development of scientific advances and their applications in the field of optics has transformed society. In the recent years, a technological revolution is underway: transmission and processing of quantum information might change the ways the human beings communicate, handle and process information. This revolution has a long-standing story behind it, but essentially rests on fundamental principles of quantum mechanics whose paradoxical behavior has challenged some of the brightest minds of our time [1, 2, 3]. The essence of this technology is not other than the use of a quantum bit of information, or qubit [4], which is represented by a basic two-element basis quantum-mechanical superposition state. The vision of our research is the development of a quantum communications network able to transmit and process qubits in an analog way to a classical communications network, but which addtionally benefits from the computational power of quantum information processing [5, 6]. As everything in life, it is not only sugar sweet: for its implementation a series of issues have to be addressed related to the vulnerability of quantum states under interaction with the environment (decoherence) and the impossibility of generating copies of a quantum state, which are natural drawbacks compared to its classical analog [7, 8, 9].

A number of different quantum systems are possible candidates for composing the first full-working quantum network: atomic clouds, single ions, artificial atom-like systems, superconducting qubits, etc. However, since there is no single quantum systems that meets all the required criteria, the most likely approach is the use of a hybrid combination of different quantum systems, taking advantage of the best properties of each system into a composite realization. This is the main topic of study of the present doctoral work, focused on the use of atoms (single ions) and heralded single-photons (Spontaneous Parametric Down-conversion) as building blocks of a quantum network where single ions represent the nodes and photons play the role of channels of the network. Experiments involving the combination of these two-counterparts (interfaces) represent advances in the field of quantum information processing although due to physics underlying these phenomena, they represent as well a contribution to the study of fundamental physics in the field of quantum optics.

Motivation

A key resource of an interface is the possibility of generation and distribution of entanglement between nodes of a network. In protocols like DLCZ (Duan, Lukin, Cirac, Zoller) [10], entanglement among nodes is produced by projective measurement of photons emitted by the atom. However, a powerful alternative is swapping of entanglement by photon absorption as proposed by Sangouard [11] which outperforms the DLCZ approach. Moreover, an extended approach for photon pairs by Spontaneous parametric down-conversion (SPDC) was proposed in [12], which profits from of

high-generation rates, wavelength flexibility and high-quality entanglement of SPDC sources.

A series of experiments carried out by several groups have been pointing towards entanglement distribution using different interfaces, some remarkable examples are described briefly. Basic network experiments have been implemented using Rubidium atoms in the group of G. Rempe [13, 14]. A photonic interface using frequency conversion has been shown by Tanzilli in the group of N. Gisin [15] whose group has also shown quantum teleportation using SPDC photons and solid-state memories [16]. Additional interesting experiments targeting atomic and solid-state memories have been shown in the group of H. de Riedmatten [17].

During the present thesis, we focus on experiments that permit the use of entangled photons pairs and allow for entanglement distribution by controlled single-photon absorption by single-trapped ions. Moreover, we are interested in analyzing the perspectives of long-haul transmission capabilities of photonic channels, as necessary for a quantum network scenario.

Previously in our group a series of experiments including controlled emission and absorption of SPDC photons by the ion have been realized. As a first step, the absorption of photons from a bulk SPDC source by a $^{40}Ca^{+}$ ion was performed by looking at quantum jumps [18] as a first indication of their interaction. Furthermore, absorption of heralded SPDC photons was used to show the single photon absorption by correlating the quantum jumps at the ion with detected heralds [19, 20]. By using a similar scheme, Huwer et al remarkably showed the entanglement of a SPDC polarization-entangled pair by using the polarization dependence of the photon absorption at the ion, performing for this full tomographic reconstruction of the photons states [21, 22]. Additionally, the ion apparatus has been used as single emitter [23, 24], making possible the controlled emission and further absorption by a second ion [25].

Since the implementation of a narrow-band 729 nm laser and RF-excitation for qubit transitions in our ion-trapping apparatus [22], a new generation of experiments has been realized. These allow one to prepare coherently the internal state of the ion for photon absorption and state read-out, opening new ways for studying internal state mapping and information transfer. These are key aspects on the way to a single-photon single-atom quantum network, since high-fidelity protocols that permit transferring information from flying qubits into stationary qubits and vice-versa are necessary conditions for their implementation. Recently, Kurz et al have shown that it is possible to implement a protocol for mapping a photonic state transfer onto the ion, and moreover it has been shown that these protocols can be extended into photon emission [26]. Also, controlled absorption of photons has allowed to observe interference effects of the internal states of the ion in absorption and emission, and enhanced phase measurements [27, 28]. These experiments have paved the way for further experiments where true single-photons states are mapped into internal states of the ion. Experiments described in this thesis form part of these advances.

Overview of the thesis

Interfacing experiments with photonic and atomic systems is the main topic of the present thesis, this makes the chapters concerning the experimental results (2, 3, and 4), the core and most important part of this work. Three photon-to-ion interaction experiments featuring Spontaneous-parametric down conversion photon and a single trapped ion have been performed, plus additional measurements for a SPDC to quantum-frequency-conversion photonic interface (SPDC+QFC). In

total, five independent experiments are presented.

The first chapter corresponds to the doubly-heralded single-photon absorption by a single atom, where single heralds emitted by the ion upon absorbing a SPDC photon are detected and used to signal a successful absorption process. Heralds detection is very relevant for our schemes since with its use fidelity is no longer limited by success probability, for instance for state transfer, entangling operations, among others [29, 30]. Additionally, an efficient method for decreasing the background of the correlations was applied by inspecting the final state of the ion after an experimental run. Furthermore, this experiment is a relevant step towards the realization of a heralded photon-to-atom quantum state transfer protocol using SPDC, where the polarization state of an polarization-entangled SPDC photon is mapped onto the ion using a superposition state sensitive to the polarization of the incoming photon.

Following, two experiments for exploring the compatibility of photon-to-atom systems with long distance communication were realized. In these experiments, the absorption of an SPDC photon by a single trapped ion was heralded in the telecommunications band of the electromagnetic spectrum, where fiber transmission losses are significantly lower compared to typical optical-memory wavelengths. In these two experiments two approaches for making compatible quantum systems with long distance communications are studied. The first (Chapter 3) corresponds to the use of quantum frequency conversion, i.e. adding an intermediate wavelength translation step. Several additional measurements are performed between the combined SPDC+QFC interface, including single-photon characteristics, energy-time entanglement and telecom-signal multiplexing. The second (Chapter 4) corresponds to the use an alternative ultra-bright highly-tunable photon source based on resonant-cavity enhancement whose photons are emitted directly at telecom wavelengths.

Finally, additional information on the experiments is presented in the appendices for the interested reader. A brief revision of the ion's efficiency for 854 nm photon absorption is presented, based on analysis of the interaction experiments. Moreover, a project of a high-brightness photon source based in a PPKTP waveguide crystal performed during the present doctoral work is presented. Advantages and drawbacks of this technique are discussed. Concluding, journal versions of the experimental results presented in in this thesis are attached as supplementary material.

Chapter I

Experimental tools

In this chapter an introduction to the tools used for our experiments is presented: a single $^{40}Ca^{+}$ ion trapping apparatus, a SPDC heralded single-photon source and a quantum frequency conversion setup. SPDC photon source and quantum frequency conversion set-ups are adapted to work altogether resonantly at the wavelength of the $D_{5/2} \rightarrow P_{3/2}$ transition in $^{40}Ca^{+}$ ion. These setups are operated independently and can be used for relevant stand-alone experiments, however the main goal of this thesis and of our researching interests is to explore interfacing possibilities among them as fundamental components of a quantum network were photonic transmission channels and atomic nodes are combined.

I.1. Ion traps

Ion traps are the subject of several PhD theses in our group which cover construction, characterization and experiments with single $^{40}Ca^{+}$ ions, we thus refer to them briefly, explaining only the most relevant details for our consideration.

Ion traps are a paradigmatic platform for quantum mechanics experiments. Single trapped ions represent almost ideal quantum systems which not only allow one to study fundamental physical phenomena but also offer a range of important technological applications, one significant example being high-precision atomic clocks [31, 32]. Furthermore, high-fidelity gates, long storage times and single qubit addressing possibilities have made trapped ions one of the most robust candidates for the implementation of quantum computers and simulators [33, 34, 35, 36] and particularly attractive as quantum processors [37].

Their development started with the construction of devices for mass spectrometry using oscillatory electromagnetic fields whose further development lead to the construction of traps allowing for 3-dimensional confinement of ions (1959). For their contributions W. Paul and G. Dehmelt were awarded the Nobel Prize in physics (1989). A few yeas later, I. Cirac and P. Zoller (1995) proposed trapped ions as an ideal system for implementing Shor's quantum factorization algorithm (1994), attracting attention and boosting their development as tools for quantum computation purposes [6, 38].

Ion traps works as an electromagnetic analog of a classical rotating-saddle experiment [39]. A static two-dimensional well-potential will not confine a particle in three dimensions, although this can be achieved by a rotating it around its axis. Analogously for an ion, an fast-oscillatory electromagnetic field with given parameters can be used for confining it.

In our laboratory we use a linear Paul-trap originally designed in R. Blatt's group [34], where the ion is confined in a plane (radial direction) with an oscillatory quadrupole field created using four

blade electrodes, with two opposing each other diagonally and with opposite charges, while in the axial direction, a static potential is applied (end tips) as shown in Fig. I.1(a). This geometry allows for trapping several ions in a string and eases the optical access for single-ion laser addressing [40]. Blade electrodes are driven to a high-voltage V_{RF} at a radio frequency ω_{RF} at a distance r_o from the center while the static potential with a high voltage V_s at a distance d_o. Close to the trap center the potential described by its radial and axial parts is written as

$$V_{\text{radial}} = \frac{V_{RF}}{2r_0^2}(r_0^2 + x^2 + y^2)\cos(\omega_{RF}t) \tag{I.1}$$

$$V_{\text{axial}} = \frac{V_s\alpha}{2d_0^2}(2z^2 - x^2 - y^2) \tag{I.2}$$

where α is numerical factor relative to the trap geometry. When fast oscillations caused by V_{radial} (micro-motion) are averaged, the ion is trapped stable in an effective harmonic potential where it oscillates at a lower frequency (macro-motion) [41]. By applying laser cooling, the oscillations of the ion in the pseudo-harmonic potential are reduced to close-to-zero energy of its motion states, where it is described by a 3-dimensional quantum mechanical harmonic oscillator [42]. Thus, the single ion Hamiltonian is

$$H_i = h\omega_i(a_i^\dagger a_i + \frac{1}{2}) \qquad (i = x, y, z) \tag{I.3}$$

whose energy eigenstates are $|n_i\rangle$, with eigenenergies $h\omega_i(n_i + 1/2)$.

Setup

As mentioned, our ion trapping apparatus corresponds to linear Paul-type traps where single $^{40}Ca^+$ ion are trapped. An important feature is the optical arrangement involving two custom-made high-numerical aperture laser objectives (HALOs) placed at opposite sides along one of the axes of the trap, inside the ultra high-vacuum chamber that contains it. These objectives were set to enhance spatial mode overlap for absorption and collection of photons and have a numerical aperture (NA) of 0.4 covering about 4% of the solid angle each. Our trap with their respective HALOs is shown in Fig. I.1(b). Their working distance is about 12 mm that can be adjusted by xyz-translational stage (Attocube) depending on the wavelength of interest. Magnetic field is controlled by three pairs of coils along every axis of the trap. A higher current is applied in one direction to define the quantization axis (set by the field direction) for 2.8 gauss, while coils in the other directions compensate other static magnetic fields such as the earth's. Two such traps are situated in our laboratory with one meter of separation, allowing for combined-use experiments [23, 25].

Relevant transition of the $^{40}Ca^+$ ion are shown in Fig. I.2. For each of these transitions (397 nm, 866 nm, 850 nm, 854 nm), a narrowband frequency-stabilized extended-cavity laser diode systems is available (Toptica, <300 kHz bandwidth). Their stabilization is based on a Pound-Drever-Hall locking scheme that uses low-finesse cavities referenced to an 852 nm laser, which is itself locked to a cesium vapor reference (transfer-lock, [43]). Additionally, a 729 nm ultra-narrowband laser (4 kHz bandwidth) that uses an ultra-high-finesse cavity as a reference is used to address the $S_{1/2} \rightarrow D_{5/2}$ dipole-forbidden qubit transition [22].

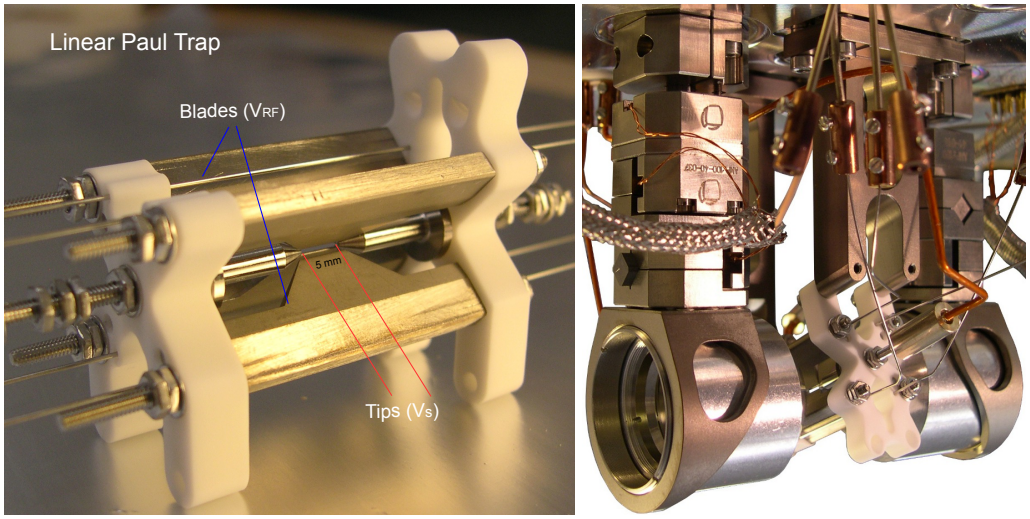

(a) (b)

Figure I.1: (a) Linear Paul trap. (b) Trap with two High-numerical Aperture Laser objectives (HALOs). In the experiments presented in this thesis one of the HALOs is used for focusing 854 nm SPDC photons onto the ion and both of them are used to collect 397 nm fluorescence or 393 nm photons.

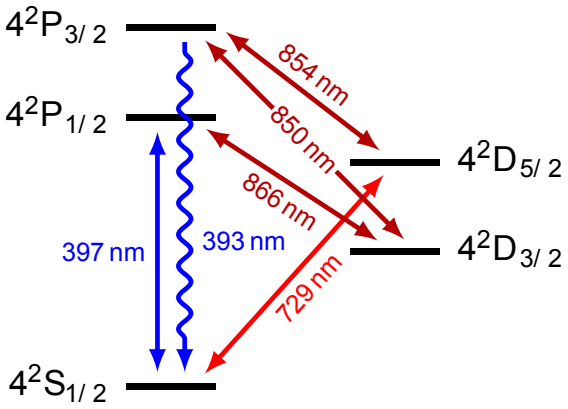

Figure I.2: Relevant levels in $^{40}Ca^{+}$ ion. 397 nm and 866 nm lasers are used for Doppler cooling and fluorescence detection. 854 nm laser is used for state preparation and re-pumping, and 729 nm narrowband laser is used for coherent state preparation.

Acousto-optic modulators (AOMs, Brimrose) are used as shutters and for fine frequency detuning (up to 200 MHz) of the lasers, whose control is performed in the RF regime assisted with a hardware-based control unit. These are HYDRA (I/II) units, a pulse sequencer based on direct digital synthesizers (DDS) controlled by independent field programmable gate arrays (FPGA). (Signadyne, [44]). With its latest version, multiple channel parallel operations synchronized down to 1.25 ns are processed while for detection an input resolution of 320 ps is possible. These allow for high precision driving of laser sequences for preparation and control of the trapped ion while

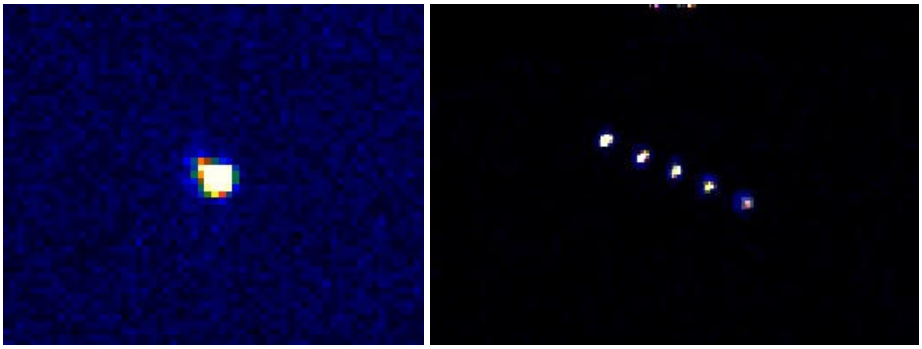

(a) (b)

Figure I.3: (a) A single trapped $^{40}Ca^{+}$ ion. (b) A five ions string.

simultaneously synchronized photon detection is performed. A picture of trapped ions using our experimental apparatus is shown in Fig. I.3, captured with a low-noise Electron Multiplying CCD camera (EM-CCD, Andor).

I.2. Spontaneous Parametric Down-conversion

In this section we give a basic insight on spontaneous parametric down-conversion (SPDC or PDC) and its use for the generation of ion-resonant photons

Spontaneous parametric down-conversion is a second-order non-linear process that can be understood as the conversion of a pump photon into two photons of lower frequency after interacting with a non-linear medium. This phenomenon was observed for first time in 1967 [45] and since then has become a powerful tool for photonic experiments. Created photons usually called signal and idler photons are strongly correlated and can be used as source of entangled two-photon states. This has been used for more than 20 years for testing Einstein-Podolsky-Rosen experiments using energy-time of polarization entanglement [1, 46, 47].

Theoretical considerations

Interaction between an electric field with a non-magnetic material is described in terms of its polarizability P,

$$P_i = \epsilon_0 \chi^{(1)}_{ij} E_i + \epsilon_0 \chi^{(2)}_{ijk} E_i E_j + \epsilon_0 \chi^{(3)}_{ijkl} E_j E_k E_l + \ldots \tag{I.4}$$

with ϵ_0 the vacuum permitivity and $\chi^{(n)}$ the non-linear susceptibility tensor of order n. SPDC is a non linear process of the second order, which is determined by the strength of $\chi^{(2)}_{ijk}$, characteristic of each material. It is analog to a frequency conversion process but where the input fields are a strong pump beam and vacuum field, thus having a low efficiency compared to classical non-linear

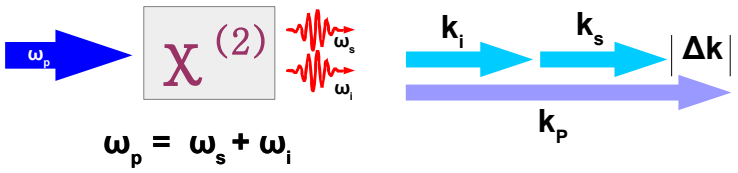

(a) (b)

Figure I.4: Phase-matching conditions: (a) Conservation of the energy for frequencies of pump, signal and idler modes (b) Poling of the nonlinear crystal Λ is reversed periodically to the momentum mismatch $\Lambda = \frac{2\pi}{\Delta k}$.

processes. In this process the conservation of energy demands

$$\omega_p = \omega_s + \omega_i \tag{I.5}$$

where $\omega_{p,s,i}$ are the frequencies of pump, signal and idler respectively. Additionally the momentum conservation must be also satisfied but the birefringence in the medium induces a momentum mismatch Δk for the signal and idler fields such that the momentum conservation is written

$$\mathbf{k}_p = \mathbf{k}_s + \mathbf{k}_i + \Delta\mathbf{k} \tag{I.6}$$

These are the phase-matching conditions, illustrated in Fig. I.4. The output field intensity is proportional to $L^2\text{sinc}^2(\Delta k L/2)$ which drops as a consequence of the dephasing produced by the momentum mismatch. However, reversing periodically the non-linear coefficient of the medium one compensates this effect, this is called quasi phase matching by periodic poling ($\Lambda = \frac{2\pi}{\Delta k}$). This also compensates for walk-off of the different modes, allowing for collinear photon generation of signal and idler modes [48, 49].

A general form for photon state for SPDC is calculated using the interaction picture [49].

$$|\Psi(t)\rangle = U(t)\,|\Psi(0)\rangle = \exp\left(-iH_I t/\hbar\right)|\Psi(0)\rangle \tag{I.7}$$

where the interaction Hamiltonian of the non-linear process for the electromagnetic field

$$H_I = \frac{1}{2}\int d^3\mathbf{r} E_i \int dt_1 dt_2 \chi^{(2)}_{ijk} E^\dagger_j E^\dagger_k \tag{I.8}$$

and the initial state, given by the classical state of the pump (α_p)and vacuum for signal and idler.

Using first order Taylor expansion for the quasi phase matching conditions, the two-photon state obtained by the time evolution for narrowband pumping can be written as

$$|\Psi\rangle_{SPDC} = |0_s, 0_i\rangle + \zeta \int d\omega_s d\omega_i V_p \delta(\omega_s + \omega_i - \omega_p)\phi(\omega_s)\,|\omega_s, \omega_i\rangle \tag{I.9}$$

where ζ is a normalization constant related to the conversion efficiency, V_p the pump amplitude and

$$\phi(\omega_s) \propto \exp(-iL\Delta k/2)\mathrm{sinc}(L\Delta k) \tag{I.10}$$

describes the spectral characteristics of the signal and idler fields.

Heralded single-photon source

A more general description of the parametric conversion process where signal and idler fields are created is described by

$$\hat{H}_I = i\hbar\chi\hat{a}_s^\dagger\hat{a}_i^\dagger + H.c. \tag{I.11}$$

where $a^\dagger$ are the creation operators for of the respective fields and χ is a parameter of the pump field. For the time evolution (I.2) in the low gain regime $|\eta| = |\chi t| \ll 1$ leads to an state with a low number of photons per mode

$$|\Psi(t)\rangle \approx (1 - |\eta|^2/2)\,|0\rangle + \eta\,|1_s, 1_i\rangle + \eta^2\,|2_s, 2_i\rangle \tag{I.12}$$

where the probability of generation of higher order is decreased by the low efficiency of the process (η^n). By detecting one photon in the signal mode, the state is projected into

$$\langle 1_s|\,|\Psi(t)\rangle = (1 - |\eta|^2/2)\,\langle 1_s|\,|0_s\rangle\,|0_i\rangle + \eta\,\langle 1_s|\,|1_s\rangle\,|1_i\rangle + \eta^2\,\langle 1_s|\,|2_s\rangle\,|2_i\rangle + \ldots = \eta\,|1_i\rangle \tag{I.13}$$

which is a single-photon state for the idler mode. At low pump powers higher order modes do not play an important role and it has been shown experimentally by measuring anti-bunching that for SPDC good quality heralded single-photon states is reached [50, 51].

I.3. SPDC source setup

Our photon source is based on SPDC for degenerate narrowband polarization-entangled photon pairs generation. As mentioned before the source has been designed for resonant interaction with the $^{40}Ca^+$ ion. For this purpose frequency stabilization and spectral shaping have been implemented, which guarantees emission at the correct resonant wavelength and the correct bandwidth of the target transition. For interactions experiments, the 22 MHz $D_{5/2} \rightarrow P_{3/2}$ transition of the ion at 854 nm has been chosen. A scheme of the experimental set-up is shown in Fig. I.5. This source has been designed by A. Haase and N. Piro and its construction and characterization is described in detail in [20], published in journal format in [52, 53]. Its main characteristics and complementary characterization measurements performed during the development of this doctoral work are described below.

Non-linear Crystal

For SPDC generation, a periodically poled $KTiOPO_4$, Potassium titanyl phosphate crystal (PPKTP) is used. Type-II quasi-phase matching conditions allow for collinear creation of photons with perpendicular polarizations (V→H+V) for polarization entangled photons pairs. Crystal dimensions

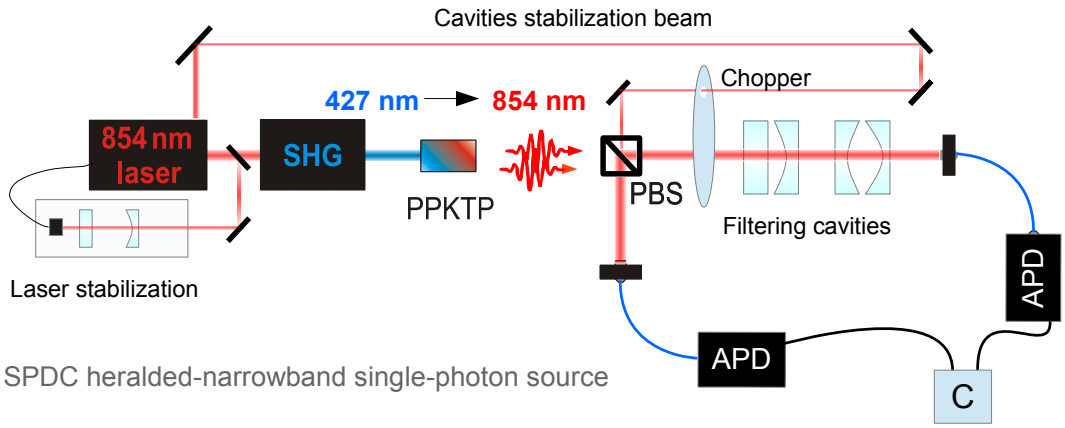

Figure I.5: SPDC photon source setup. Broadband degenerate photons at 854 nm are created by SPDC in a PPKTP non-linear crystal by continuous pump at 427 nm. Pump field is provided by a Toptica SHG-pro module consisting of an amplified laser diode at 854 nm doubled in frequency into 427 nm using second-harmonic generation. Original laser emission is stabilized to a cesium reference using a transfer lock scheme [43]. Created photon pairs are split using a polarizing beam splitter (PBS). Transmission port of the PBS is connected to a two-cavities spectral filtering step used for selecting 22 MHz narrowband photons. Cavities are stabilized about 15% of the time using a probe beam alternated with photon transmission using a chopper. Photons for coincidence measurements are detected using avalanche-photodiodes (APDs, Perkin-Elmer) and time-stamps are recorded using a high-resolution Picoharp Unit (Picoquant, 4 ps).

are $20\times6\times1$ mm oriented along the y-x-z crystallographic axes. Two poling periods are imprinted in the crystal along its length: 14.03 µm for degenerate emission at 850 nm (25° C) and 14.63 µm for 854 nm (10° C) with a non-linear coefficient $d_{24} = \chi^{(2)}_{223}/2 = 7.6$ pm/V. According to our target transition, the latter poling option is used, for which temperature is set to 10° C with a precision better than 10 mK.

Pump

Photon pairs are generated by continuously pumping the non-linear crystal with a classical field. For emission at 854 nm, pump at 427 nm is provided by a Toptica SHG-pro module which consist of a laser diode at 854 nm whose emission is amplified to 500 mW using a tapered amplifier unit and doubled in frequency to 427 nm using cavity-enhanced second-harmonic generation (SHG), with a maximum output power of $\sim$ 60 mW. Original diode laser emission is stabilized to the transition wavelength using a transfer lock scheme intermediated by a 852 nm laser locked to a Cesium vapor cell reference as described in [43]. As the original diode laser is stabilized to the correct wavelength transition, degenerate SPDC 854 nm emission is performed at the same resonant wavelength. A probe 854 nm is further used to stabilize the spectral filtering unit at the same central wavelength fulfilling the same requirements.

Spectral filtering

The spectral filtering unit consists of two cascaded Fabry-Perot cavities. Two cavities of medium Finesse allow for strong spectral reduction from ~ 200 GHz down to 22 MHz without needing a high-finesse cavity. First cavity of 78 µm length and Finesse of 760 has a transmission bandwidth of $2.5{\cdot}10^3$ MHz while the second a Finesse of 649 and 22.5 MHz transmission bandwidth. Transmission through the cavities is about 90% which is achieved by a proper spatial mode-matching along the 600 mm of propagation, after which transmitted photons are fiber coupled with ~85% efficiency. Under normal conditions during the experiments performed in this thesis an overall transmission through the filtering system for SPDC photons including fiber coupling, cavities transmission and losses in the optics was about 30%. Stabilization is performed using a reference 854 nm probe beam which allows for filtering photons that are resonant with the ion transition. The reference beam is alternated with photon generation using a chopper with a 85:15 ratio driven at 15 Hz rotation frequency, which is long enough for the cavities to stay locked during the photon transmission period. The stabilization method uses high harmonics of the scanning piezo for the first cavity modulated at 50 kHz, while the second cavity is stabilized by creation of an error signal using the 20 MHz modulation of the diode laser, which is also used for the SHG cavity stabilization (Pound-Drever-Hall). Filtering cavities allow one to characterize the narrowband emission of the source, given by the transmission bandwidth of the filtering system, ~22.5 MHz. Coincidences detected between filtered triggering photons and their unfiltered partners are shown in Fig.I.6. An exponential time decay of 7±0.4 ns is observed, which results in 22.9 MHz spectral bandwidth, as expected from its design.

Furthermore, for illustration purposes, a normalized comparison between the measured broadband spectrum and the 22.5 MHz Lorentzian transmission bandwidth of the cavities is shown in Fig. I.7. As it is seen, most of the 173 GHz broadband emission is filtered out by the cavities system, meaning a big single counts reductions at the APDs. From this spectra, only $1.04 \cdot 10^{-4}$ of the total emission survives the spectral selection, without considering transmission losses (normalized). This way, 10^7 broadband single photons per second produced at maximum pump power are reduced to a few thousand counts after applying the filtering cavities.

Interaction with the Ca^+ ion.

For photon-ion interaction experiments, narrow-band photon generation rate is the most important figure of merit for the experiments presented in this thesis. Characterization of the source (as in Fig.I.6) resulted in a extrapolated maximum rate of 120 narrowband coinc./s (60 mW pump). Considering the coupling and transmission losses a maximum of ~ $4000s^{-1}$ resonant photon are available at the ion for absorption. These photons are fiber coupled from the reflected arm of the PBS in Fig. I.5 using a single-mode polarization maintaining fiber. It is important to note photons impinging on the ion are not filtered since the ion itself works as a filter and will not absorb photons outside of the Zeeman broadened $D_{5/2} \rightarrow P_{3/2}$ transition. However, filtering cavities are still employed for the opposite triggering arm since strong background produced by the remaining broadband photons shown in Fig. I.7 spoil the detection of the triggering photons. Since energy must be conserved (eq. I.2), partners of the heralded photons fulfill the same spectral requirements meaning coincidences correspond to 22 MHz photons, allowing to herald the absorption of the

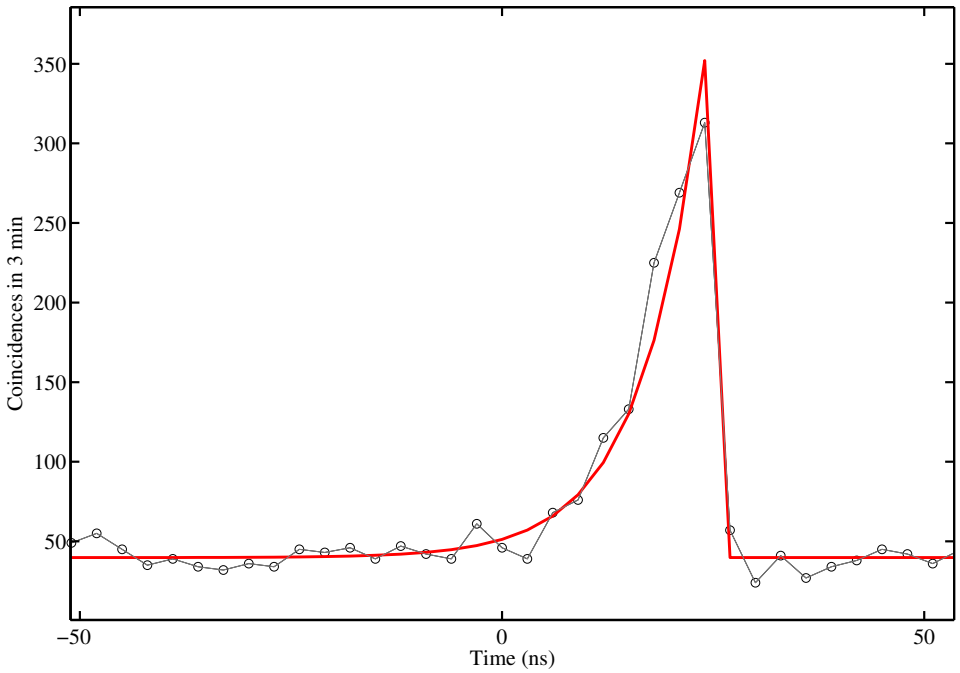

Figure I.6: Coincidences histogram of SPDC photon pairs at 854 nm. Long exponential decay corresponds to the ring-down time of the cavities, with time constant of 7±0.4 ns (22.9 MHz) fitted by the red solid line, while the steep slope is the jitter time of the APD (~ 600 ps).

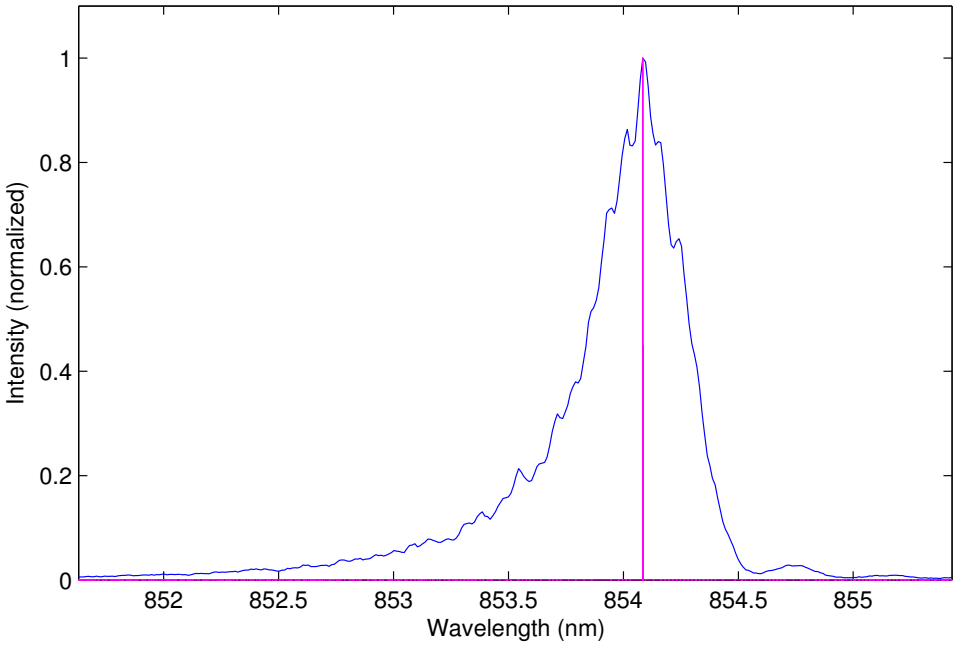

Figure I.7: Comparison of the spectra of SPDC 854 nm photons. Blue solid line shows a spectrum measurement of the broadband 854 nm photons (173 GHz, FWHM) while the magenta curve represents the 22 MHz transmission bandwidth of the filtering cavities.

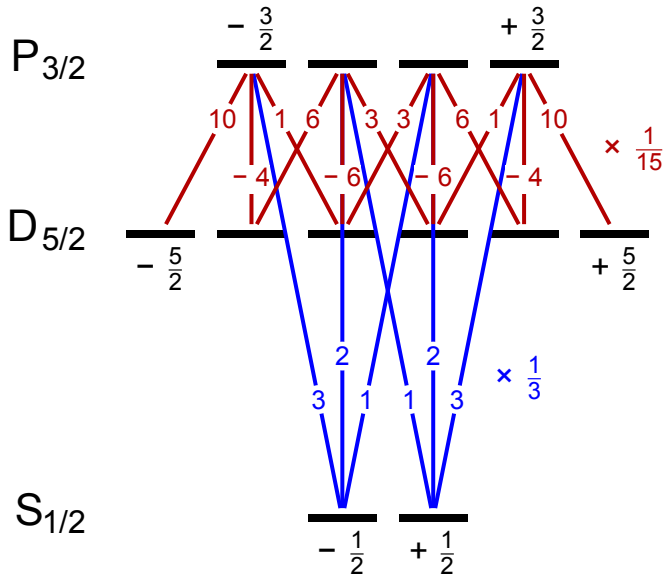

Figure I.8: Clebsch-Gordan coefficients (CGC) of the $S_{1/2}$–$P_{3/2}$, and $D_{5/2}$–$P_{3/2}$ transitions in $^{40}Ca^{+}$ ion relevant for interaction experiments with resonant SPDC source photons. CGC of a particular transition $j, m \rightarrow j'm'$ are calculated by multiplying the modulus of the respective number with the factor placed on the right and then taking the square root, with the respective sign [54].

absorbed photons [19]. In order to maximize the absorption of photons, the ion is prepared in the $|m = -\frac{5}{2}\rangle$ sub-state of the $D_{5/2}$ by coherent excitation using the narrowband 729 nm laser, where the absorption probability is maximum for this transition, as seen from the corresponding Clebsch-Gordan coefficients in Fig. I.8. This means polarization of the SPDC photons at the ion is set to σ^+ along the quantization axis, which for the experiments presented in this thesis is defined along the HALO axis for enhancing the focusing of the SPDC photons. After a source photon absorption the ion is excited into $P_{3/2}$ from where it decays with 94% probability into $S_{1/2}$ emitting a 393 nm photon. As shown further in this work, one can use either this single photon to herald the absorption or use an amplified uncoherent heralding by fluorescence emission.

Entanglement

Type-II phase-matching conditions determine the polarization correlation between pump and generated photons (V →H+V). If we split photon pairs using a non-polarizing beam splitter, the post-selected state on coincident detection corresponds to a Bell maximally-entangled two-photon state for the polarization

$$\left|\Psi^{(-)}\right\rangle = \frac{1}{\sqrt{2}}\Big(|H_s, V_i\rangle - |V_s, H_i\rangle \Big) \tag{I.14}$$

This was shown for first time by Kwiat et al [47]. As the crystal is birefringent, different propagation velocities for signal and idler modes causes time distinguishability of the photons that

spoils the entanglement. As in reference [47], this is normally tackled by placing an additional crystal with rotated-axis for compensating the birefringence or using a Sagnac-interferometer [55]. In our case, strong spectral selection by filtering compensates this effect (overlap of long 7 ns photons), allowing for high-quality entanglement. Tomography measurements by Piro show a fidelity for the mentioned $|\Psi^-\rangle$ state of 97.6% and a concurrence $C = 94\%$, [53]. Due to the reason just mentioned, polarization entanglement of broadband 854 nm pairs cannot be observed with the current setup, however as it is explained further in this thesis, we use an extended setup for observing energy-time entanglement of the broadband-photon pairs by Franson interference [56].

I.4. Quantum frequency conversion

Frequency conversion of light is a well known non-linear optical phenomenon which corresponds to nonlinear wave-mixing. Since the invention of laser it has been widely used for accessing light with exotic wavelengths . Three-wave mixing processes arise from the second-order non-linear susceptibility of equation I.2, in particular as second harmonic generation, sum frequency generation and difference frequency generation, depending on the additive phase relation between the input fields. Since they are second order non-linear effects the efficiency of these processes is low and typically phase-matching is required for their use. The interaction is described as

$$H_I \propto \chi^{(2)} \int d^3\mathbf{r} \hat{E}_1^{(+)}(r,t)\hat{E}_2^{(-)}(r,t)\hat{E}_3^{(-)}(r,t) + H.c. \tag{I.15}$$

which is initially a classical non-linear interaction, nevertheless as for parametric down-conversion a quantum mechanical treatment of the electromagnetic field shows that these processes work analogously for quantum states of light, called quantum-frequency conversion. A general theoretical treatment of this process is found in [49, 57]. In particular we can choose two quantum-mechanical fields fed by a strong classical field such that an input single photon state is turned into a frequency converted single-photon state, which is the interesting case for our experiments.

In the present thesis quantum frequency conversion has been used for converting our SPDC photons at 854 nm into the telecom band at 1310 nm using Difference Frequency Generation (DFG) such that

$$\frac{1}{854\text{ nm}} - \frac{1}{2453\text{ nm}} = \frac{1}{1310\text{ nm}} \tag{I.16}$$

which is fed by a strong pump at 2453 nm as shown in Fig. I.9. The implementation of the quantum frequency conversion used in the present work happened in C. Bechers laboratory and has been one of the main topics of A. Lenhard's PhD thesis. It is thus described here summarized. Design, implementation and characterization are described in detail in [58].

Experimental setup

The quantum frequency conversion setup is based on a single-pass conversion in a periodically poled lithium niobate waveguide crystal (PPLN). The high refractive index contrast of the ridge waveguide structure [59] provides high modal overlap of all involved fields, allowing for single-pass conversion. This step is crucial since high modal overlap is a prerequisite for high conversion efficiency. The chip has various polings for its waveguides, from 22.60 µm up to 22.85 µm period

in 50 nm steps, for phase-matching covering the whole telecom O-band. Pump beam is provided by a continuous wave optical parametric oscillator (OPO) tunable between 2311 and 2870 nm with output powers up to 1 W. After combining pump beam and single-photons in a dichroic mirror, they are focused into the waveguide with a single uncoated aspherical lens (Thorlabs, A220TM) as shown in Fig. I.9(b). Spatial modes of both have been designed for optimal coupling, where a 854 nm laser probe coming in the same path as the single-photons from the SPDC source is used for aligning and optimization of the conversion, including polarization adjustments. While the waveguide is capable of polarization independent guiding, the DFG process needs a fixed polarization state. A coupling efficiency of 84.2% at 854 nm and 38% at 2453 nm is reached, which includes transmission losses which affect strongly the pump beam (27%). We measure a maximum pump power of 280 mW inside the waveguide. After frequency conversion telecom photons are collimated and cleaned from residual light from the pump, broadband noise from parasitic nonlinear effects and also unconverted photons. This is done using a dichroic mirror and three band-pass filters, two 50 nm and one 12 nm (FWHM), with a total transmission of 37%. Furthermore, photons are coupled to a telecom fiber (SMF28) with an efficiency of 80% and detected with a superconducting single photon detector (SSPD, SingleQuantum, EOS X10) with a detection efficiency of 25% in continuous mode operation. This way, an overall conversion efficiency for the 854 nm field including losses and fiber coupling of 8% is measured.

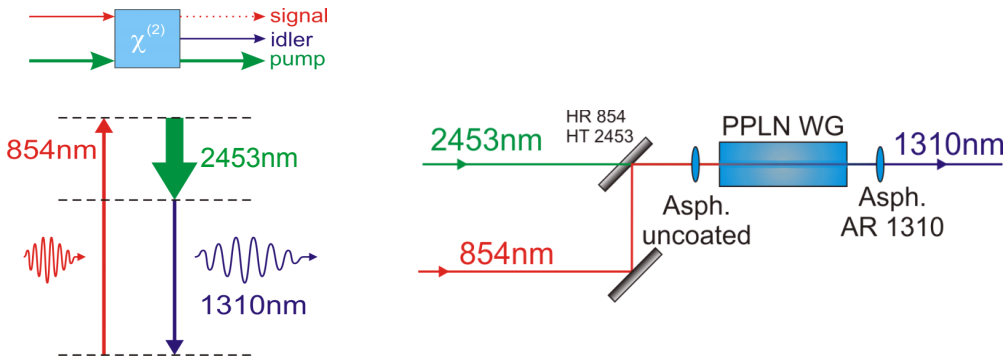

(a) (b)

Figure I.9: (a) Difference frequency generation: an incident photon at 854 nm is converted into a telecom 1310 nm photon in presence of a strong 2453 nm pump field. (b) Photons at 854 nm are overlapped with strong pump beam at 2453 nm into a PPLN waveguide crystal using a dichroic mirror and strong focusing using an aspheric lens. Output converted 1310 nm photons are collimated and separated from residual emission using passive filters

Chapter II

Doubly-heralded single-photon absorption by a single atom

A major goal in quantum technologies is the integration of quantum communication and information processing into quantum networks [5]. One promising approach is using single atoms and photons as nodes and channels of the network [14, 60, 25]. Single photons are able to transmit quantum information between different nodes of the network, while single atoms serve as high-fidelity, long-storage-time memories; single trapped ions, in particular, may additionally be used as quantum processors [61, 62, 37, 63]. In this context, the use of heralding photons for repeaters and memories schemes is very promising [64, 29]: successful entanglement transfer or information storage onto a single atom is signaled by the detection of a photonic herald emitted as a consequence of the process. The detection of such heralds permits one to discriminate successful events and thereby enables high-fidelity protocols, e.g. for photon-to-atom quantum state transfer [65, 30, 66] or distant ion entanglement [64].

Previously we have demonstrated the absorption of single SPDC photons in a single ion, signaled by the onset of fluorescence, i.e., by a quantum jump [19]: absorption of a photon excites the ion out of a metastable state into a fluorescence cycle, and a large number of emitted photons heralds the absorption event with near 100% efficiency. This method has also been used to herald single-photon interaction between two distant ions [25] and to manifest the polarization entanglement of a SPDC photon pair in single-photon absorption [21]. By generating fluorescence, however, the state of the ion after the single-photon absorption is not preserved, and transferred quantum information is lost. This limitation is overcome when a single scattered photon is used to herald the absorption process [67, 65, 66, 54, 68]. In [30] we implemented a specific protocol based on such heralding that enabled high-fidelity transfer of a photon polarization onto an atomic qubit, and that may also be used for photon-to-atom entanglement mapping [68]. While the experimental demonstrations so far were carried out with laser photons [30, 66], here we extend them to the absorption of single photons from an SPDC source, thus proving the feasibility of photon-to-atom quantum state conversion with our interface.

The principle of our single-photon-to-single-atom interface is as follows: a single trapped ion is exposed to a single resonant photon, generated via SPDC and heralded by its partner; successful absorption is heralded by the detection of a single Raman-scattered photon released as a result of the absorption. Coincident detection of the partner SPDC photon and the photon emitted by the ion marks doubly-heralded single-photon absorption by a single atom. Furthermore, we present a method for discriminating real absorption events from dark-count induced coincidences, tackling the main source of background. Additional perspectives for the detection of single heralds for

quantum-state-transfer using the discrimination method are also discussed. Elements presented in this chapter are also used further in this thesis for analyzing perspectives of similar experiments extended to long-distance communication using telecom photons. Main results presented here have been published in journal format in [69], on which this chapter is based.

II.1. Experimental setup

The experimental apparatus is shown in Figure II.1. Narrow-band heralded photon at 854 nm are created by spontaneous parametric down-conversion using the bulk source described in sec. I.3. The PPKTP crystal is pumped continuously with a 427 nm beam (Toptica, TA-SHG pro) stabilized to an atomic reference via a transfer lock method [70]. SPDC photons are further frequency stabilized to match the $D_{5/2}$-$P_{3/2}$ transition in the $^{40}Ca^{+}$ ion using spectral selection.

The two photons of a pair have perpendicular polarizations due to type II phase-matching. Photons are split by a polarizing beam splitter (PBS) to use them as a heralded single-photon source meaning polarization entanglement is projected out. As explained earlier this means a photon of the pair is used to signal the presence of its partner, which arises from the strong time correlation shared by them due to the SPDC process.

In this experiment, vertically polarized photons are coupled into a single-mode fiber and transmitted to the ion trap setup where their polarization is adjusted using waveplates ($\lambda/4$, $\lambda/2$) before sending them to the ion for absorption, while horizontally polarized partner photon detections are used as triggering signal.

In order to signal presence photons that may resonantly be absorbed by the ion, triggering photons are transmitted through two cascaded Fabry-Pérot cavities which mimic the $D_{5/2} \rightarrow P_{3/2}$ transition with 22 MHz transmission bandwidth and actively stabilized to resonance . This allows one to select triggers of only ion-resonant photons partners, strongly reducing the background produced by broadband SPDC emission ($\sim$ 200 GHz).

The single $^{40}Ca^{+}$ ion is trapped in a linear Paul-type trap, as described in sec. I.1. Two in-vacuum high numerical aperture laser objectives (HALOs, $NA = 0.4$) are used for efficient ion-photon coupling. They are placed along one of the axes of the trap, which in this case also defines the quantization axis (magnetic field direction, B in Figure II.1). While only one of the HALO's is used to focus the 854 nm SPDC photons onto the ion, both of them are used to collect the 393 nm absorption heralds, which are extracted using dichroic mirrors and furthermore detected by two photomultiplier tubes (PMTs, Hamamatsu). Including collection and detection efficiency, 1.86% of the emitted heralds are finally detected. Lasers used for ion cooling, pumping and state preparation are shown in Figure II.2.

II.2. Experimental sequence

The sequence runs at 401 Hz repetition rate and consists of several phases, as shown in Fig. II.3 The first step of the sequence corresponds to Doppler cooling where 397 nm and 866 nm laser light is applied onto the ion for 100 µs bringing the ion down to the Lamb-Dicke limit [22]. Subsequently, optical pumping is performed for 60 µs by continuous excitation with 729 nm and 854 nm light, bringing the ion into the $|m = -\frac{1}{2}\rangle$ Zeeman substate of the $S_{1/2}$ ground state after which the ion

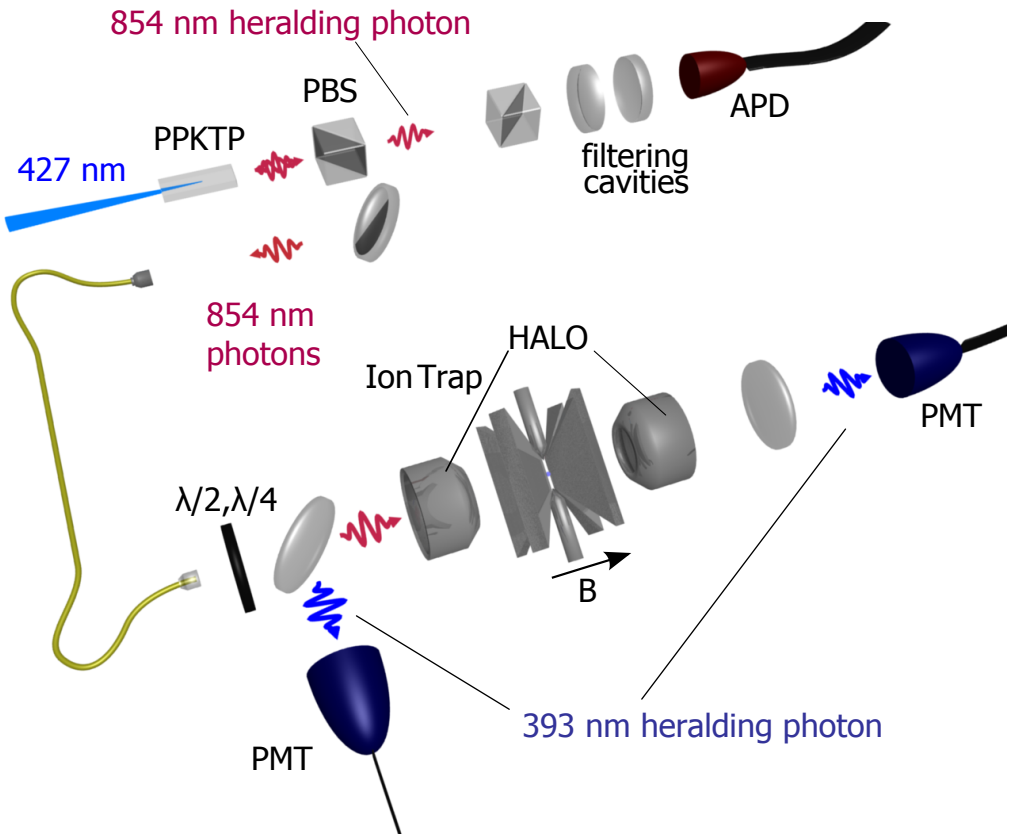

Figure II.1: Experimental setup for doubly heralded interaction. The top part shows the SPDC narrowband heralded photon source for resonant interaction with the $^{40}Ca^{+}$ ion at 854 nm. Lower part shows the ion trap setup consisting of a linear Paul trap equipped with two high numerical aperture laser objectives (HALOs). Photon pairs are generated by pumping a PPKTP non-linear crystal. Pairs are split using a polarizing beam splitter (PBS). Reflected photons are fiber coupled, polarization adjusted ($\lambda/4$, $\lambda/2$) an sent onto the ion for absorption using one HALO along the quantization axis (B), while transmitted partners is are sent through filtering cavities that mimic the $D_{5/2} \rightarrow P_{3/2}$ transition in the ion. 393 nm herald photons emitted by the ion upon an absorption are collected through both HALO's and detected with two photomultiplier tubes (PMTs, Hamamatsu). A coincidence between a 393 nm detection (PMTs) and an 854 nm triggering partner (APD) marks the doubly-heralded absorption.

is prepared for the absorption of 854 nm SPDC photons by coherent excitation to the $|m = -\frac{5}{2}\rangle$ substate of the $D_{5/2}$ metastable manifold (lifetime $\tau_D = 1.17$ s) with a 7 µs long π-pulse of a narrow-band 729 nm laser.

Subsequently, a detection window (gate) is open for 2 ms, while photons from the SPDC source are sent to the ion at a rate of $\sim 3500\ s^{-1}$ resonant photons. These photons are set to be σ^+ polarized in the ion's reference frame, thereby exciting the ion to the $\left|P_{3/2}, m = -\frac{3}{2}\right\rangle$ level, which corresponds to highest absorption probability between $D_{5/2}$ and $P_{3/2}$, as shown in Fig. I.8.

During the interaction phase, detection events of 854 nm photons on the APD and 393 nm photons on the PMTs are recorded and time-tagged for their later correlation analysis. After an

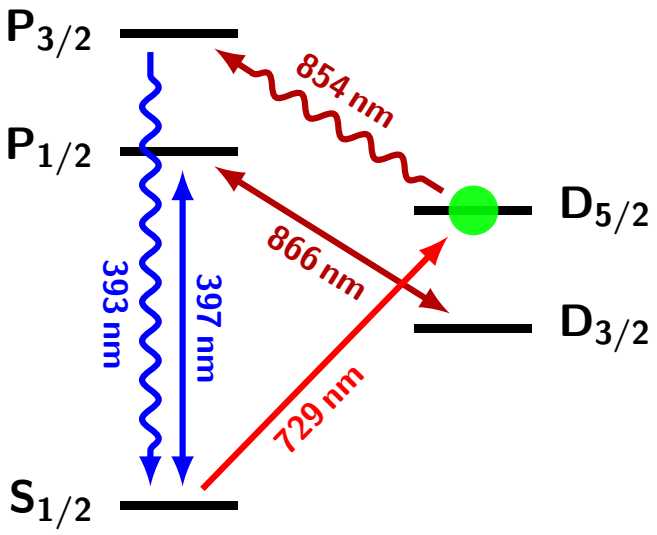

Figure II.2: Relevant level scheme of the $^{40}Ca^{+}$ ion. 397 nm and 866 nm lasers are used for cooling and fluorescence detection (discrimination). Lasers at 729 nm and 854 nm are used for for pumping and state preparation. The single ion is prepared into the $D_{5/2}$ metastable state for absorption of 854 nm SPDC photons ($D_{5/2}$-$P_{3/2}$ transition). Relevant absorption heralds are emitted at 393 nm.

experimental cycle of cooling, pumping, preparation, and interaction has finished, a series of 729 nm π-pulses are used for discrimination of the background, as explained in the background discrimination section. The effective single-photon-single-atom interaction time is 68% of the measurement time, resulting from the 2 ms interaction period per 2.5 ms cycle repetition, and reduced by the periodically applied stabilization of the cavity filters.

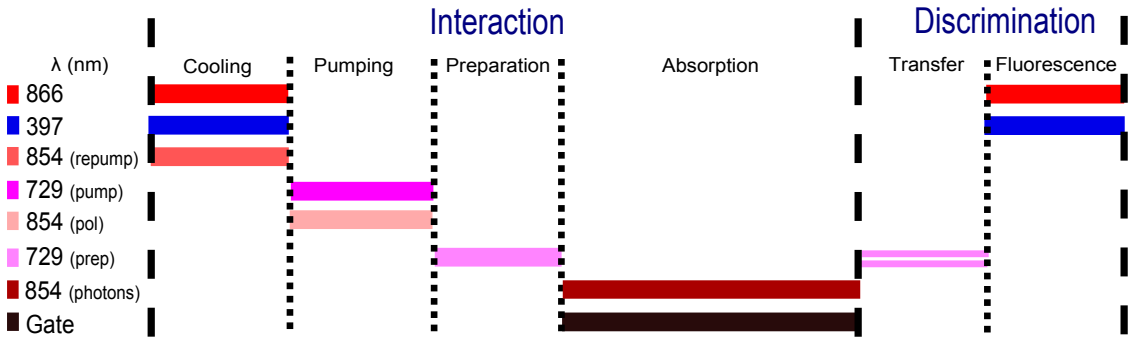

Figure II.3: Sequence for the doubly-heralded interaction. After the interaction phase, an additional part for background discrimination is included. See text for details.

After a successful absorption the ion decays from $P_{3/2}$ into the $S_{1/2}$ with 93.5% probability, scattering a blue Raman anti-Stokes photon at 393 nm (Fig. II.5(a)). This photon is the herald of the absorption process we are interested in. As mentioned earlier, two PMTs are used for collection through both HALO lenses. The SPDC partner photons that trigger the presence of

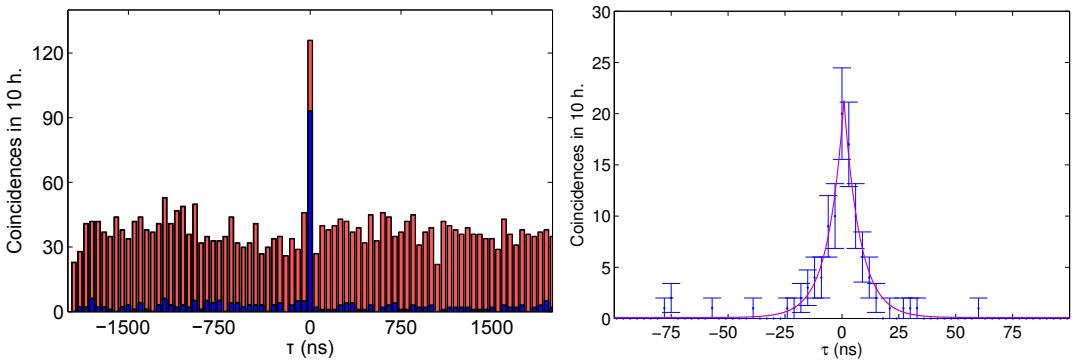

(a) (b)

Figure II.4: (a) Time correlation between photon heralds (854 nm) and absorption heralds (393 nm) with 50 ns binning and 10 hrs total measurement time (24 540 s interaction time). The peak at zero time delay corresponds to doubly-heralded single-photon absorption. The red and blue histograms show, respectively, the same data without and with additional background reduction. (b) Coincidence peak after background reduction and with 3 ns binning. The purple line represents the expected correlation function.

their absorbed partner are detected at the source's side using a single-photon avalanche photodiode (APD, Perkin-Elmer, ∼30% efficiency).

II.3. Experimental results

Time correlation histograms of the detections are shown in Fig. II.4. The peak around zero time delay corresponds to coincident photon detections on the APD and on one of the PMTs, and thereby marks doubly-heralded single-photon absorption. In the histogram of Fig. II.4(a) shown in red, 88.9(6.1) doubly-heralded absorption events (on top of 37.1(6.1) background counts) were detected in 10 hrs (24 540 s interaction time), meaning an average coincidence rate of $3.6 \cdot 10^{-3}$ per second. With an average background of 37.1 counts per 50 ns bin and Poissonian noise, the signal-to-background ratio (SBR) amounts to 2.4 and the signal-to-noise ratio (SNR) is 14.6 for this binning. Origin of background counts is explained in detail in the further section. As seen in Fig. II.4(b), a higher time resolution of the coincidence peak using 3 ns binning reveals a "tent-like" correlation peak: a symmetric double-sided exponential of about 7 ns 1/e-time originating from the temporal shapes of the two heralding photons, i.e. the shape of the 393 nm herald represents the lifetime of the $P_{3/2}$ state ($\tau_P = 7.2$ ns), while the shape of the 854 nm photons corresponds to the ring-down time of the filtering cavities as shown in figure I.6, which have been designed to match the same atomic spectral shape [52, 53]. The purple line in the plot represents the expected shape of the correlation function, showing very good agreement with the experimental findings.

II.4. Background reduction

In a further step of the data analysis, a discrimination method is included to reduce the most important source of background, i.e., events where a photon detection on the APD is coincident with a dark count on the PMT. Reducing the background is important since it decreases the measurement time for a target SNR or SBR and increases the fidelity of quantum state transfer schemes [30], by disregarding accidental coincidences that mimic a real absorption. Our method to achieve this is to measure the atomic state after the interaction and consider only those coincidence detections where the atom has indeed made the transition from $\left|D_{5/2}, m = -\frac{5}{2}\right\rangle$ to $\left|S_{1/2}, m = -\frac{1}{2}\right\rangle$. For this purpose, a series of laser pulses (altogether $\sim$ 300 µs) is included in the experimental sequence after the ion-photon interaction phase. First, as shown in Fig. II.5, two 729 nm π-pulses are applied to the ion. The first pulse takes the population from $\left|S_{1/2}, m = -\frac{1}{2}\right\rangle$ to $\left|D_{5/2}, m = +\frac{3}{2}\right\rangle$, which is used as an auxiliary metastable state. This population corresponds to the case where absorption of an 854 nm photon has happened. The following pulse transfers the population from $\left|D_{5/2}, m = -\frac{5}{2}\right\rangle$ to $\left|S_{1/2}, m = -\frac{1}{2}\right\rangle$, which corresponds to the case where no photon was absorbed. Subsequently, by switching on the cooling lasers for 250 µs, both cases are discriminated. The onset of fluorescence (ion turning bright) means that the ion remained in $D_{5/2}$ during the interaction, and no 854 nm photon was absorbed or that the ion returned to $D_{5/2}$ after the absorption. In the case where an absorption event happened, the ion will stay dark. By selecting only those 393 nm heralds that go along with a dark ion, we disregard coincidence events triggered by dark counts of the PMTs. While the coherent pulses, which in effect swap the bright and the dark result of the state measurement, do not seem to be strictly necessary for the state discrimination in this particular experiment, they are required in order to protect any quantum information transferred in the absorption event [30], and furthermore they are part of a more extended method which is explained below.

The result for the background reduction method as described so far is shown in Fig. II.4(a), where the blue bars correspond to the correlation measurement for the same data as the red bars, but with post-selection of the relevant events. The average background per bin is reduced from 37.1 to 2.3 events, a 16-fold improvement of the SBR, which translates into a 4.1-fold increase of the SNR. After applying the background reduction as described, there are still three cases which account for most of the remaining background counts, namely failed initial state preparation in $D_{5/2}$, failed $D_{5/2} \rightarrow S_{1/2}$ transfer (pulse 2 in Fig. II.5) before the state detection, and spontaneous decay from $D_{5/2}$ to $S_{1/2}$. Since in these cases the ion will be in $D_{5/2}$ (i.e., dark) during the state-selective fluorescence phase, they will be counted as successful absorptions events when they coincide with a double-herald detection. For the particular measurement of Fig. II.4 these "false positives" are not critical, as verified by the low observed background (2.3 events for 50 ns bins, or 0.14 events for 3 ns bins, as in Fig. II.4(b)). Nevertheless, discussion about the background reduction and analysis including a way to correct for preparation pulses error is presented further.

II.5. Efficiency considerations

Although HALO lenses are used to enhance absorption and collection of photons, main losses still stem from a poor photon-atom spatial mode overlap at the ion side. In this section we look at

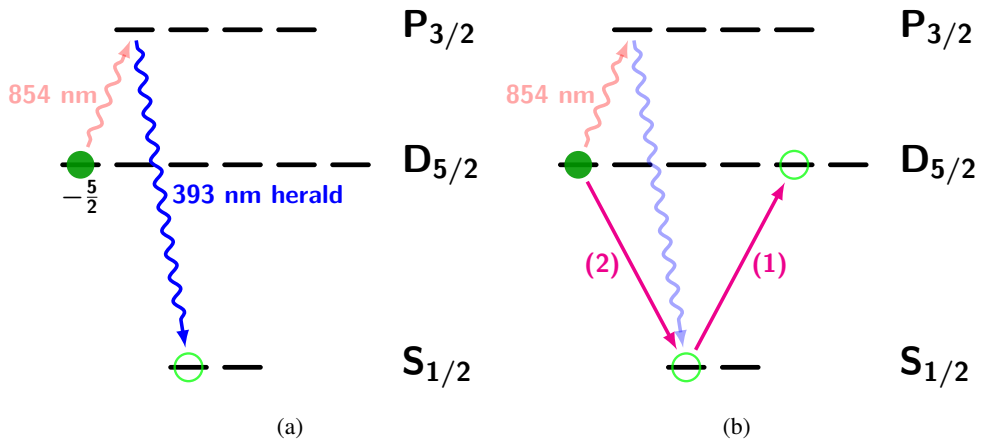

Figure II.5: Experimental scheme and background reduction. (a) The scheme shows the absorption of a σ^+ 854 nm photon (wavy red arrow) and subsequent emission of the photon at 393 nm that heralds the absorption process (wavy blue arrow). (b) State measurement for background reduction employs two coherent pulses at 729 nm after the single-photon interaction period, and subsequent state-selective fluorescence. Pulse (1) transfers population corresponding to successful absorptions into an auxiliary state while pulse (2) takes population of unsuccessful absorption cases back into $S_{1/2}$. Fluorescence emission allows one to discriminate them.

the overall losses by looking at efficiencies on both correlated SPDC arms and see if they fulfill our expectations in coincident detection. Losses at the filtering arm including fiber coupling, transmission through the filtering cavities and APD detection give rise to $\eta_{\text{fil}} \approx 0.1$, where photon losses due to stabilization periods of the cavities are accounted for in the effective experimental time (85%). At the ion arm, losses are given by photons fiber coupling efficiency (~60%), absorption efficiency at the ion and collection efficiency of 393 nm blue heralds. An absorption efficiency per source photon in the order of $\sim 1 \cdot 10^{-3}$ is calculated for this experiment from the coincidences , which is higher than the value reported in [25, 21] ($\sim 5 \cdot 10^{-4}$), and which we attribute to better preparation of the ion in the $D_{5/2}$ state by using the 729 nm laser. In these previous experiments preparation was performed by three-photon excitation into $P_{3/2}$ and further decay into $D_{5/2}$ (see Fig. II.2) with further incoherent optical pumping, which makes pure preparation into the outermost Zeeman levels not possible, thus reducing the absorption efficiency (Fig. I.8). Related information and relative comparison between these two experiments is found in [27, 22]. Calculations and measurements are discussed in section V.1, where a comparison with other experiments presented in this thesis was performed. Blue heralds collection efficiency is determined by a calibration measurement routine performed daily by using 854 nm strong laser light [26], and is found to be $\eta_{coll} = 1.86\%$ which corresponds to the overlap between the spatial emission characteristics of the ion times the collection angle of the the HALO lenses, optics transmission and detection efficiency of the two PMTs used for detection. This way an overall efficiency at the ion arm of $\eta_{\text{ion}} \approx 1 \cdot 10^{-5}$ is estimated. From a source calibration measurement, ~ 6000 resonant photons per second were generated at the crystal. With this information we estimate the expected coincidences of our measurement which is a good indicator of the understanding of the absorption process at the

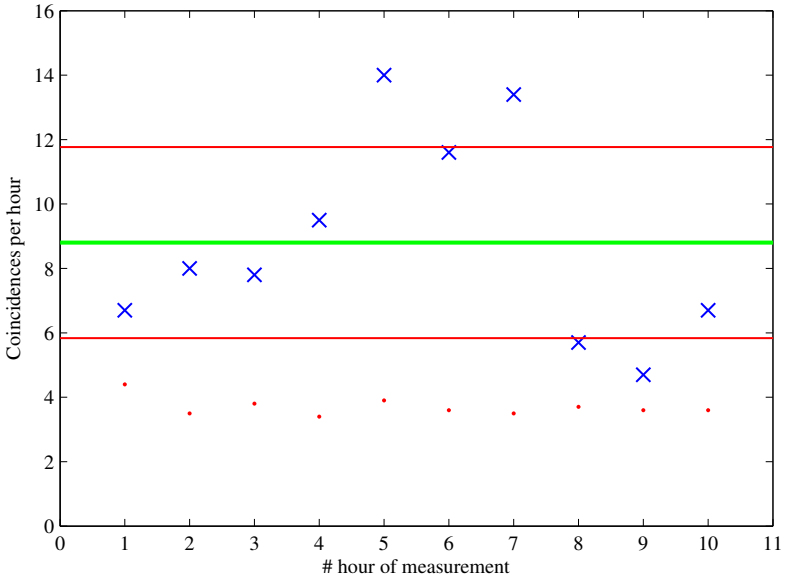

Figure II.6: Doubly-heralded coincidences between 393 nm heralds and 854 nm triggers per hour of measurement for 50 ns bins (blue crosses). Average detected coincidences per hour is 8.9 and is represented by the green line with a standard deviation (red lines, Poissonean). Estimated coincidences per hour are 7.8. Red points represent average background counts per bin. See text for details.

ion and overall losses in both arms. The number of coincidence events C and of a SPDC source with generated pair rate R_{pair} in a measurement time T is given by:

$$C = R_{\text{pair}}\, \eta_1 \eta_2\, T \tag{II.1}$$

where $\eta_{1,2}$ are the efficiencies of the individual channels, including all losses (fiber coupling, optics transmission, detection efficiency, etc.). Now, the SPDC-ion expected coincidence rate (average) is given by

$$C = R_{\text{pair}} \cdot \eta_{\text{fil}} \cdot \eta_{\text{ion}} \cdot \eta_{\text{ov}} = 6000\tfrac{1}{s} \times 0.1 \times (1 \cdot 10^{-5}) \times 0.5 = 3.0 \cdot 10^{-3}\ \tfrac{\text{coinc.}}{s} \tag{II.2}$$

we obtain an expected coincidence rate of $3.0 \cdot 10^{-3}$ coinc./s which is in good agreement with the measured rate ($3.6 \cdot 10^{-3}$ coinc./s). An additional factor $\eta_{\text{ov}} = 0.5$ has to be taken into account arising from spectral overlap between the Lorentzian shape of the narrowband photons and the Lorentzian of the $D_{5/2} \rightarrow P_{3/2}$ transition when looking at coincidences. An expected rate below the detected rate is attributed to a conservative estimation of the absorption efficiency, as explained in the section V.1. An hourly display of the detected coincidences and background counts is seen in Fig.II.6 which corresponds to the 10 hours of measurement, obtained along several days of experimental runs. One of the critical points detected in the set-up is the alignment of the photon stream onto the ion, which changes on a few-hours basis due to thermal drifts and although this is realigned periodically it might be responsible for the displayed fluctuations.

Interaction probability per herald

An interesting figure of merit for characterizing the heralded photon-atom interface is the probability of a successful absorption per detected herald, which is described by

$$P_{\text{int/her}} = \frac{C_{\text{total}}}{R_{\text{herald}}} \tag{II.3}$$

where C_{total} is the total number of coincidences and R_{herald} is the rate of detected heralds. As in this experiment we have two ways of heralding our absorption process, we look at both arms. For 854 nm filtered heralds the heralds rate is $R_{\text{fil}} = 808\text{s}^{-1}$ APD detections at the filter, which means $P_{\text{abs/fil}} = \frac{C}{R_{\text{fil}}} = 4.5 \cdot 10^{-6}$. This is an accurate figure in the sense that most of the APD detections correspond to real heralding photons, given a proportionally low dark count rate at the APD ($\sim 20\text{s}^{-1}$). Following the same procedure, the probability of photon absorption per blue herald is calculated, which is an important figure of merit for considering the implementation of two-photon-to-two-ion state-transfer scheme where no triggering partner is used. In this case $P_{\text{abs/393}} = \frac{C}{R_{393}} = 1.3 \cdot 10^{-4}$, where $R_{393} = 27.3\ s^{-1}$. In this case we expect for most of the detections at the PMTs to be dark counts since as we have discussed earlier, absorption and collection efficiencies are strongly reduced by limited spatial overlap. This is corroborated by calculating an estimated heralds rate based in the rate of absorbed photons and the collection efficiency of the ion arm. Let's recall that the detections of one of the arms of a SPDC source without background contributions nor dark counts is defined as

$$R_{Det,i} = R_{\text{pair}}\eta_i \tag{II.4}$$

where η_i the losses of the respective arm including detection efficiency. This way, the rate of expected 393 nm heralds detected by our setup is calculated as

$$R_{\text{est,393}} \approx R_{\text{pair}} \cdot \eta_{\text{ion}} = (6000\,\text{s}^{-1}) \times (1.0 \cdot 10^{-5}) = 0.06\,\frac{1}{s}. \tag{II.5}$$

As we see from this calculation, expected 393 nm heralds rate is much lower than the detected rate, confirming our expectations that most of the PMT detections correspond to dark counts rather than real absorption heralds and the main reason why a background reduction method is desirable. Furthermore, we calculate the probability of a successful absorption per detected herald after background discrimination, given by the rate of post-selected 393 nm heralds $R_{post,393} = 1.7\ s^{-1}$, which corresponds to the selected PMT events as described in the background reduction section. Thus, we evaluate $P_{\text{abs/post,393}} = \frac{C}{R_{\text{post,393}}} = 2.1 \cdot 10^{-3}$. This is the most important figure of merit in this section since it shows an increase in one order of magnitude in the heralding probability of our interface (compared to $1.3 \cdot 10^{-4}$) and illustrates the benefits of our discrimination method which becomes important for heralded quantum network schemes [26].

Characterization of background discrimination

Furthermore, since we wish to understand the process of background reduction applied by the heralds discrimination method we look at the different cases that contribute to background counts in the coincidences histogram and its differences with discrimination.

The main source of background in our experiment originates from PMTs dark counts coincident with 854 nm triggers, since at the ion there is a low probability of a photon absorption and subsequent herald detection. As discussed in the previous section, this is illustrated by looking at the detected rates. While 854 nm filtered heralds $R_{fil} = 808\ ^{-1}$ are detected, only $R_{est,393} = 0.0648\ \frac{1}{s}$ heralds are expected at the ion side. Detected rate at the PMTs is $R_{393} = 27.3\,\mathrm{s}^{-1}$ and thus corresponds mostly to dark counts. The expected background for the coincidences histogram is given by

$$B = R_{\mathrm{Det},1} R_{\mathrm{Det},2}\ \Delta t\ T \tag{II.6}$$

where $R_{\mathrm{Det,i}}$ are the detected rates on each channel, Δt is the bin size and T is the total measurement time. For the doubly-heralded coincidences of Fig.II.2(a) in red, the expected value for 50 ns bins in the 10 hours of measurement time is 39.8, which corresponds closely to the 37.1 background counts per bin detected in average.

As shown in the experimental results part, background is greatly reduced by our discrimination method. The average background in Fig.II.2(a) red, corresponds to 2.3 events per bin. With $R_{\mathrm{post},393} = 1.7\,\mathrm{s}^{-1}$, the rate of post-selected 393 nm heralding events, equation II.6 leads to an expected value for background events per bin of 2.4, which is in agreement with the previously mentioned observed value. However, the rate of post-selected heralds is still considerable higher than $R_{\mathrm{est},393}$, the estimated number of heralds. In order to explain this fact, we look at the different cases where our discrimination method still produces 'false-positives', meaning cases where decisions are positive but no real herald has been detected. Main cases leading to false decisions are:

1. wrong state preparation + successful state discrimination
2. successful preparation + wrong discrimination
3. successful preparation + spontaneous decay + successful discrimination
4. successful preparation + absorption w/o 393 nm herald + successful discrimination
5. successful preparation + absorption with 393 nm herald + successful discrimination

each of these cases happening simultaneously with the presence of a dark count during the 2 ms of absorption window will lead to a background count in the heralds list. To calculate the contributions for each case, we need to consider the associated probabilities (errors) and the rate of dark counts at the PMTs. For the dark counts rate, we use as a reference the number of PMT detections of the undiscriminated case. As we have seen, they correspond mainly to dark counts. Thus, $R_{dc} \approx 27\ \frac{1}{s}$.

First, we discuss probabilities for cases 1, 2 and 3. The preparation efficiency is the efficiency of the 729 nm $\pi-$ pulse. From calibration measurements $\eta_{\mathrm{prep}} = \eta_\pi = 99\%$. The discrimination efficiency consists of two 729 nm π-pulses and the fluorescence detection efficiency, which is 100%. The second pulse (Fig.II.5) contributes more importantly to wrong discriminations because in most of the cases, the ion stayed in $D_{5/2}$ and the first pulse does not affect this population. This way we get $\eta_{\mathrm{dec}} \approx \eta_\pi \cdot 100\% \approx 99\%$. The probability for a spontaneous decay in the 2 ms

absorption window is calculated as function of the lifetime of $D_{5/2}$ which is 1.17 s. The probability of decaying during this absorption time window is thus:

$$\eta_{\text{spont}} = 1 - e^{-\frac{2ms}{1.17s}} = 0.17\% \tag{II.7}$$

Suming up these cases we obtain

$$\begin{aligned} R_{dc\ 1,2,3} &= \left((1-\eta_{prep})\cdot\eta_{dec} + \eta_{prep}\cdot(1-\eta_{dec}) + \eta_{prep}\cdot\eta_{dec}\cdot\eta_{spont}\right)\cdot R_{dc} && \text{(II.8)}\\ &= (1\%\cdot 99\% + 99\%\cdot 1\% + 99\%\cdot 99\%\cdot 0.17\%)\cdot R_{dc} && \text{(II.9)}\\ &= (0.99\% + 0.99\% + 0.17\%)\cdot R_{dc} && \text{(II.10)}\\ &= 0.58\,\tfrac{1}{s} && \text{(II.11)} \end{aligned}$$

In the cases 4 and 5, the absorptions with and without herald sum up to the total number of absorptions. Photon absorption probability at the ion P_{abs} while photons are impinging at the ion at a constant rate $R^*_{ph} = 3500\,\text{s}^{-1}$ during an experimental cycle is

$$P_{\text{abs}} = 1 - exp(-\eta_{abs} R^*_{ph} \Delta t_{abs}) \approx 0.7\% \tag{II.12}$$

with $\eta_{\text{abs}} = 1\cdot 10^{-3}$ absorption probability in $\Delta t_{abs} = 2\,\text{ms}$ time window. Thus, the remaining dark counts are

$$\begin{aligned} R_{dc\ 4,5} &= \left(\eta_{prep}\cdot\eta_{dec}\cdot P_{abs}\right)\cdot R_{dc} && \text{(II.13)}\\ &= (99\%\cdot 98\%\cdot 0.7\%)\cdot R_{dc} && \text{(II.14)}\\ &= 0.18\,\tfrac{1}{s} && \text{(II.15)} \end{aligned}$$

This results in

$$R_{dc\ 1,2,3,4,5} = R_{dc\ 1,2,3} + R_{dc\ 4,5} = 0.76\,\tfrac{1}{s} \tag{II.16}$$

remaining dark counts from these five cases. Summing up the expected heralds rate $R_{\text{est,393}}$, the expected rate of discriminated detections is $R^*_{\text{post,393}} = 0.82\,\text{s}^{-1}$. This accounts for only 48% of the real detected rate $R_{\text{post,393}}$. As the analyzed cases are expected to be still the most relevant contributions, the observed inaccuracy is attributed to a sum of the following factors: an underestimation of the dark counts rate at the PMTs, an overestimation of the error in the state preparation (changes on a daily basis, reaches up to 99.9%) and the underestimation of the absorption probability. Nevertheless, the observed rate of discriminated absorption events is still much lower than the non-discriminated case, meaning this method is an effective way of tackling background contributions produced by dark counts. Moreover, the method is easily extended for correcting preparation pulses affecting state preparation and discrimination. This extension becomes important for more sophisticated schemes, as described in the following.

II.6. State preparation error and coherent superposition

Background reduction method can be extended to also eliminate the background related to failed state preparation: by applying a 397 nm laser pulse after the 729 nm preparation pulse, remaining

$S_{1/2}$ population is stored in the $D_{3/2}$ metastable state (see Fig. II.7) until the end of the interaction period. The discrimination pulses leave the $D_{3/2}$ population untouched, such that once performing fluorescent detection for discrimination, it will correctly contribute to the bright cases, i.e. to the no-absorption result of the state measurement. Its use is recommendable for cases where several

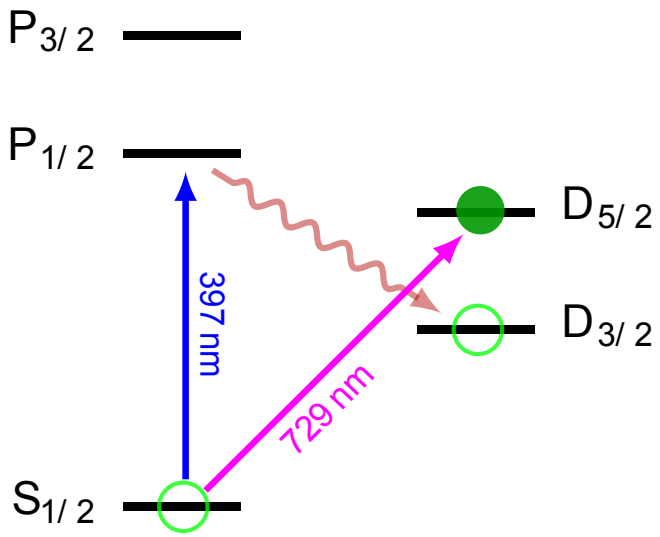

Figure II.7: After state preparation into $D_{5/2}$ with a 729 nm pulse, a subsequent 397 nm pulse carries the remaining population (unsuccessful preparations) into $D_{3/2}$ for temporal storage. At the end of the sequence fluorescence detection sums up these cases with discriminated non-absorption events (Fig. II.5).

coherent 729 nm pulses are needed, since preparation errors scale proportionally. Moreover, a very important aspect of the design of the scheme is to allow one to discriminate preparation pulses error protecting the final state of the ion upon the absorption, which means in case of quantum state storage that the scheme will improve the heralding but without spoiling the information stored. This is achieved by bringing final state of the ion from $S_{1/2}$ into $D_{5/2}$ as seen in Fig. II.5(b) (1), making it invulnerable to operations made in $S_{1/2}$, e.g. fluorescence detection.

As discussed earlier, a relevant goal is the heralded mapping of single photon states into the ion, where an ion is prepared in a polarization sensitive superposition in $D_{5/2}$ so that upon absorption, the polarization state of the photon is stored into the final state of the ion $S_{1/2}$, as in the protocol presented by Kurz, shown in Fig. II.8.

Furthermore, once could use an SPDC photon from a polarization entangled pair, such that at the end of the process the internal state of the ion is entangled with the polarization of traveling partner photon [22, 26]. However, photon absorption and collection efficiencies are low due to reduced spatial overlapping even when HALOs are used, making the use of the discrimination method an attractive alternative for identifying real heralds, for instance for quantum state tomography where a big number of measurements has to be performed.

As an example, two possible schemes of the discrimination method for state mapping are presented and which are implemented easily with the tools already presented. First, a scheme for state analysis after state mapping is shown in Fig. II.9. This scheme follows the same principle as

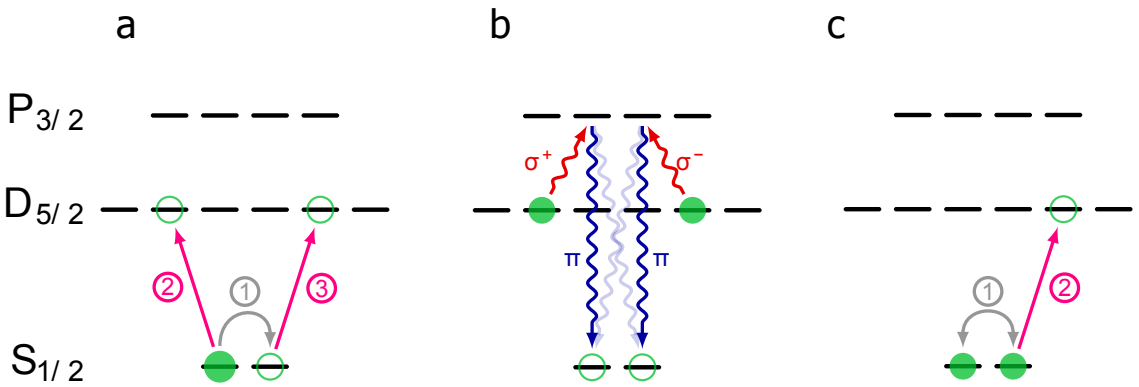

Figure II.8: (a) Scheme for photon-polarization storage. Firstly, a coherent superposition is created between m=-3/2 and m=+3/2 substates of $D_{5/2}$ using one RF (1) and two 729 nm pulses (2,3). (b) An 854 nm laser photon of arbitrary polarization (red arrows) is absorbed producing a single 393 nm photon emission (wavy arrows). The detection of a π-polarized 393 nm photon (dark-blue) projects the atom into a superposition state in $S_{1/2}$ corresponding to the 854 nm photon polarization. (c) Electron shelving using a RF and 729 nm pulses (1,2) and further fluorescence detection allows reading out the final state in a desired basis. From [30, 26]

in Fig.II.8 but using dark counts discrimination. Differently to the doubly-heralded case, a series of 729 nm and additional RF pulses are used for preparation, transfer and basis selection. As suggested earlier, 397 nm pulses are used to transfer remaining population in $S_{1/2}$ into $D_{3/2}$, which are unsuccessful 729 nm preparations into $D_{5/2}$. As in Fig. II.7, the meta-stable $D_{3/2}$ is used as temporal population storage until the end of the sequence, from where it is retrieved for discrimination by fluorescence detection with 397 nm and 866 nm lasers. This way, error related to 729 nm preparation and discrimination pulses in (a) and (c) is considered and summed up to no photon absorption cases. Once more, by looking at the ion's fluorescence (dark/bright) and correlating it with 393 nm detections list, dark counts mimicking heralds at the PMTs are discriminated. The RF pulse in (c) is what determines the basis selection: no RF-pulse would project the state in σ_z otherwise with an RF-pulse in a chosen superposition $\sigma_\phi = \cos(\phi)\sigma_x - \sin(\phi)\sigma_y$, where σ_i Pauli matrices and ϕ is the phase determined by the detection time of the herald [26].

Furthermore this method is also adapted for only-storage case where heralds are discriminated from dark counts without performing projective measurements, i.e. the state in the ion is left untouched. Such a protocol is presented in Fig. II.10.

In this sequence no additional RF basis-selection is performed, meaning the whole superposition is transfered between S and D. In some cases after background discrimination in (d) one might want to skip step (e), since central Zeeman substates of the $D_{5/2}$ manifold are less vulnerable to magnetic field induced decoherence, although at the cost of a limited lifetime. Other schemes according to different possible storage protocols as described in [54] or even for atom-photon entanglement can be adapted straightforwardly following the same logic. Further considerations as well as geometrical conditions for entanglement transfer and heralds detection are not further discussed here since these are described in detail in [26].

An important remark for these schemes is related to time and error cost of the added pulses.

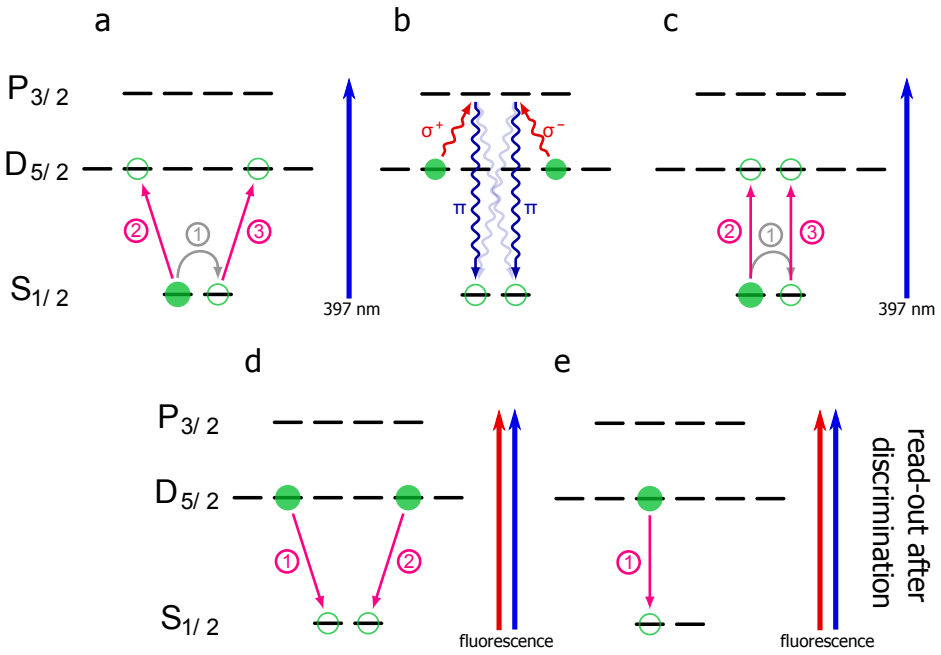

Figure II.9: Photon state mapping and analysis. (a) A coherent superposition is created between $m = -\frac{3}{2}$ and $m = +\frac{3}{2}$ substates of $D_{5/2}$ using one RF (1) and two 729 nm pulses (2,3). (b) A single 854 nm photon of arbitrary polarization (red arrows) is absorbed producing a single 393 nm photon emission (wavy arrows). The detection of a π-polarized 393 nm photon (dark-blue) projects the atom into a superposition state in $S_{1/2}$ corresponding to the 854 nm photon polarization. (c) A RF pulse (1) defines the desired basis for state analysis and two 729 nm pulses (2,3) bring the superposition into $D_{5/2}, m = \pm\frac{1}{2}$. (d) Two 729 nm pulses bring remaining population from (a) corresponding to non-absorption cases into $S_{1/2}$. Optional 397 nm pulses after (a) and (c) can be used to account for their four 729 nm pulses unsuccessful preparations error, sending the related population into $D_{3/2}$. After (d), fluorescence detection is performed (397 nm and 866 nm), where unsuccessful preparations and non-absorption cases sum up and produce a bright ion for herald discrimination (unsuccessful cycle).(e) If the ion has remained dark, electron shelving 729 nm pulse is applied from $D_{5/2}, m = -\frac{1}{2}$ into $S_{1/2}, m = -\frac{1}{2}$ and fluorescence detection concludes the state read-out in the chosen basis. In this scheme, no final superposition is available since the ion has been projected into a particular basis for state analysis.

Every 729 nm pulse has an associated error of $\sim 1\%$ and a duration of about 7 µs, nevertheless 729 nm preparation error is low and it is tackled with the implementation of 397 nm pulses, where the time cost is short compared to duration of a standard sequence (few ms). However, to evaluate the utility of discriminating errors of cases were no photon absorption takes place and the overall utility of the discrimination method we take a look at the absorption probability. Let us write the photon absorption probability at the ion P_{abs} while photons are being sent at a constant rate during an experimental cycle as

$$P_{\text{abs}} = 1 - exp(-R_{\text{abs}} \cdot \Delta t_{\text{abs}}) \tag{II.17}$$

with R_{abs} the photon absorption rate and time window Δt_{abs}. Furthermore, $R_{abs} = \eta_{abs} R_{ph}$, mean-

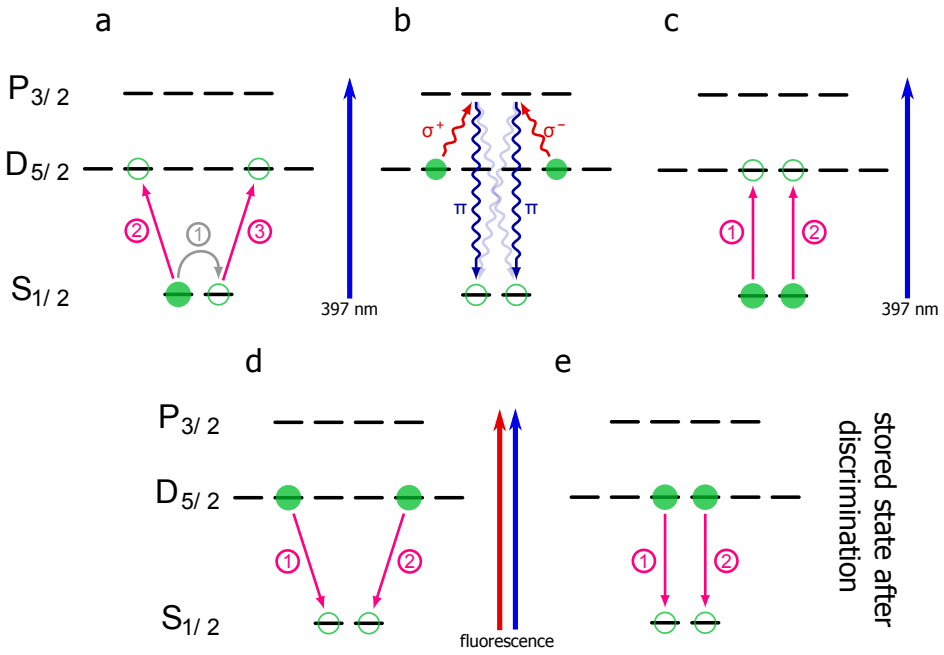

Figure II.10: Photon state storage with background discrimination. (a) A coherent superposition is created between m=-3/2 and m=+3/2 substates of $D_{5/2}$ using one RF (1) and two 729 nm pulses (2,3). (b) A single 854 nm photon of arbitrary polarization (red arrows) is absorbed producing a single 393 nm photon emission (wavy arrows). The detection of a π-polarized 393 nm photon (dark-blue) projects the atom into a superposition state in $S_{1/2}$ corresponding to the 854 nm photon polarization. (c) Two 729 nm pulses (1,2) map the superposition into $D_{5/2}, m = \pm 1/2$. (d) Two 729 nm pulses bring remaining population from (a) corresponding to non-absorption cases into $S_{1/2}$. As before 397 nm pulses after (a) and (c) are applied to account for 729 nm unsuccessful preparations by sending remaining population into $D_{3/2}$. After (d), fluorescence detection is performed for discrimination (unsuccessful cycle).(e) If the ion has remained dark, the superposition can be brought back into $S_{1/2}$ for storage.

ing the absorption probability is dependent on the product $\eta_{abs} R_{ph} \Delta t_{\text{abs}}$; absorption efficiency, resonant photon rate at the ion and length of the absorption window, respectively. From this equation very useful information is extracted for the design of the experiment. Absorption efficiency at the ion is limited by geometry up to $\sim 2 \cdot 10^{-3}$ due to oscillator strength and Clebsch-Gordan coefficients of the transition, times the solid angle of the HALO lens. The absorption window can be extended, although ultimately is also limited by the probability of spontaneous decay from $D_{5/2}$, as $P_{\text{sp}} = 1 - exp(-\Delta t_{\text{abs}}/t_{sp})$, one would thus expect to stay in the few milliseconds region in order to keep spontaneous decay probability below 1% during the absorption window and also to avoid decoherence in $D_{5/2}$. Finally, the decisive parameter will be R^*_{ph}, the rate of resonant photons impinging on the ion. With the previous parameters a photon rate of 10^6 is needed to come to unitary absorption probability, meaning 3 orders of magnitude higher than the rate of photons used in the experiment presented here, which could be reached with a cavity enhancement set-up or a state-of-the-art waveguide source [71, 50, 72]. Under these optimal conditions, a few thousands

393 nm heralds per second are emitted by the ion. It can be seen that the discrimination method is still useful because collection and detection efficiencies decrease herald detection rate down to $\sim 2\%$. As PMTs dark counts are in the region of dozens per second, we end up in the best case in the same order of magnitude for heralds and dark counts, making this method still valuable even for much better experimental resources.

II.7. Conclusion

As a summary, we have realized an interface where a single emitted photon heralds the absorption of a single SPDC photon by a single atom. This demonstrates that our protocol for high-fidelity heralded photon-to-atom quantum state transfer, presented in [30], can be extended to single photons. Successful absorption is heralded by the coincident detection, within < 50 ns, of the emitted photon at 393 nm and the SPDC partner photon at 854 nm. The time correlation displays the expected double-exponential temporal structure. Furthermore, we presented a way to efficiently reduce background counts by verifying the atomic state after the detection of a herald, which is important as the fidelity of photon-to-atom state conversion may be reduced by dark counts that mimic heralds and heralding probability is reduced. With small time overhead and no additional lasers, we decreased the background counts by a factor of 16, leading to a 4.1-fold improvement of the signal-to-noise ratio and one order of magnitude increase in the absorption probability per herald detection. As we have shown, this method is easily extended for more sophisticated schemes and provides a powerful tool accounting even for the remaining sources of error. These results add another proof-of-principle to constructing a quantum network toolbox with single photons and single atoms. As discussed, a brighter entangled photon source will allow us to implement full photon-to-atom quantum state transfer and to work towards entanglement mapping from photon pairs to distant atoms [54, 30, 9]. In the following chapter we analyze the extension of this interface into the telecom range using quantum frequency conversion, which means a major step toward a quantum communication network since it allows one to extend the heralding process in long-distance communication and eventually to connect different quantum systems.

Chapter III

Quantum frequency conversion for a single-photon–single-atom based quantum network

Although atomic systems have shown to be excellent candidates for storage and processing of quantum information in a quantum network [5], an important limitation arises from using optical transitions in the near-infrared (NIR) region of the spectrum where fiber transmission losses and decoherence effects due to dispersion are high for photons carrying the information.

A solution for this problem is using quantum frequency conversion (QFC) for translating wavelengths into the optical telecommunications region, where fiber transmission losses and dispersion are low and for which already implemented infrastructure for classical communications could be used. Furthermore, for long distance communication (>100 km) conversion into and from atomic memories wavelengths could strongly enhance possibilities for atom-based quantum repeaters schemes [9]. Even though there are remarkable examples of systems that permit working directly at telecom wavelengths [73, 72, 16, 74, 75], using frequency conversion provides a general solution for interfacing any type of quantum systems. This is a big advantage since in a network scenario several properties are necessary, i.e. long storage times, fast processing capabilities, high-quality entanglement, compatibility with long distance communication, high emission rates, etc. which are hard to obtain with a single type of quantum system.

Several realizations using frequency conversion for quantum systems have been shown, including light conversion in atomic non-linear media [76] and more often using non-linear crystals for converting memory wavelengths for cold Rubidium clouds [17], quantum dots [77, 78] and doped crystals [79, 80]. Moreover, with the help of frequency conversion entanglement between a quantum dot spin and a telecom photon has been shown[81, 82]. Despite these notable results, quantum-network schemes including dissimilar quantum systems are to be shown, especially involving true single-photon conversion, where pump-induced noise from the conversion process might make its implementation challenging [17].

In the present chapter we present a set of measurements featuring quantum frequency conversion (QFC) of memory-wavelength heralded single photons generated by spontaneous parametric down-conversion (SPDC). Furthermore, we show its use in a composite interaction experiment with a single trapped $^{40}Ca^{+}$ ion by detection of single-photon time correlations. Through this results we propose that these systems are an excellent candidate for the implementation of a single-photon single-ion based quantum network, where single telecom photons work as long-distance carriers of information and single trapped ions work as nodes for storage and processing [37, 64, 29, 30].

SPDC photons are generated at an ion's transition wavelength at 854 nm and furthermore converted into telecommunications O-Band at 1310 nm.

For a real single-photon single-atom scenario not only wavelength and spectral characteristics are important, but also quantum-mechanical features of the system. Since quantum mechanical properties of our atomic system are shown in detail elsewhere [23, 30], here we focus particularly on our photonic interface, meaning frequency-converted SPDC photons. We show that the strong time correlation between signal and idler photons of the original SPDC pair is preserved after the conversion process for memory-compatible photons, that this way also energy-time entanglement and heralded single-photon characteristics are maintained, and finally that frequency conversion allows one to signal a single-photon absorption by the single ion at a telecom wavelength by single-photon conversion of the SPDC triggering partner. Closing, an additional experiment for wavelength multiplexing in the telecom band using telecom O- and C-bands is presented, which presents additional perspectives on hybrid classical-quantum communication.

Results presented in this chapter have been edited into three articles for journal publication [83, 84, 85], and also partially presented in [58]. A comparison of the performance of this interface and experiments using an alternative telecom-OPO source are presented in the following chapter.

III.1. SPDC-QFC photonic interface

Our photonic interface is composed by two setups, a degenerate SPDC pair source at 854 nm and a quantum frequency converter used here for converting 854 nm photons into the telcom band at 1310 nm. The SPDC photon-pair source generates narrow-band heralded single photons by single-pass pumping of a non-linear PPKTP (periodically poled potassium titanyl phosphate) bulk crystal. As presented earlier in this thesis, this source was designed such that generated photons match the $D_{5/2} \rightarrow P_{3/2}$ transition in $^{40}Ca^{+}$ ion at 854 nm [53, 52]. Pumping at 427 nm is performed by an amplified frequency-doubled 854 nm diode laser (Toptica, TA-SHG pro), which is actively stabilized to the atomic transition via transfer lock [70]. Due to type II phase-matching, photons of a generated pair have perpendicular polarizations that can be used for generating high quality-polarization entanglement [53], however for using our source as an heralded single-photon source, photons are split by a polarizing beam splitter (PBS) meaning any polarization entanglement is projected out. Photons leaving through its transmitting port (H-pol.) are sent into a spectral filtering stage consisting of two cascaded optical cavities with 22 MHz transmission bandwidth compatible with the mentioned transition in $^{40}Ca^{+}$, thus selecting ion-resonant photons. Due to energy conservation of the SPDC process, partners of the filtered photons fulfill the same spectral requirements, ergo they can be absorbed by the ion [53, 19]. In the following, the use of filtering cavities allows one to look at the characteristics of selected narrow-band photons while for interaction experiments with the ion (which works itself as a filter) it helps reducing background at the heralding side produced by broadband SPDC emission, as discussed further.

Quantum frequency conversion (QFC) is realized using a single photon level difference frequency generation (DFG) process in a periodically poled lithium niobate (PPLN) waveguide chip (fabricated by NTT). General properties of this setup are discussed in detail in [58] and have been reviewed in I.4. For the present experiments, SPDC photons at 854 nm are overlapped inside the waveguide with a strong 2453 nm pump field producing as a result converted O-band telecom

photons at 1310 nm. SPDC photons coming from the ion laboratory are transmitted through a 90 meters long single-mode fiber with a transmission of 63% into another laboratory in the same building where the frequency converter setup is placed (converter lab). This fiber channel shows a polarization stability good enough for working without stabilization (<23 mrad over a day of measurement). In order to facilitate the alignment and polarization adjustments of the incoming SPDC photons, a 854 nm weak laser probe coming through the same long fiber channel has been used. After frequency conversion in the waveguide, telecom photons are separated from the 2.5 µm pump field and residual 854 nm photons by using dichroic mirrors and passive filters, after which they are fiber coupled for detection. We define the over-all conversion efficiency as the ratio between the 1310 nm photon rate inside this final fiber and the rate of 854 nm photons before waveguide coupling, i.e. including all coupling and filtering losses. As mentioned earlier, about 8% conversion efficiency has been achieved at this wavelength.

III.2. Non-classical characteristics of SPDC-QFC single-photon interface

Conservation of non-classical characteristics after quantum frequency conversion has been recently shown, including photon entanglement, photon anti-bunching and indistinguishability [15, 77, 86, 78]. These characteristics are essential for a quantum network relying in single photons to carry quantum correlations between nodes of the network for entangling operations and transmitting quantum information [10, 5, 29]. In the present section we show how strong time-correlations, energy-time entanglement and heralded single-photon characteristics of our SPDC photon are preserved after quantum frequency conversion. These experiments bridge a pending gap between a pure-photonic telecom interface with a memory-compatible photon source by frequency down-conversion, completing a set of tools for an atom-photon based quantum network.

III.2.1. Preservation of time correlations

Strong signal-idler time correlations of an SPDC pair is a non-classical characteristic which arises at its generation and related to its energy-time properties. Generated photons are created within a time interval corresponding to the extension of the pump photon packet and limit the certainty of their position [87]. In the following we see how the time correlation between the generated pair, observed by coincidence detection between signal and idler fields, keeps its behavior after frequency conversion.

In the first set of coincidence measurements we look at broadband 854-854 nm and 854-1310 nm photon coincidences, meaning no narrowband filtering is applied to the photons. 854 nm SPDC photon pairs are generated at a constant rate by continuous pumping of the PPKTP crystal with 0.5 mW pump power, allowing one to stay below APD saturation at a rate of heralds of $\sim 100\,000\,\mathrm{s}^{-1}$. On the other arm (reflected arm of the PBS) photons are detected with an APD for 854 nm unconverted photons, and further using a SSPD for 1310 nm converted photons. For the later case, frequency conversion setup is ran at maximum conversion efficiency as described in the earlier section. The setup for time correlations measurements is shown in Fig. III.1(a). The coincidences histogram for unconverted photons is shown in (b) while coincidences after applying

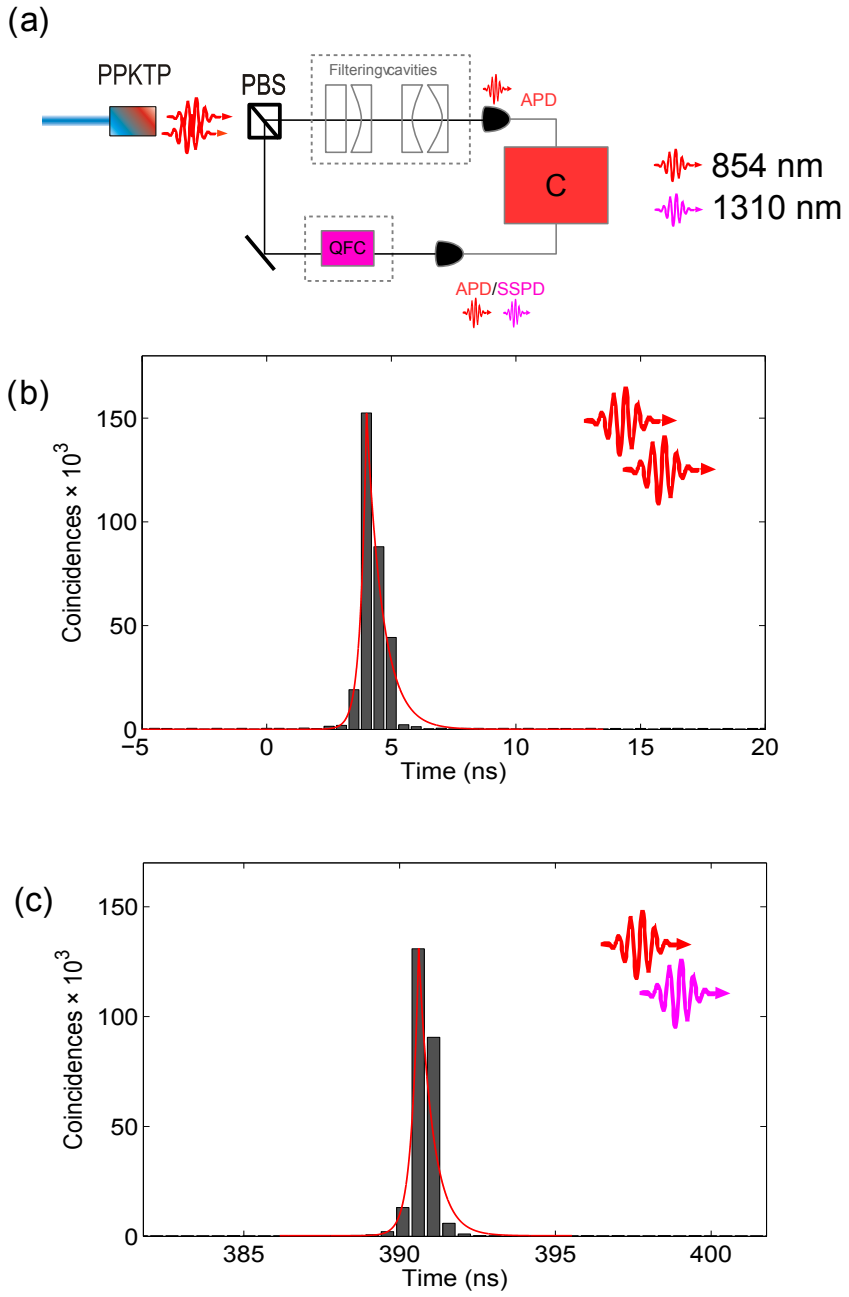

Figure III.1: (a) Experimental setup for time-correlations measurements (see text for details). When applied (dashed lines), filtering cavities reduce strongly the bandwidth of the original SPDC photons, mimicking the $D_{5/2}$-$P_{3/2}$ transition of the $^{40}Ca^{+}$ ion . After 854 nm coincidences measurement using avalanche photodiodes (APDs), reflected photons at the polarizing beam splitter (PBS) are sent for frequency conversion and detected at 1310 nm using a superconducting single-photon detector(SSPD). (b) Coincidences histogram of unfiltered broadband SPDC photon pairs at 854 nm. (c) Coincidences histogram of unfiltered broadband SPDC signal photons at 854 nm with converted partners photons at 1310 nm. The time resolution is limited in both cases by detector time jitter (exponential fits, red lines).

quantum frequency conversion (QFC) in (c), both for 500 ps time binning. Data sets are selected for comparison of the time structure having similar number of coincidences $C_b = 3.0 \cdot 10^5$ and $C_c = 2.4 \cdot 10^5$ respectively[1]. A similar temporal behavior is observed for both: a narrowband coincidence peak whose structure doesn't represent the photons but which is ruled by the time jitter of the single photon detectors (APD, SSPD). The expected width for these time correlations is of 3-5 ps, in contrast, using known values for detectors jitter; $\tau_{j,APD} = 350$ ps and $\tau_{j,SSPD} = 600$ ps we fit a simplified exponential rising-time model for the correlation function and obtain a full width half maximum of $\Delta T_{\text{unconv}} = 621 \pm 245$ ps and $\Delta T_{\text{conv}} = 475 \pm 209$ ps for the unconverted and converted photons respectively, which are represented by red curves in the histograms (fitting functions). The differences in the correlations peaks are attributed to the use of detectors with different time jitter and not to the photon structure which is well below the detector resolution. However, as it will be shown later, spectral properties of the QFC process reduce in part the broadband SPDC photon spectrum thus increasing its temporal extension, although this effect doesn't extend enough the photon wavepacket to overcome our time resolution limitations.

Furthermore, we focus on our primary interest which is looking at time correlations of narrowband memory-compatible SPDC photons. The experimental setup is the same as in Fig. III.1(a), this time applying the filtering cavities (dashed line). We start by measuring narrowband 854-854 nm coincidences. Its histogram is shown in Fig. III.2(a), which was obtained by pumping our SPDC source for three minutes with a power of 2.85 mW. A coincidence rate of 4.97 cts./s is obtained from the data. This time, due to the long temporal extension of the filtered-photons wave-packet, we are not limited by time resolution of the detectors and resolve their temporal shape. The coincidences exhibit an exponential time decay with a time constant 7 ± 0.4 ns given by the ring-down time of the cavities. This time constant corresponds to 22.9 ± 1.3 MHz very close to the 22 MHz (7.25 ns) of the $D_{5/2} \rightarrow P_{3/2}$ transition, as expected from its design (sec. I.3).

Moreover, to show preservation of temporal correlations of narrowband 854 nm photon pairs after frequency conversion, we correlate 854 nm filtered heralding photons with their 1310 nm partner photons, which have been frequency-converted from 854 nm following the procedure described earlier. The respective histogram is presented in Fig. III.2(b). This time, detector saturation is not an issue since the heralding rate is reduced by filtering of the cavity, we increase thus the SPDC pump power to the maximum available level of 55 mW and collect detection events for 30 minutes. As expected, we observe a similar temporal behavior with a time constant of 7.3 ± 0.7 ns showing good agreement with former results. For converted photons case we find a coincidence rate of 4.15 cts./s compared to 96.1 cts./s of the unconverted case extrapolated linearly to the same pump power, corresponding to an over-all conversion efficiency of 7.8 %, which is in agreement with the characterization measurements. Between both histograms differences arise from different signal and background conditions. Coincidences rate in the converted case are reduced by fiber transmission and conversion efficiencies at the converter arm. Including detection efficiency, overall efficiency at the converter arm is $\eta_{\text{conv}} \approx 8 \cdot 10^{-3}$. As expected, most of detections at the converter arm correspond to broadband converted SPDC photons outside the

[1] Although particular data sets presented here are useful for illustrating temporal structure of the correlations, they were not acquired for performance comparison and show efficiency differences with the upcoming results, thus they are not detailed here. Further details on the efficiency of frequency conversion is discussed further in this and following sections.

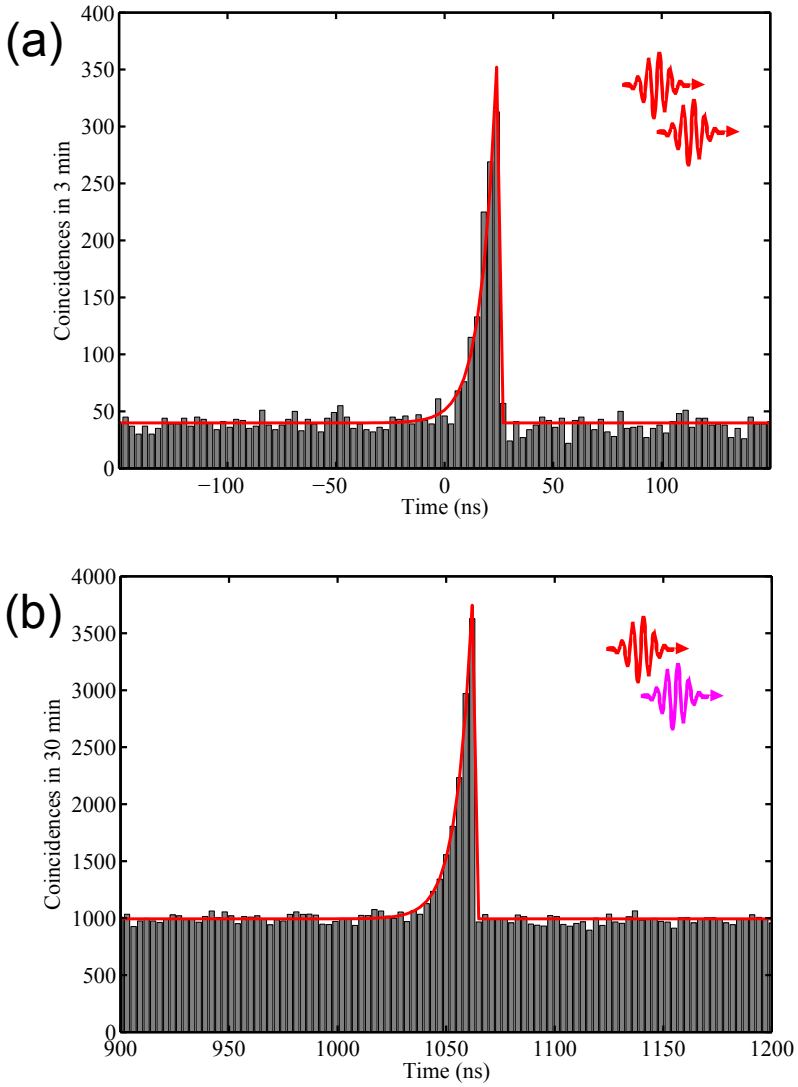

Figure III.2: Time correlations of narrowband photons. Experimental setup is shown in Fig. III.1a (a) Coincidences histogram of filtered SPDC photon pairs at 854 nm. Long exponential decay corresponds to the ring-down time of the cavities, with time constant of 7.0 ns. (b) Coincidences histogram of the SPDC filtered signal photon and its telecom-converted partner. Temporal structure of the original photons is preserved after quantum frequency conversion (QFC) with 7.3 ns time constant. Red lines correspond to exponential fits for the long time decay. The steep edge is the time jitter of the detectors.

selected 22 Mhz bandwidth. At maximum power, SPDC source generates ~ 5000 resonant photons per second, meaning out of them, about 40 s^{-1} converted narrowband SPDC photons are expected at the SSPD compared to an actually observed detections rate of 165907 s^{-1}. From these photons, approximately 4000 detected events per second are residual from the converter process, however, spectral selection of the 118 GHz acceptance bandwidth of the conversion process compensates importantly this effect by reducing the background produced by non-resonant broadband SPDC photons in ~ 50%, avoiding an additional of ~ 170 000 background counts at the SSPD, estimated by extrapolation of detections events at the APD in the unconverted measurement. An illustrative example of the convenience of such filtering effects of the conversion process has been reported in [78], where single-photon characteristics of converted photons from a single emitter are improved by spectral selection. Although background reduction and spectral shaping effects are highly desirable, signal reduction by limited efficiency of the whole conversion channel has still a higher impact in the final result, as seen in Fig. III.2. In the following sections we will show how conservation of these time correlations between herald photons and converted partner allows us to observe photon entanglement and single-photon absorptions.

III.2.2. Preservation of Energy-time entanglement

In this section, we show coherence and Franson interference measurements performed with our SPDC-QFC interface for broad band photons. These results have been discussed in detail in A. Lenhard's thesis [58], thus they are discussed here in a summarized manner. A draft version of the corresponding paper is found in the appendix B.1.

In 1989, J.D Franson proposed a way to test Bell's inequality using two-photon state interference effect [56]. This proposal was interesting since back then implementations had focused mostly on superposition of polarization states and this new approach offered an alternative for testing the EPR paradox with continuous variables. Although original Franson's proposal is for an atomic EPR source, SPDC has shown to be an ideal system for testing this effect due to the strong energy and time correlation of pair arising from the enforcement of energy conservation and the nature of the generation process, respectively [46].

The "Franson experiment" is an interference effect between a two-photon wave and a time-shifted version of itself. Individual photons of a two-photon state run through individual unbalanced interferometers and are detected at its end, as shown in Fig.III.3. The unbalance of the interferometers (T_a, T_b) has to be much longer than the single-photon coherence time T_c, for avoiding single-photon interference effects and shorter than the coherence of the pump T_p, for coherence between photons to be kept ($T_c \ll T_{a,b} < T_p$). When both interferometers are equally unbalanced, the two photon state for single frequency modes can be written as

$$|\Psi\rangle = \frac{1}{\sqrt{2}}\Big(|s_a, s_b\rangle + e^{i(\Phi_a+\Phi_b)} |l_a, l_b\rangle + e^{i\Phi_a} |l_a, s_b\rangle + e^{i\Phi_b} |s_a, l_b\rangle \Big) \tag{III.1}$$

given by the four possible paths, two short s_a, s_b or two long l_a, l_b. Cases where both photons take either short or long paths of their respective interferometers can not be distinguished and are thus entangled. Leaving out the other two cases, the post-selected entangled state for the pair is :

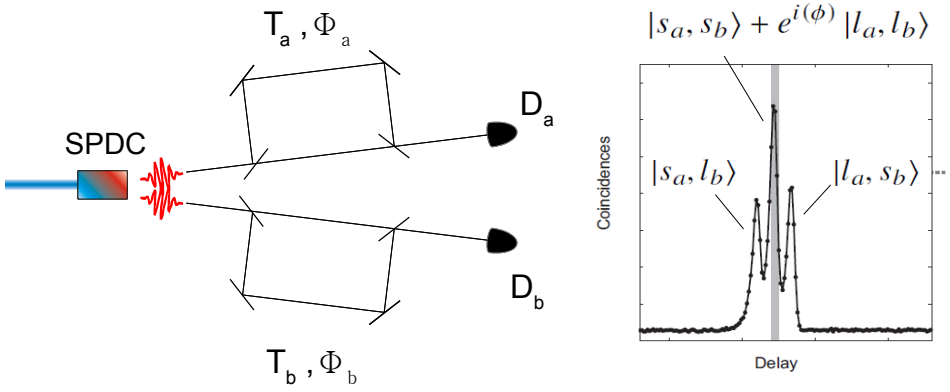

Figure III.3: Scheme for Franson interference using SPDC photons. Long arms $l_{a,b}$ of the interferometer introduce phase differences $\Phi_{a,b}$ compared to short path $s_{a,b}$. Post-selected coincidence window for energy-time entangled photons is shown in gray (III.2), and depends on the combined interferometer's phases ϕ. See text for details.

$$|\Psi\rangle_{\text{post}} = \frac{1}{\sqrt{2}}\Big(|s_a, s_b\rangle + e^{i\phi} |l_a, l_b\rangle \Big) \tag{III.2}$$

where $\phi = \Phi_a + \Phi_b$, the sum of the phases of each interferometer unbalance. Coincidences for this state are given by

$$C_{ab} = \cos^2\left[\frac{\Phi_a + \Phi_b}{2}\right] \tag{III.3}$$

meaning coincidences are modulated by phase changes in any of the interferometers, meaning by scanning either of both we will observe interference fringes when looking at coincidences. A 100% visibility is expected, arising from the strong correlation between conjugated photons in the state III.2 [46, 49]. A more complete multi-mode photon description shows that the interference at the coincidences is in addition modulated by the two-photon coherence function [49]

$$F(\tau) = \frac{\int_{-\infty}^{+\infty} g_a(t)\, g_b^*(t+\tau)\, dt}{\int_{-\infty}^{+\infty} g_a(t)\, g_b^*(t)\, dt} \tag{III.4}$$

which corresponds to the convolution between the first-order coherence functions of the photons $g_{a,b}(t)$. In the following, we show that we satisfy coherence conditions to observe Franson interference and measure successfully the two-photon coherence function for our hybrid photonic system, which is also corroborated by measuring individual coherence functions (854 nm and 1310 nm photons).

First-order coherence

First-order coherence functions for 854 nm and converted 1310 nm photons are measured using a Michelson interferometer (MI). Both functions are analyzed independently for single photons by

looking at singles rates after the interferometer and will be used later for comparison with Franson two-photon state interference, which is measured in coincidences. Coarse and fine displacements are used in the opposite mirrors of the interferometer (M1, M2) such that we can step-wise scan the first-order function while finely scanning the oscillatory single-photon interference pattern for determining the visibility at every step, respectively. Coarse steps performed with a mechanized translational stage sets a length (time-equivalent) difference up to 1.7 ns in 7 fs steps while fine sub-fs scanning is done with a piezo actuator. Both coherence functions are measured with the same interferometer meaning optics are replaced and APD (Perkin Elmer) and SSPD (Single Quantum) are exchanged for detecting 854 nm and 1310 nm photons respectively. The coherence

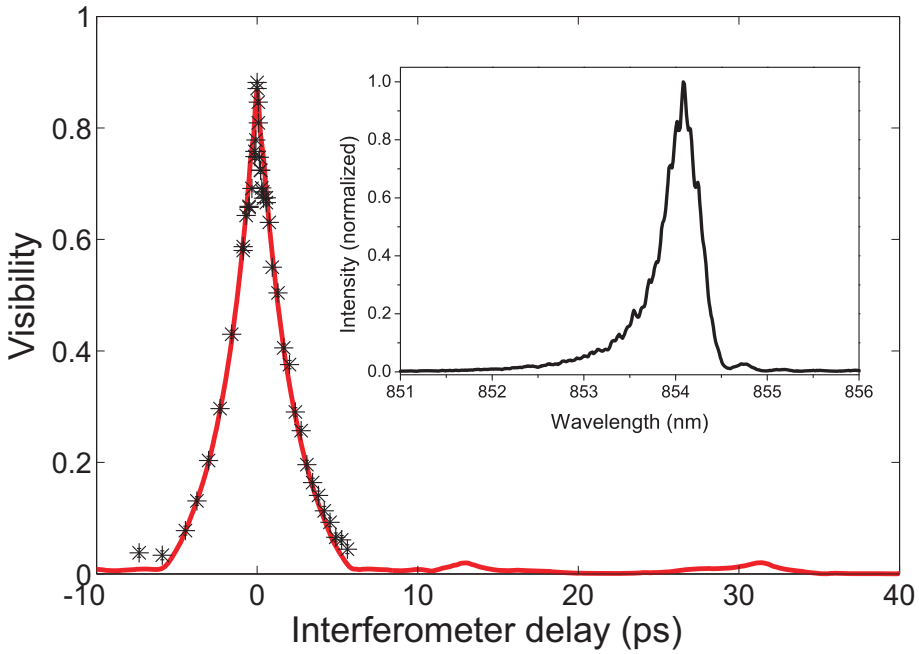

Figure III.4: First order coherence for 854 nm photons. Black stars represent measured visibility as a function of the coarse interferometer displacement. Inset shows photon spectrum measured with an spectrometer, used for deriving the red solid line.

function of 854 nm photons is shown in III.7. Single counts interference oscillations are detected using 100 ms integration time and visibility is obtained by sinusoidal fits in a similar fashion to Fig. III.4, with $V = \frac{I_{max}-I_{min}}{I_{max}+I_{min}}$. This way, a maximum visibility of 88% is found, which is limited by the interferometer visibility of the same value as measured for calibration purposes using laser light. The spectrum of these 854 nm photons was measured using a spectrometer (Princeton Instruments SP2500A, grating of 600 lines/mm) shown in the inset of Fig. III.4. By Fourier transform of this spectrum (173 GHz FWHM), the envelope of the coherence function measured with the interferometer is obtained for comparison, coming to good agreement (red solid line). A coherence time of $\tau_c = 3.7$ ps is found by integrating the coherence function over time, which allows one to define a coherence time independent of its shape.

Furthermore, after adapting the interferometer for telecom wavelengths the same procedure is repeated for converted photons and its coherence function is measured as seen in Fig. III.5. For

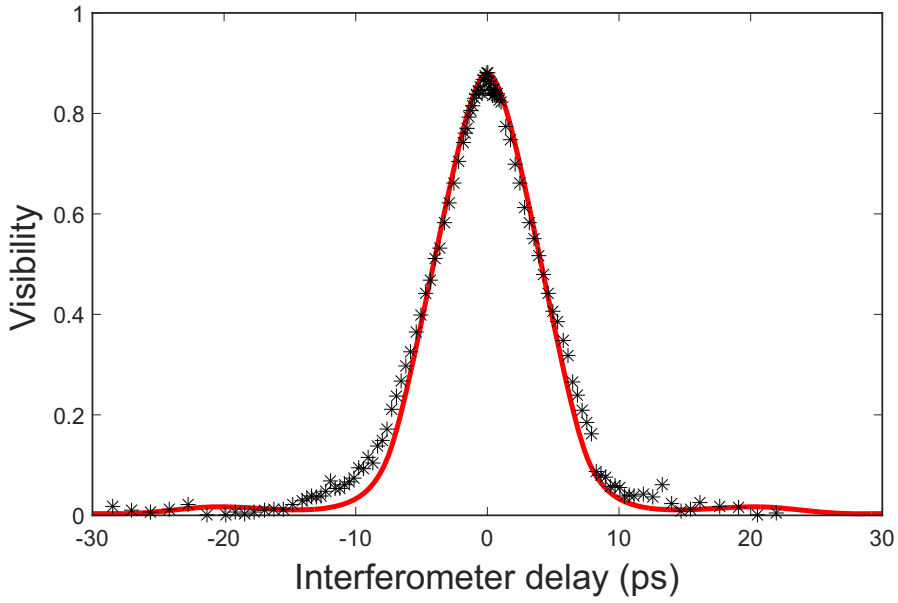

Figure III.5: First order coherence for 1310 nm photons. Black stars represent measured visibility as a function of the coarse interferometer displacement. In this case, the red solid line is obtained from a convolution between conversion process and original photon spectra.

this case a coherence time of $\tau_c = 10.5\,\text{ps}$ is found, where an increased length of the photon arises from the spectral filtering effect of the conversion process mentioned earlier in this chapter. The spectrum of converted photons is calculated from the convolution of the original 854 nm photon spectrum with the sinc^2-function of the conversion phase matching function, resulting in a 101.3 GHz spectrum. As before, Fourier transform of this spectrum (represented by a red solid line in the same figure) is used to compare to the measured coherence function, demonstrating close agreement and thus validating our results.

Franson interference

In the following, we present Energy-time entanglement of 854 nm and converted 1310 nm photons using Franson's two photon interference [56]. The set-up for its implementation is presented in Fig. III.6. As before, broadband SPDC photon pairs at 854 nm are generated and further split using a PBS. Transmitted 854 nm photons are sent into the Michelson interferometer (MI) described in the previous section and further detected using an APD (Perkin-Elmer), while at the converter side (reflected photons) photons are converted following the procedure described earlier and furthermore sent into a unbalanced fiber Mach-Zehnder interferometer (MZI) equiped with a phase modulator (Phoenix Ph.), after which photons are detected using a SSPD (Single Quantum). An interferometer unbalance of 1.14 ns is chosen, which is much longer than the photon coherence time measured in the previous section and shorter than the coherence time of the pump beam, which is below 2 MHz bandwidth, thus fulfilling requirements discussed earlier for two-photon state interference. After balancing both interferometers coincidences are registered as in Fig. III.8. A 512 ps central window for indistinguishable paths is chosen for the state III.2 as discussed

in the previous section. Franson interference fringes in the coincidences are observed scanning the piezoelectric displacement in M2 (phase scan), for a fixed unbalance of the interferometers. Following this procedure a maximum visibility of 80.7 ± 6% is found. Furthermore, the phase of 854 nm interferometer is kept fix and fringes are scanned for both additional scenarios meaning only phase changes at the fiber interferometer and finally simultaneous phase changes, as shown in Fig. III.7. This way, the effect of relative phase changes over the combined coincidences is shown.

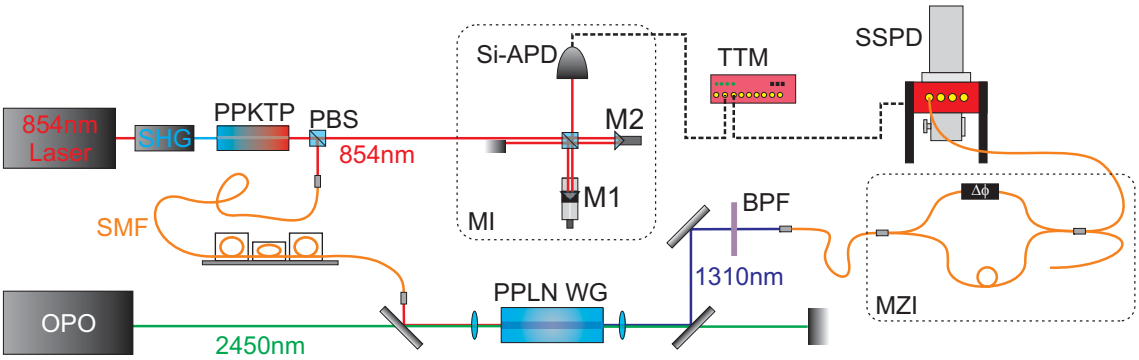

Figure III.6: Setup for Franson interference using 854 nm and frequency converted 1310 nm photons. Broadband 854 nm photons are sent into a Michelson interferometer (MI) and photons are detected using a silicon APD (Perkin-Elmer). At the converter side photons are converted and furthermore sent into an unbalanced fiber Mach-Zehnder interferometer (MZI) and photons are detected using a SSPD (Single Quantum). See text for details

First-order coherence function of the photon pair (eq. III.2.2) is measured following a similar procedure to the single-photon case (considering coherence constrains), but this time looking at coincidences instead of single interferometer detections. Visibility of Franson interference fringes in the coincidences is measured as a function of the interferometers unbalance by stepwise displacements of the mirror M1 of the MI interferometer, while phase scans are performed at M2 and phase at the MZI is kept fix. Results are shown in Fig. III.8.

Following equation III.2.2, the first-order coherence function of the photon pair state depends on the individual coherence functions of each photons. Using the functions measured in the previous section, $F(\tau)$ is calculated and compared (solid red line) to our measured data performing a peak height fit. A pair coherence time of $\tau_{\text{pair}} = 12.4\,\text{ps}$ is determined. This result shows a remarkable agreement of the individual coherence functions measured independently for the photons with the two-photon state function obtained using Franson interference. Furthermore, we analyze the quality of our Energy-time entanglement by looking at the detected visibilities. A maximum visibility for Franson interference of 80.7±6% was found, which exceeds by far the 50% expected for classical states [88]. More importantly, Bell inequality for Franson interference [89] sets an upper boundary for the visibility of $V \leq \frac{1}{\sqrt{2}} \approx 70.7\%$, meaning we observe a violation by 1.66 standard deviations. Background subtraction increases the maximum visibility to 84%, which coincides with the maximum expected for our interferometers. From calibration measurements $V_{max} = 0.88 \cdot 0.95 = 84\%$, ergo we believe our photons are maximally entangled although in our results this is limited by the measurement apparatus.

This results represent an important step further in the use of photonic interfaces. Although

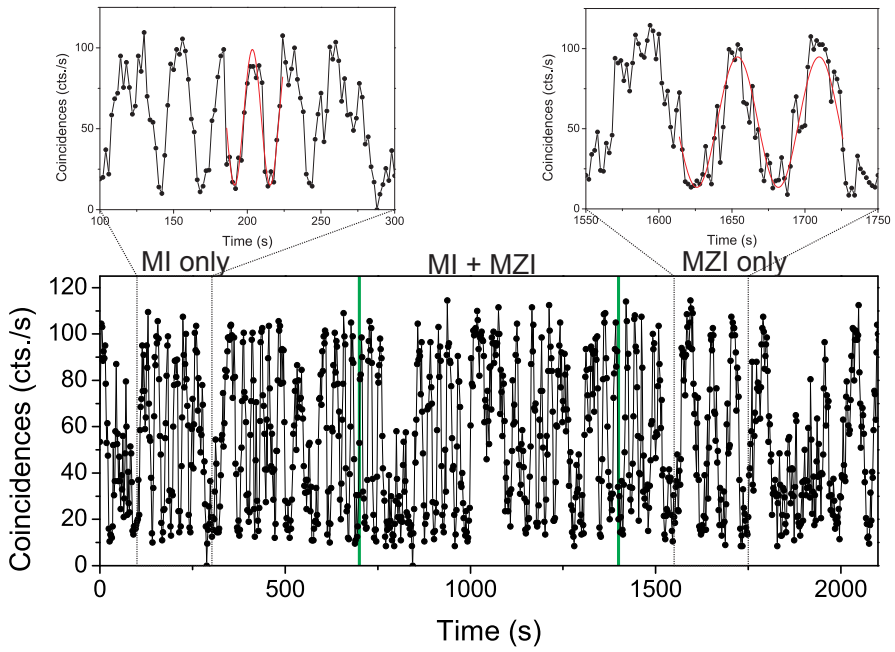

Figure III.7: Franson interference fringes in coincident detection while scanning the interferometers phase. The insets show oscillations in the coincidences in regions where only the Michelson interferometer or the Mach-Zender interferometer are scanned. Sinusoidal fits (red) are used to determine the visibility of Franson interference.

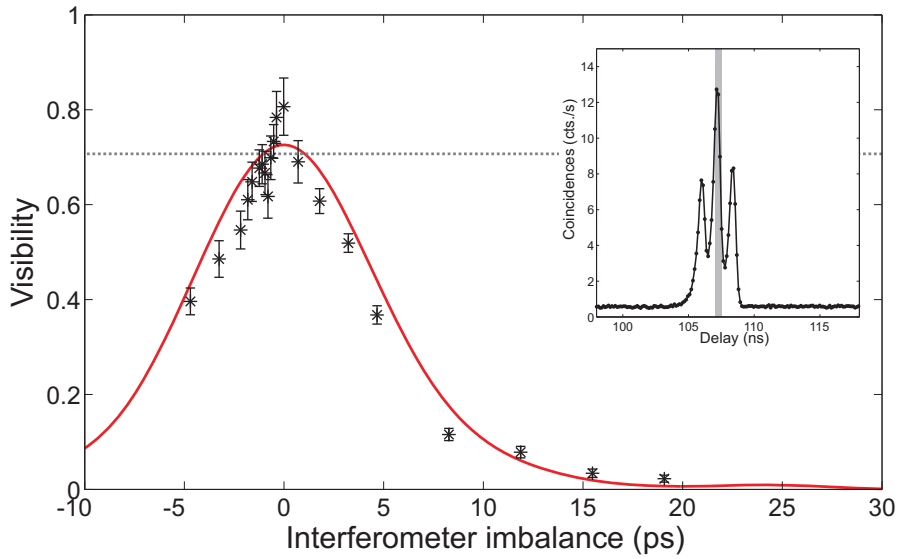

Figure III.8: Two-photon coherence function. Solid red line is the function III.2.2 calculated using individually measured first-order coherence functions. The dashed line represents 71% visibility for Bell inequality violation. The inset shows photon coincidences between both interferometers. A 512 ps window for post-selected Franson interference is used (gray).

energy-time entanglement for up-converted photons has been already shown [15], these are the first results for frequency down-conversion and further for memory-compatible photons, opening a broad range of possibilities for networking schemes. Moreover, coherence function of single photon states and photon pair have been shown successfully for the interface, in good agreement with expectation from spectral analysis. A similar experiment with narrowband photons would be desirable, but due to the long coherence time of the narrowband photons implementation of such an experiment is out of our possibilities.

III.2.3. Heralded $g^2(0)$ measurements

In the present section we analyze the single-photon characteristics of our interface and its heralding properties. An ideal single-photon source produces pure single-photon Fock states on demand. Usually these conditions are obtained with single atoms or atom-like quantum systems, which are excited with very high probability at a given time by an excitation pulse (i.e. laser pulse), emitting a photon at a rate typically limited by the decay time of the excited transition (in the optimal Fourier-limited case, the duration of the photon wavepacket) [90]. Single-photon emission of our single ion has been shown in a series of experiments, at different transitions and with different tailorable spectral, temporal and polarization properties [23, 25, 24]. However, for continuously pumped SPDC sources photon generation occurs at random times. Typically one photon of the pair, the 'herald' is used to announce the presence of its partner, the heralded single-photon (eq. I.2). Although statistics of SPDC generation follow thermal statistics [91], once detected, the herald projects its partner into a state close to a single-photon Fock state [92]. This is normally the case for low pump power, as probability of generating multiple pairs is reduced. Second-order correlation function $g^2(\tau)$ gives one information about the statistics of photon emission and is used for its characterization. In particular, $g^2(0)$ values tell us how close are we from an ideal photon source, for which $g^2(0) = 0$, meaning the source does not generate more than one photon at a time [93]. The second-order correlation function $g^2(\tau)$ is defined as

$$g^2(\tau) = \frac{\langle E^-(t)E^-(t+\tau)E^+(t+\tau)E^+(t)\rangle}{\langle E^-(t)E^+(t)\rangle^2} \tag{III.5}$$

where E^+ and E^- are the Hermitian conjugate operator components of the quantized electromagnetic field. Commonly it is measured by sending the photon-stream into a Hanbury-Brown & Twiss (HBT) interferometer where the field is divided in two paths using a beam splitter where coincidences are detected. If the source is a true single-photon source, meaning no coincidences should be detected at zero time delay.

For SPDC, a triple-coincidence experiment is performed, since detections at the HBT are heralded. For this purpose one splits the original pair with a PBS and use a Hanbury-Brown & Twiss (HBT) interferometer in one of the SPDC arms to further correlate its detection events with the heralding partner photon. This is the procedure we use here to characterize our heralded photon source.

For calculating $g^2(0)$ values we follow the method described by Fasel in [51] and we used M. Bock's implementation [94]. This method reorders the data in bins according to the number of heralds detected between two detection events at the different arms of the HBT within a certain time window. Central bin n=0 represents cases where no herald is detected between these events meaning

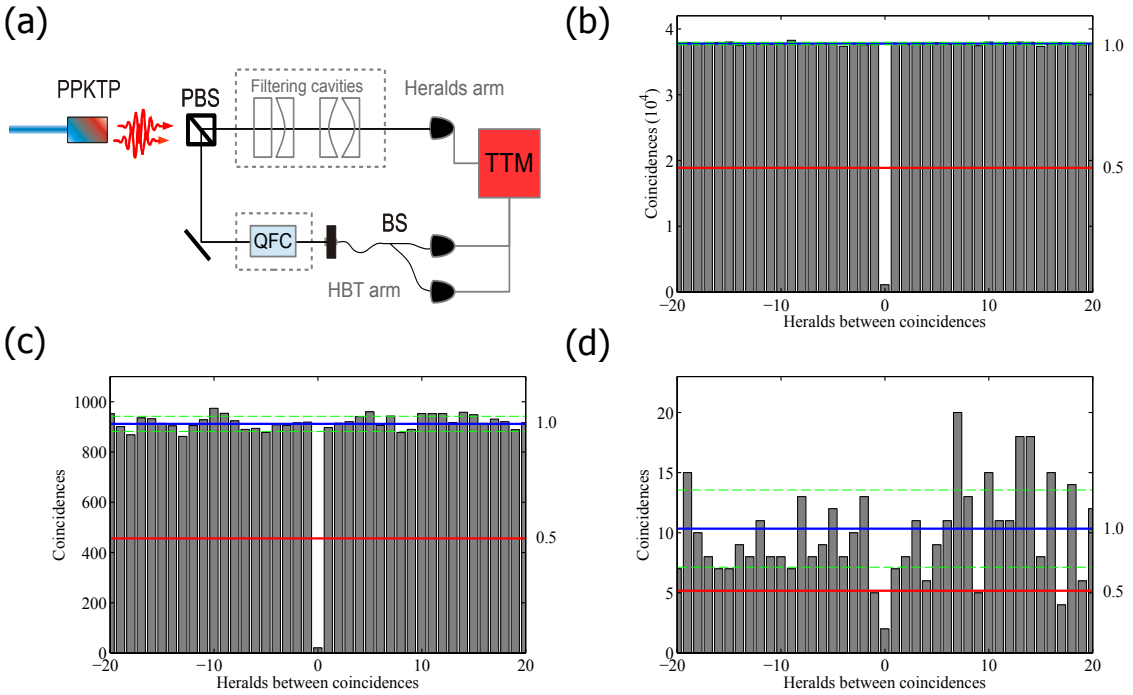

Figure III.9: a) scheme for the heralded $g^2(0)$ measurement. Fiber based HBT is implemented in one arm. As before, APDs are used for 854 nm photons detections and a SSPD is used for converted telecom photons. Three different configurations are studied, triple coincidences of original SPDC photons (b), using quantum frequency conversion (c), and converted narrowband photons (using filtering cavities) (d). Blue lines represent average coincidences and red lines represent $g^2(0) = 0.5$ boundary for classical states of light. Green lines correspond to a standard deviation. See text for details.

no triple coincidences take place. For an ideal single-photon source one herald is expected for every photon detection at the HBT meaning this bin should contain no events. In our experiment, $g^2(0)$ values are obtained by comparing the central bin with the average triple-coincidences contribution of the surrounding 200 bins, without background subtraction.

As seen in figure III.9 we have performed three sets of measurements: triple coincidences for the original broadband 854 nm photons, for converted photons, and finally for narrowband-converted photons. As for time correlations measurements shown earlier, original SPDC photons are split using a PBS. Horizontally polarized photons are used as heralds while vertically polarized photons are sent into a fiber based HBT and detected using APDs for 854 nm photons detections and a SSPD is used for converted telecom photons. (Fig. III.9a). Time correlations between individual arms of the HBT and the heralding arm are evaluated as shown in section III.2.1 in order to determine time offsets for triple coincidence detections and time windows are chosen for finding an optimal value of $g^2(0)$ in post-selection. A boundary at $g^2(0) = 0.5$ sets the limit for non-classical states of light, meaning below its value we observe photon anti-bunching, as expected for a single-photon source.

We look at triple coincidences of 854 nm broadband SPDC photons (173 GHz bandwidth) using an 854 nm fiber beam splitter in the HBT arm. We set a reduced 0.5 mW pump power in order to

avoid APDs saturation, detecting a rate of 129 700 heralds and ~50 000 photons per second in each arm of the HBT. We evaluate triple coincidences within a 6 ns time window for which we obtain $g^2(0) = 0.0293 \pm 0.0003$. The resulting histogram is displayed in Fig. III.9(b) which corresponds to 15 minutes measurement time. The temporal extension of this photons is ~3 ps meaning we are limited by the jitter of the detectors (as seen previously).

In the second measurement and as described earlier, vertically polarized photons are sent for frequency conversion. Converted photons are split using a telecom fiber BS and detected using two channels of our SSPDs. These HBT detections are heralded by unfiltered 854 nm partner photons. Converted photons have a time extension of about 5 ps, thus we are again limited by the resolution of our detectors. Once more a low pump power of 0.5 mw is used, leading to a similar rate of detected heralds (113 480 s^{-1}) while ~3 500 s^{-1} at each SSPD channel for 78 minutes measurement time. Evaluating the data for a window of 6 ns results in $g^2(0) = 0.021 \pm 0.005$. The corresponding histogram is shown in Fig. III.9c.

In the last measurement of this set (Fig. III.9d) we look at the triple coincidences of filtered-converted photons, namely coincidences between narrowband 854 nm heralds and frequency-converted 1310 nm photons. Due to energy conservation of the SPDC process, coincidences correspond to 22 MHz photons whose time structure (7 ns length) we have observed in the previous section. In this case, additional to losses at the converter, spectral selection and transmission of the filtering cavities decreases strongly the heralding rate (three orders of magnitude reduction). For a maximum pump power of 55 mW, an heralds rate of 784 s^{-1} was detected vs ~30 000 s^{-1} detections in the SSPD channels, in a measurement time of 426 minutes. We detect a low triple coincidences rate for multiple heralds bins (10.3 on average, blue line in Fig. III.9d), which increases the uncertainty of our measurement. However, single-photon characteristics are still observed for these narrow-band photons with $g^2(0) = 0.19 \pm 0.14$ which including deviation stays within the anti-bunching region. As in the previous histograms a time window of 6 ns has been used which corresponds to the optimal length for this data set, close to the length of the narrowband photon. Time-window dependence is shown in Fig. III.10 for different evaluations.

As discussed in the previous section, spectral (and thus temporal) properties of the detected photons are different (3 ps, 5 ps and 7 ns respectively). As we are limited by detectors resolution (600 ps) we chose the longest time window for comparison with narrowband photons. However, we also re-evaluate the data of the two first measurement for shorter time windows looking for the best $g^2(0)$ values for each case, since the temporal length of these broadband photons is much shorter than the 6 ns time window used for the narrowband photons. This way, we find $g^2(0) = 0.0077 \pm 0.0007$ for the unfiltered unconverted 854 nm photons for a time bin of 750 ps and $g^2(0) = 0.0074 \pm 0.0037$ for the unfiltered-converted photons, using a bin size of 1.5 ns, showing a good agreement between them.

Experimental conditions are at every step also different. For the first measurement losses correspond only to coupling efficiency while for unfiltered converter photons additionally fiber transmission (63%), filtering effect of the frequency converter (~50%) and conversion efficiency (8%) have to be included at the HBT arm. For the third measurement, strong decrease in the heralding rate due to spectral filtering is introduced although in this experiment the filtering effect of the frequency converter at the HBT arm instead of decreasing the signal serves as background reduction filter for the remaining broadband SPDC photons outside the 22 MHz selected spectrum

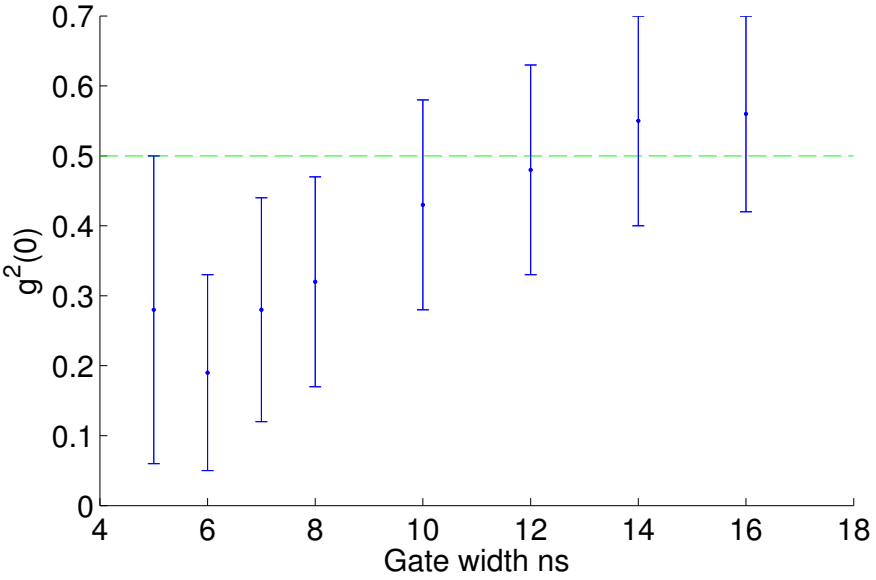

Figure III.10: $g^2(0)$ of narrowband photons as function of post-selected time window for triple coincidences. Optimal value was found at 6 ns, close to the 7 ns photon length. Green dashed line marks non-classical limit.

(~50% of the SPDC background). For both measurements with frequency conversion a constant rate of about 2000 detections corresponding to residual background photons generated at the converter are observed on each arm of the HBT.

As to be expected for a typical SPDC source, unfiltered 854 nm photon have shown a successful heralded single photon-source behavior. After quantum frequency conversion single-photon characteristics behave accordingly, meaning our interface works as a good telecom-heralded source with $g^2(0)$ values comparable to other SPDC sources [51, 95]. We have also shown that heralded single-photon characteristic of the narrowband photons (22 MHz) is still visible despite strong signal reduction after applying spectral selection and frequency conversion.

To conclude this section, we have observed a series of non-classical properties of our SPDC-QFC interface including time correlations, energy-time entanglement and heralded single-photon characteristics. These measurements show that they are versatile and powerful tools for quantum network experiments. Moreover, a very important property of this interface is their working wavelengths that permit the use of memory wavelength photons while heralding in the low-loss telecom band. In the further section we apply this interface in a extended scenario to study the telecom-heralded single-photon to single-atom interaction.

III.3. Photon-ion interaction

A single trapped $^{40}Ca^+$ ion is a robust system for quantum information processing and network node of a quantum network [37, 64, 29]. In this context combination of a photonic-telecom interface with such a node is a promising candidate for integration of quantum communication and information

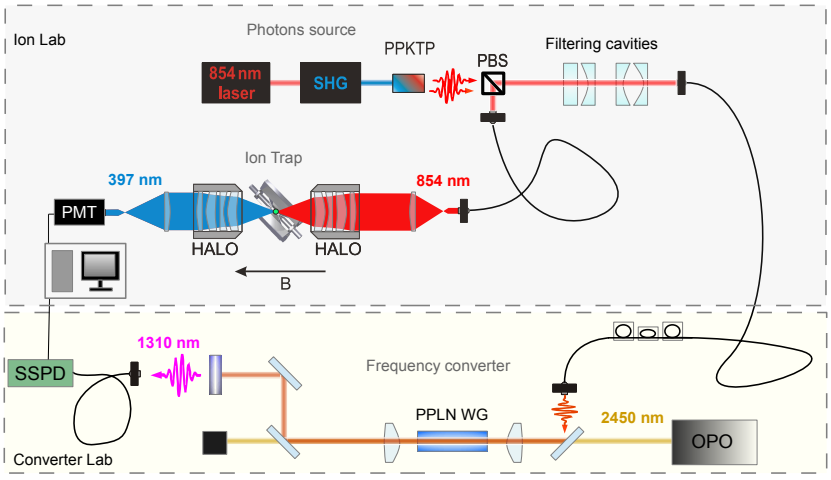

Figure III.11: Schematic of the experimental apparatus composed by a heralded photon source, a single trapped $^{40}Ca^{+}$ ion ion and a quantum frequency converter. The SPDC photon source and ion trap are located in the same laboratory (ion Lab). Photons from a SPDC pair are split using a polarizing beam-splitter (PBS) and sent onto the ion through a single-mode fiber channel, while their triggering partners photons are transmitted through filtering cavities, coupled into a 90 meters fiber channel and sent into the converter laboratory placed in a different floor. At the ion, 854 nm photons from the source are polarization adjusted and sent onto the ion through one of the HALOs (high-numerical aperture laser objectives, $NA = 0.4$) along the quantization axis (defined by the magnetic field direction, $\vec{B}$). At the converter, triggering heralding partners are overlapped with a strong optical parametric oscillator (OPO) pump and coupled into a PPLN waveguide for single-photon frequency conversion into the telecommunications band at 1310 nm. The 16 Hz experimental sequence is ran at the ion where fluorescence emission is detected using photomultiplier tubes (PMTs, Hamamatsu) while 1310 nm converted photon are detected continuously with a superconducting single-photon detector (SSPD, Single Quantum). Detections during an absorption window of 44 ms are registered using time-tagging electronics for further correlation analysis (Picoharp 300, Picoquant).

processing. In the following experiment, we combined the SPDC source, frequency converted and trapped ion into a single network-like experiment. Previously, we have shown that the intrinsic time correlation shared by a SPDC photon pair is preserved in the absorption of single photon by a single trapped ion and that this allows one to trigger the absorption process [19]. As temporal correlation of a narrowband SPDC pair is also preserved by frequency conversion, we thus use QFC for enhancing the capabilities of this photon-atom interface into the telecom band. Photons from the SPDC source are sent onto a single ion for absorption, while their partner heralding photons are filtered for selecting resonant photons and furthermore sent to the frequency conversion setup described earlier for heralding their absorbed partners in the telecom band. The setup is shown in Fig. III.11. Coincidences between a telecom-converted herald and an absorption-induced quantum jump by the ion mark a telecom-heralded single-photon absorption. This way we have extended the heralding of a SPDC single-photon absorption to the telecom band [19], making it compatible with long-haul transmission.

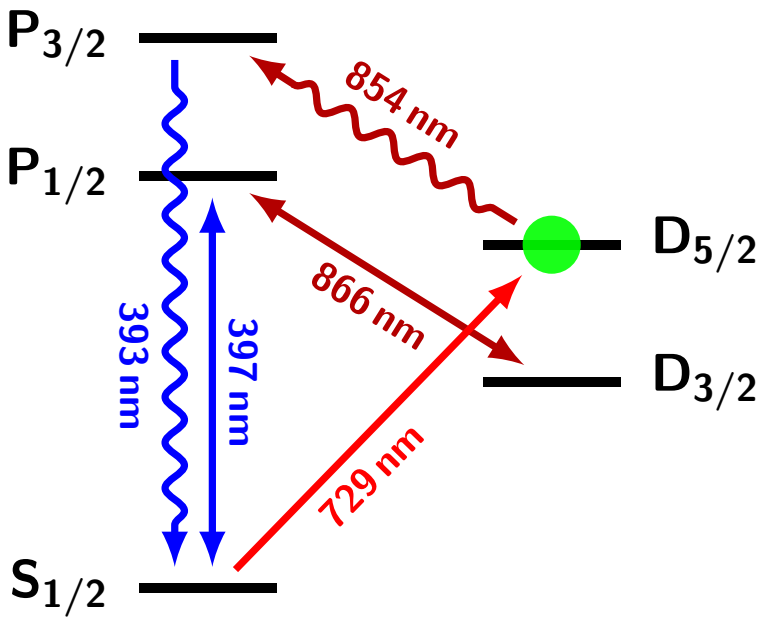

Figure III.12: Relevant levels and transitions of the $^{40}Ca^{+}$ ion. Lasers at 397 nm and 866 nm are used for Doppler cooling and detection of quantum jumps (fluorescence). Lasers at 729 nm and 854 nm are used for optical pumping and state preparation. The single ion is prepared into the $D_{5/2}$ metastable state for absorption of 854 nm SPDC photons. Upon a photon absorption, the ion decays into $S_{1/2}$ ground state and onsets the emission of fluorescence which is induced by the presence of cooling lasers. Time traces of dark-to-bright transitions allows one to identify when an absorption has occurred and they are further correlated with converted photons detections.

Our ion trapping apparatus was described in section I.1, and corresponds to a linear Paul-type ion trap where a single $^{40}Ca^{+}$ ion is trapped [19, 21]. Two high-numerical-aperture laser objectives (HALO lenses, N.A=0.4) are placed along one of the axes of the trap for enhancing photon-ion coupling. SPDC photons are sent along this axis, which in this case also corresponds to the quantization axis, defined by the magnetic field direction ($\vec{B}$, Fig. III.11). While one of the HALOs is used for focusing 854 nm SPDC photons onto the ion, both of them are used to collect 397 nm fluorescence. The ion is prepared into the $D_{5/2}$ metastable state, with a lifetime of $\sim$ 1.1 s. An SPDC photon absorption excites the ion from $D_{5/2}$ into $P_{3/2}$ decaying with 93.5 % into the $S_{1/2}$ ground state, given by the branching ratio of the $P_{3/2}$ state. Once in $S_{1/2}$ the presence of cooling lasers induces emission of fluorescence used to signal the absorption-induced quantum jump. Relevant levels are shown in Fig.III.12.

Experimental sequence

The experiment runs at 16.7 Hz repetition rate and is subdivided in different phases, as shown in Fig. III.13. The sequence is started performing Doppler cooling by shining in 397 nm and 866 nm laser light for 100 µs. Furthermore, optical pumping into $|m = -\frac{1}{2}\rangle$ Zeeman sub-state of the $S_{1/2}$ ground state is performed (60 µs), after which the ion is prepared with > 99 % measured probability

into $D_{5/2}$ using a series of four 729 nm laser pulses (40 µs).

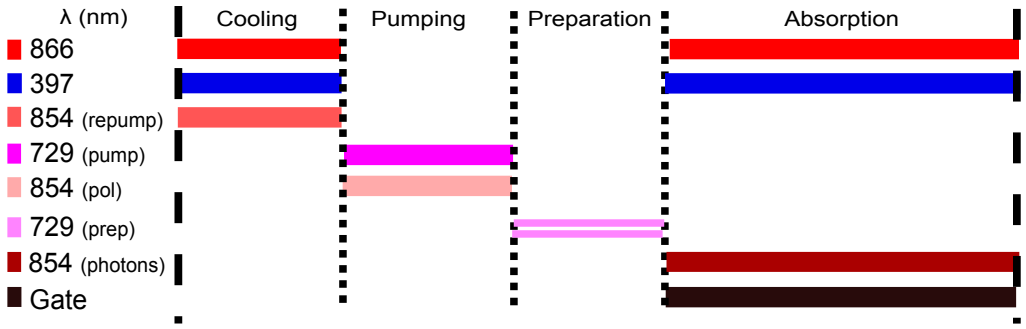

Figure III.13: Sequence for the telecom-heralded absorption of SPDC photons. Absorption induced quantum-jumps are detected during the absorption window and further correlated with telecom-converted partners. See text for details.

Furthermore, an interaction window of 44 ms is opened and SPDC photons are sent onto the ion at a rate of $\sim 4\,000\text{s}^{-1}$. Polarization of photons has been set to σ^+ in the ion's reference frame this way exciting the ion from $D_{5/2}$,$m = -5/2$ to $P_{3/2}$, $m = -3/2$, which has the highest absorption probability for this transition.

During this window, 397 nm and 866 nm cooling lasers are activated and fluorescence emitted upon the absorption of an SPDC photon is collected through the HALOs and detected using two photomultiplier tubes (PMTs, Hamamatsu). Quantum jumps produced by the photon absorption is then signaled by the onset of fluorescence (dark-to-bright transition) and it is time-traced for its further correlation with telecom-partners of the absorbed photon. The time correlation between quantum jumps events and telecom heralds is shown in Fig. III.14(b). The central peak at zero time delay corresponds to coincidences between an SPDC-induced quantum jump in the ion and the detection of its converted partner, marking thus the telecom-heralded single-photon absorption. Slopes modulating the background at both sides of the correlation peak correspond to the shape of the expected time-correlation function between telecom photons and quantum jumps detections, given by a constant photons detection rate and an exponential decay function, respectively. The exponential decay function in Fig. III.14(a) shows the quantum jumps detection distribution within the interaction window, whose time constant represents the effective lifetime of $D_{5/2}$ state in presence of resonant SPDC photons ($\tau_{\text{eff}} = 0.08550(5)$s). Detection events were integrated for 1957 minutes where 852 coincidences were found (background subtracted). Effective interaction time is given by the 44 ms absorption window of each cycle corresponding to a 73% of the total measurement time, leading to $9.9 \cdot 10^{-3}\text{s}^{-1}$ coincidences for the combined experiment. For 7.1 μs time bin, the resulting signal-to-background ratio (SBR) is 0.04 and corresponding signal-to-noise ratio (SNR) 6, calculated for the central bin. Hence we see that the peak significantly exceeds the 95% confidence boundary of noise events, represented by green lines in the plot. Average background is $1.90 \cdot 10^4$ per bin which agrees with the $1.89 \cdot 10^4$ expected from accidental coincidences, as calculated from the singles rates using equation II.6. Background counts arise from coincidences between lost partners, uncorrelated noise of the converter and dark counts. Details are given in the following section.

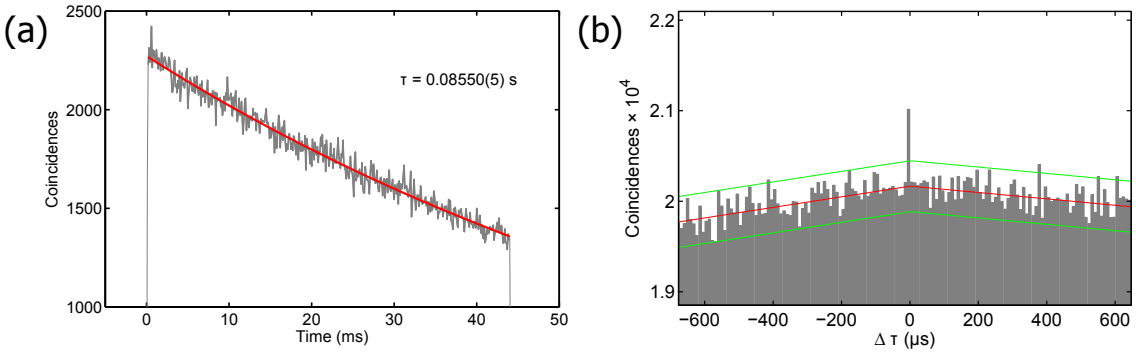

Figure III.14: (a) Quantum jump distribution during the absorption window. τ represents the effective lifetime (1/e) of the $D_{5/2}$ in presence of SPDC photons. (b) Coincidences histogram for telecom-heralded single photon absorption by a single calcium ion. The peak at zero time delay corresponds to coincidences between a quantum jump by the ion and a detected telecom-heralding photon. Slopes at both sides of the correlation peak correspond the the expected correlation function between quantum jumps and converted photons. Red line represents average background and green lines the 95% confidence boundary.

III.4. Efficiency considerations

At maximum power of 53 mW about 6000 s^{-1} ion-resonant photon pairs are generated at the SPDC source for the interaction experiment. Considering transmission losses including the filtering stage ~1500 s^{-1} narrowband photon arrive at the frequency converter out of which about 80 arrive at the SSPD. Out of $2.79 \cdot 10^8$ total detections at the SSPD during the whole measurement time, only ~ 1% correspond to converted 854 nm photons. Excluding a typical rate of 300 SSPD dark counts per second, it means an average of ~2000 s^{-1} residual uncorrelated photons produced at the converter which still arrive at the detector. The effect of uncorrelated noise photons is also dimensioned by calculating the probability of a successful ion absorption per telecom detection (eq. II.3), $P_{\text{tel}} = 4.1 \cdot 10^{-6}$. If we consider the heralding probability for the estimated converted photon detection rate without background, this probability should be $P_{\text{conv}} \sim 4 \cdot 10^{-4}$.

On the other hand, ~4 000 photons per second were sent onto ion for absorption through one of the HALOs. At the ion, out of 1 961 424 experimental cycles 874 697 quantum jumps have been detected. Neglecting bad state preparations (<1% from calibration measurements) this represents a decay probability into $S_{1/2}$ of 44.59(4)% per experimental cycle. Taking into account spontaneous emission contributions of the metastable $D_{5/2}$ into $S_{1/2}$ ($\tau_{sp} \approx 1.1$ s), 93.2% of the quantum jumps are attributed to SPDC photons, corresponding to an absorption rate of 12.5 abs./s A parallel analysis is performed from histogram of Fig. III.14(a) by comparing the effective lifetime measurement ($\tau_{\text{eff}} = 0.08550(5)$) with the natural decay time of the $D_{5/2}$ state, leading to an absorption rate of 11.6 abs./s, which is in agreement with the previous calculation. From these values, an absorption efficiency for SPDC photons of $\sim 3 \cdot 10^{-3}$ is estimated.

Finally, expected losses in each arm are $\eta_{\text{ion}} = 2.1 \cdot 10^{-3}$ and $\eta_{\text{conv}} = 4.3 \cdot 10^{-3}$ at the ion and converter side respectively. Taking into account known losses a coincidence rate of 0.019 coinc./s is expected in the interaction time, which is 2 fold higher than the detected rate. Difference with the estimated value is attributed to a combination of the following facts: instability of converter's OPO

pump, which affects proportionally the conversion efficiency, polarization sensitivity of the SSPD, which decreases detection efficiency and finally alignment and polarization of SPDC photons at the ion side due to thermal drifts.

III.5. Telecom wavelength multiplexing using frequency conversion

We have shown that QFC is a powerful tool for enhancing the capabilities of our SPDC source. We were able to trigger a single-photon absorption by a single-ion because the temporal correlation of the photon pair is maintained. Moreover, we have further set an experimental realization for combination of classical and non-classical pulses in a common telecommunications channel and this way show the versatility of our interface in a more general network scenario. For quantum communication not only quantum information must be send, but also classical information must be conveyed for instance for transmission of a key or communicate the outcome of a projective measurement for teleportation [96, 97]. This makes the use of a common channel for transmitting both very practical, as it is done for in classical telecommunications. Although transmission for telecommunication wavelengths is not a big challenge, cross-talk between different signals can in the spoil the quantum information, which is much more vulnerable to the interaction with the environment. We tested a method for transmission of both types of states through a common channel by using wavelength multiplexing in the telecom band of a non-classical state triggered by a time-correlated optical pulse. This results have been published recently in [85] and presented here in the appendix B.2 in draft format. A brief description is given here for completeness.

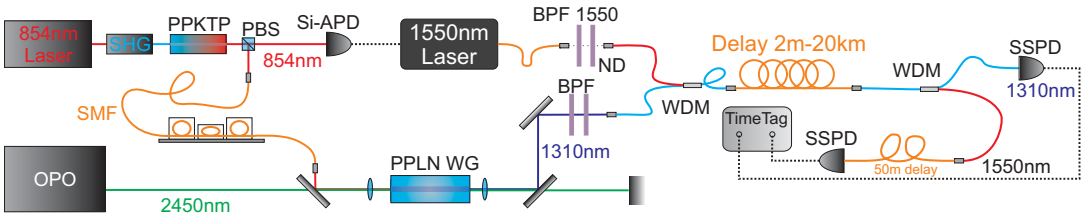

Figure III.15: Setup for multiplexing of telecom signals. O-band photon and C-band pulse are transmitted through a common fiber and retrieved using WDMs. Detection is performed using two channels of an SSPD. See text for details.

The experimental setup is shown in Fig. III.15. As in previous experiments, photon pairs are generated at 854 nm and split using a polarizing beam splitter for heralding purposes. This time no filtering is used, meaning broadband 3 ps photons are generated. While photons traveling through the transmitted port of the PBS are directly detected at the APD, reflected partner photons are sent for frequency conversion into 1310 nm as described in the previous sections. 854 nm APD detections are used to trigger 1550 nm laser pulses using a Thorlabs LPSC-1550 unit. Bias voltage of the laser is adjusted just below threshold such TTL pulses created by the APD trigger the creation of a pulse. The created pulse is seen in Fig. III.16(c). At this point we have a single 1310 nm O-band converted photon with a correlated triggering C-band laser pulse at 1550 nm. Band pass filter are used on both arms to decrease residual emission into other wavelengths. Furthermore, both wavelengths are combined and transmitted into a standard telecom fiber (SMF-28) using a telecom wavelength-division multiplexer (WDM, Thorlabs DET10C) with 16 dB isolation between bands. After fiber

transmission (2 m or 20 km) signals are de-multiplexed using an analog WDM for detection in separated wavelengths. Initially our intention is to detect laser pulses using a photodiode at 1550 nm, but under these conditions cross-talk of the laser pulses into the single-photon channel screen any correlation. Thus, laser pulses are attenuated in six orders of magnitude to reach a similar rate as in the single photon channel and both signals are measured using two channels of our superconducting-single photon detector (SSPD). A calibration measure is performed by blocking single photon to identify remaining cross-talk between channels and furthermore detections are measured on both arms. Results of the correlations for 2 m and 20 km separation are shown in Fig. III.16. Dispersion of the peaks and correlations observed are according to our expectations.

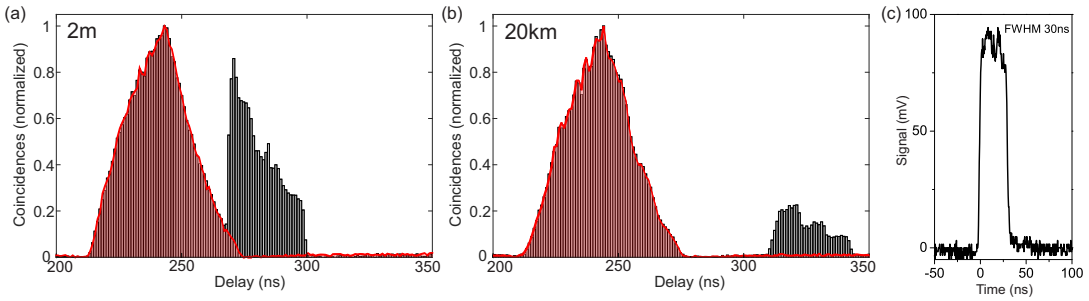

Figure III.16: Correlation of multiplexed single-photon in the O-band and heralding pulse in the telecom C-band. (a) Time correlation for 2 m delay. (b) Correlation after 20 km of fiber. Red shaded area is the calibrated cross-talk remains of the C-band. Shaded gray area represents the correlation between the multiplexed signals. (c) Generated laser pulse triggered by an 854 nm APD detection TTL.

For the interested reader, details are described in sec.B.2 . Although attenuated pulses had to be used for avoiding cross-talk, this is successful proof-of -principle test of wavelength multiplexing of classical and quantum signals in a common channel.

III.6. Conclusion

We have shown a series of successful experiments using a photonic SPDC-QFC interface. QFC have been tested in different scenarios completing a set of ingredients necessary for the implementation of a quantum communication network. In practical terms, by frequency conversion from 854 nm into 1310 nm fiber transmission attenuation has been reduced from 2dB km to 0.25dB km enhancing remarkably information transmission capabilities of our original SPDC source.

Time correlations between the detection of a converted photon and a quantum jump in a single ion haven shown a successful telecom-heralded single-photon absorption (Fig. III.14). As we have shown in the previous sections, this is possible since quantum frequency conversion preserves non-classical characteristics of the SPDC photons as heralded single-photon generation, time correlations and energy-time entanglement. Furthermore, quantum frequency conversion makes heralding compatible with existing telecom-fiber infrastructure; thereby this work is an important step towards the implementation of a hybrid quantum network of atomic memories connected by low-loss photonic quantum channels.

Further goals might include the detection of the single 393 nm photon emitted by the ion and its further correlation with telecom heralds as in the previous chapter. Different from quantum jumps detections, its detection avoids the destruction of the final state of the ion, which happens when looking at the fluorescence [30]. Since the collection efficiency of such photons is only $\sim 2\%$, some improvements in the setup are required: one alternative is improving the SPDC generation rate since this single-pass bulk source provides only $\sim$100 coupled narrowband photons pairs per second, which could be increased by two orders of magnitude using cavity enhancement [98] or using a state-of-the art waveguide source [72, 50], as discussed previously. These figures are further discussed in the following chapter.

Furthermore, this proof-of-principle experiment demonstrated a low heralding efficiency using telecom photons. At the QFC device there are two main ways to improve this fact . Conversion efficiency is currently limited by the available pump power coupled into the waveguide, which will be improved by using specially tailored aspheric lenses made of ZnSe. Increase in the conversion efficiency is in a good approximation linear, meaning a feasible increase of pump coupling efficiency up to 80% would mean a conversion efficiency of $\approx$17%. On the other hand we plan to reduce the noise at the output of the QFC device. At the moment the filtering stage has a bandwidth of 12 nm. By using a fiber Bragg grating as in [78], the background which exhibits a mostly flat spectrum could be reduced by two orders of magnitude, then being comparable to the detected signal rate. Instead of filtering the photons before conversion, a stabilized filtering stage with a bandwidth of 22 MHz in the telecom O-band would practically eliminate all background. Furthermore, at the ion improvements could include the focusing/collection with higher NA objectives or aided by cavity coupling [62, 99].

To conclude, despite low photon rates, added noise and limited conversion efficiency affecting the signal-to-background (SBR) on the different experiments, we have shown significant results for the implementation of a photon-atom based quantum network using frequency conversion, paving the way for future development. Although we have shown energy-time entanglement-preserving conversion, a promising goal is to develop a polarization insensitive QFC setup to convert ion-compatible polarization qubits. Polarization entangled photons from the pair source could thus be sent either to the ion and stored there and on the other hand the partner could be converted to a telecom wavelength polarization qubit for long-range transfer of atom-photon entanglement.

In the following chapter we present an additional experiment for heralding our atom-photon interface in the telecom region by generating photons directly in the telecom band using an OPO-source. We will discuss advantages and drawbacks of both approaches and look at the figures of merit.

Chapter IV

Telecom-heralded single-photon absorption using an OPO source

One of the most important challenges for the implementation of a quantum communication network is the compatibility of memories with long distance communication. As discussed in the previous chapter, the use of photons in the telecommunications band in combination with atomic memories a very attractive candidate for its implementation, especially because of low losses in the telecom band and robust repeater schemes for atomic memories. Quantum frequency conversion is a versatile and universal tool since translation of wavelength allows one to connect any quantum systems working in the optical region for storage or transmission purposes. Nevertheless limited conversion efficiency and increased noise of the conversion process are drawbacks to be considered for its implementation. Another approach is using systems which work directly at telecom wavelengths. Examples of these are solid states memories with telecom transitions, whose recent development is impressive [73, 72, 16, 75], although capabilities as information processors are still to be developed for them. This fact makes atomic systems like trapped ion very attractive. On the other hand, non-degenerate SPDC sources are versatile tools for connecting these systems to a network: while a photon of the pair is set to the desired target transitions at the memory, its partner at telecom band could be used to swap entanglement to nodes at distant positions [9, 100]. This type of repeater schemes based on SPDC have been proposed a few years ago [12, 101] and several new schemes have been investigated [102, 103]. As discussed in the references and previous chapters, due to typically poor overlap between SPDC photons and memory spatial modes, a high rate of photons is desired, which seems to be possible for waveguide SPDC sources or cavity enhancement. An additional constraint is narrow bandwidth of atomic transitions, which for waveguide emission means strong spectral filtering of generated photons to match this bandwidth. On the other hand, a cavity enhancement approach allows one to generate narrowband photons naturally, making it an ideal candidate for this type of experiments. In this chapter we present results following this strategy, where an optical parametric oscillator source is operated below threshold for narrow-band high-brightness SPDC generation and used for heralding the absorption of a single-photon by a single trapped $^{40}Ca^{+}$ ion. Implementation and characterization of this source has been broadly covered in the works by M. Bock and A. Lenhard [94, 58] and is thus revised here summarized. Results concerning the ion interaction which is part of this doctoral work are published in [74] and presented in this thesis as an appendix (B.3), and are contrasted here with previous interaction experiments with the ion.

IV.1. OPO Source

The optical parametric oscillator (OPO) is based on a 30 mm periodically poled MgO-doped lithium tantalate crystal placed in a bow-tie ring cavity. It is pumped at 532 nm using a frequency-doubled solid state laser (10 W max.) and thanks to a set of 6 different poling periods, a wavelength range from 1202 nm to 1564 nm for idler photons and from 806 to 954 nm signal wavelength can be chosen, meaning its tunability covers widely the telecom (O, E, S and C bands) for the signal photons while several quantum memory wavelengths for the idler (Ca, Cs, InAs/GaAs). For our experiments below-threshold conditions for SPDC generation at a pump power of 300 mW are driven, with signal wavelength at 854 nm for which the cavity is resonant, and idler wavelength at 1411 nm for which the cavity is transmissive. Cavity effects on the photon's shape are seen in a coincidence measurement in Fig IV.1. A ring-down time of the cavity of 22.7 ns is observed, which corresponds to a 7.2 Mhz bandwidth for a single mode of the comb spectrum. A photon coherence measurement determined a total spectral width of 275 GHz (FWHM). Single mode coincidences have been measured with the help of spectral filters. Idler photons at 1411 nm are filtered using two cascaded fiber Bragg gratings (FBG, from AOS) with a transmission window of 1.56 GHz with 20% efficiency while 854 nm photons are filtered using the Fabry-Perot filtering cavities described earlier in this thesis (sec.I.3) and which mimic the $D_{5/2} \rightarrow P_{3/2}$ transition in $^{40}Ca^{+}$ ion, serving as first compatibility test for further experiments with the ion. Resulting histogram is displayed in Fig IV.2.

IV.2. OPO-ion experiments

For the photon-ion interaction experiment, OPO and ion trapping setups are connected as shown in Fig. IV.3. A 90 meters fiber channel connects source and ion laboratories which is used to transmit OPO 854 nm photons. At the ion laboratory a 50/50 beam splitter is used: while half of the OPO photons are sent onto the ion for absorption, the other half is sent to the filtering cavities. As the ion works as a filter itself, filtering cavities are not used for selection of resonant modes, but used as a stabilization reference for the central OPO wavelength. Detection rate behind the cavities is used to generate an error signal for side-of-fringe locking of the piezo position of the OPO cavity.

Apart from the stabilization method employed, the experimental sequence, setup and geometry at the ion is similar to the frequency converter interaction experiment from section III.3, detecting quantum jumps at the ion induced by the absorption of photons in the $D_{5/2} \rightarrow P_{3/2}$ transition in the single trapped $^{40}Ca^{+}$ ion (see Fig. III.12). Selected photons from the OPO source have instead a 7 Mhz bandwidth and are produced at a much higher rate, as discussed further. For this reason the absorption time window at the ion is reduced to 7 ms meaning the experimental sequence runs at 140 Hz.

The result of this measurement is presented in Fig. IV.4. A coincidence peak is observed at zero time delay that marks the telecom heralded absorption of a single OPO photon. Ion resonant photons from the OPO were sent onto the ion at a rate of $\sim 340\,000$ and finally $2.06{\cdot}10^{6}$ quantum jumps were detected at the ion in the 310 minutes of measurement time. A signal-to-noise ratio of 6.7 was found for the histogram, with 12910 coincidences in the central bin over an average background of $3.65{\cdot}10^{6}$ counts per 13 µs bins. An estimation of the rate of resonant pairs generated

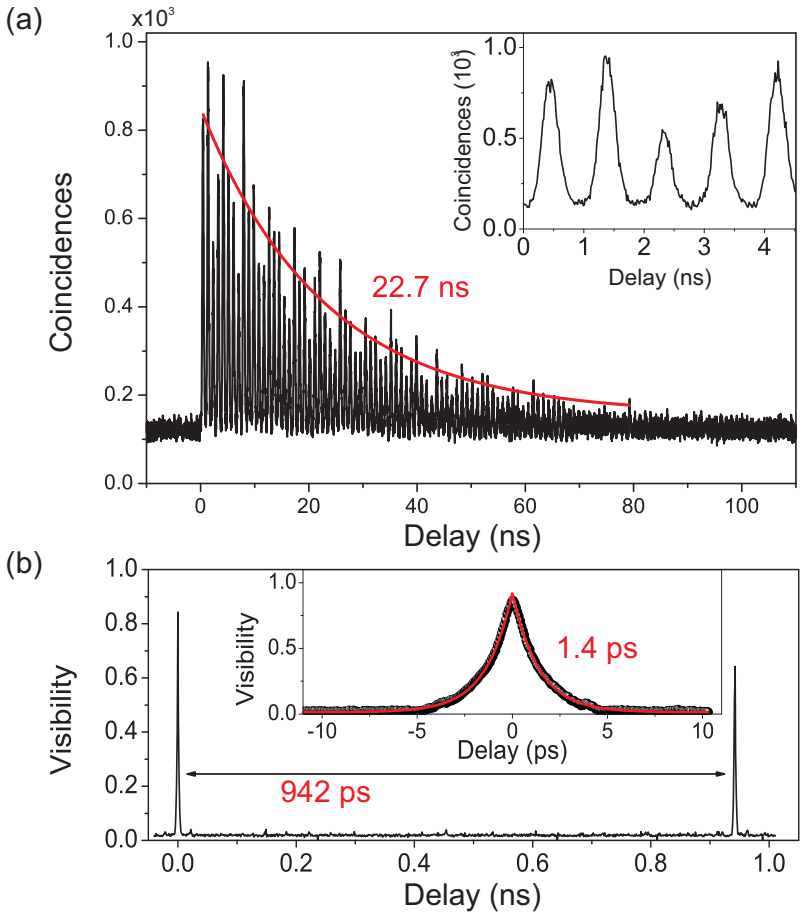

Figure IV.1: Mesured temporal characteristics of the OPO source. (a) Time correlation between signal (854 nm) and idler (1411 nm) photons by coincident detection. Short oscillations (~1 ns, inset) correspond to cavity round trip modulated by a 22.7 ns ring-down time. (b) First-coherence function of the signal photons. The inset shows a higher-resolution capture for a coherence time of 1.4 ps

at the OPO is back-calculated from the maximum absorption rate and the known losses of our setup, with which we estimate at least $2.5 \cdot 10^6$ s^{-1}. A comparison and analysis of figures of merit including previous experiments is performed in the following section.

Finally, as test of the control of the interface, a single-photon spectroscopy experiment was performed. Resonant OPO photons are sent onto the ion and effective lifetime decay change of the $D_{5/2}$ state is measured as a function of the photon detuning. As the photon absorption rate changes for off-resonant conditions, the spectral line can thus be probed. Photon detuning was controlled by changing the central frequency of the filtering cavities to which the OPO is locked via side-of-fringe-locking. The ion is prepared as for the earlier experiment and quantum jumps are detected. The effective lifetime τ_{eff} is calculated from the time distribution of quantum jumps, which represents the probability of decaying into $S_{1/2}$ after the preparation of $D_{5/2}$, as shown in Fig. IV.5, which increases as the photons get into resonance. Finally the photon absorption rate is

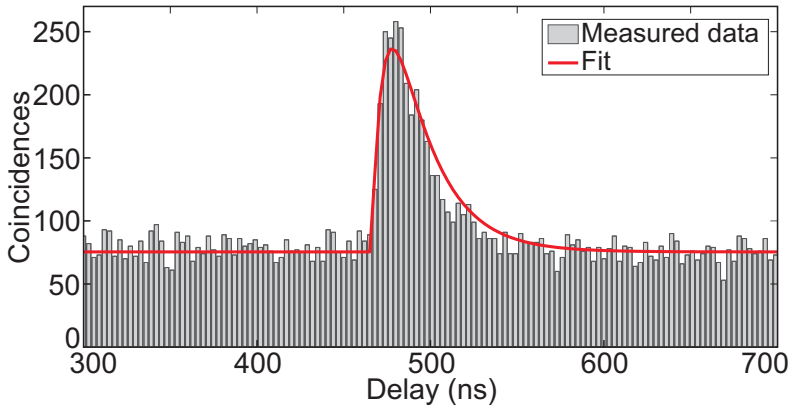

Figure IV.2: Time correlation between filtered signal (854 nm) and idler (1411 nm) photons by coincident detection. Slope on the left side represents the 7 ns ring-down time of the 854 nm cavities while the slope on the right side is given by the respective 22.7 ns of the OPO cavity.

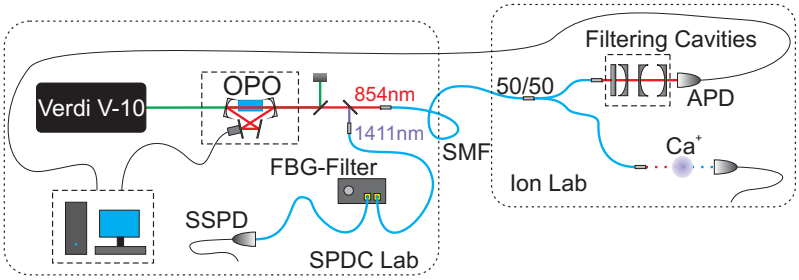

Figure IV.3: Experimental setup for the OPO-ion interaction experiment. OPO source generates photons at 854 nm and 1411 nm. Photons are split with a PBS, fiber coupled and sent onto the ion setup and heralding detection, respectively. Filtering cavities aree used at the ion lab for stabilizing the OPO emission. Absorption induced quantum jumps at the ion and telecom SSPD detections are detected and further correlated.

calculated as a function of the effective lifetime as

$$R_{abs} = \frac{1}{0.94}(\tau_{\text{eff}}^{-1} - \tau_{\text{sp}}^{-1}) \tag{IV.1}$$

this way correcting the spontaneous decay probability τ_{sp} and non-fluorescent absorption events. The detuned photon absorption recreates successfully the ion spectral line, as shown in Fig. IV.6.

IV.3. OPO vs SPDC-QFC

In the following we look at the numbers and compare the OPO performance with the results presented for photon-ion interaction using frequency conversion.

As expected from its configuration, the OPO source exhibits much higher generation rates than the SPDC bulk source. Our bulk source generates about 6000 narrow-band pairs per second, compared to $2.5{\cdot}10^6$ from the OPO source. Additionally, for single-ion interaction our bulk source

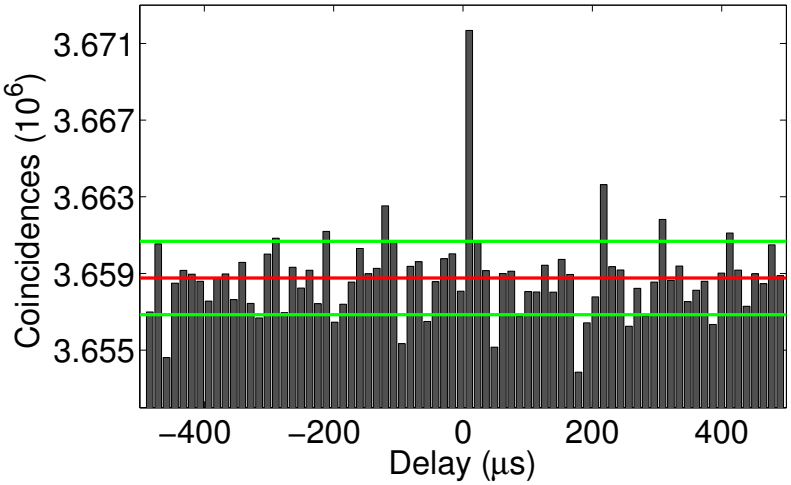

Figure IV.4: Coincidences between quantum jumps at the ion and heralding telecom photons. Central peak marks the telecom heralded absorption of OPO photons. Red line shows the average background per bin for a binning of 13 μs, in 310 minutes of measurement time. Green lines show the standard deviation interval.

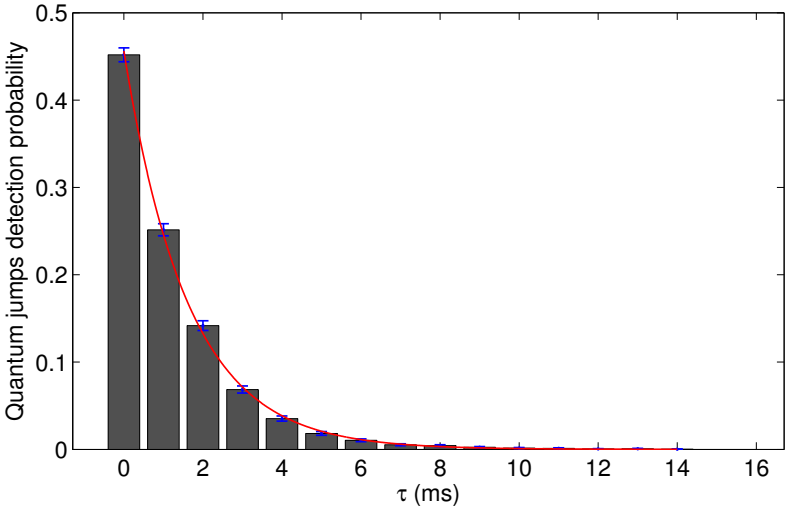

Figure IV.5: Quantum jumps time-distribution histogram for 20 MHz OPO detuning. Bayesian estimation of the probability is used and an exponential fit (red) is used [104]. An effective lifetime $\tau_{\text{eff}} = 0.0017(3)$ s is found.

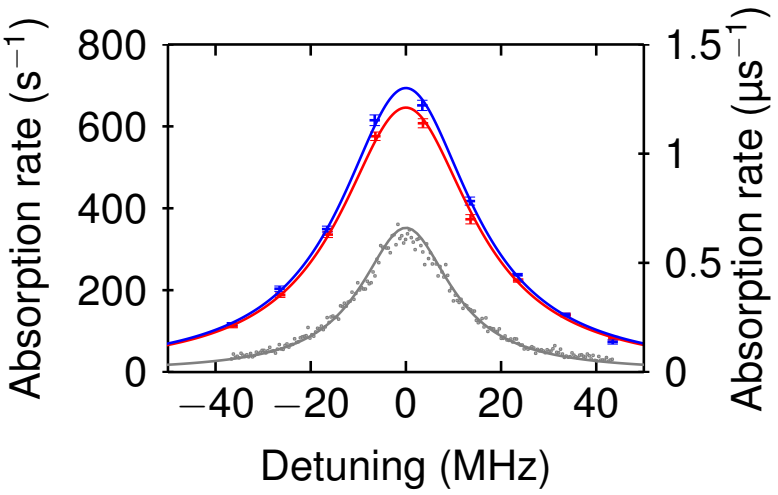

Figure IV.6: Single-photon spectroscopy of the $D_{5/2} \rightarrow P_{3/2}$ transition in $^{40}Ca^{+}$ ion. Blue and red solid lines (left axis) represent experimental runs and are obtained by detuning of the photon emission. Gray line represents laser spectroscopy for comparison (right axis).

requires the use of filtering cavities for reducing the broadband SPDC background, meaning its effective rate is reduced to $\sim$1500 s^{-1} non-coupled pairs. The OPO source also requires herald filtering, which is achieved by using FBG, decreasing the pair rate down in 20%, ($\sim 2.0 \cdot 10^6$) which still supersedes other state-of-the-art OPO sources [105, 106]. As mentioned in the interaction part, the OPO requires additionally wavelength stabilization which for the bulk source is already implemented. For the OPO this was achieved by using 50% of the photons, although only <1% of the coupled photons are needed for this purpose, which is easily achieved with a non-symmetric beam splitter.

Still, an important advantage of the OPO source is that heralds the signal 854 nm photon directly at a telecom wavelength, meaning no additional losses are necessary with this purpose. Our Bulk source rates are further reduced for telecom heralding. Under the experimental conditions presented in the last chapter, the efficiency at the converter side is $\eta_{\text{conv}} = 63\% \cdot 8\% = 5\%$ including fiber coupling, transmission, conversion efficiency and background reduction. This is the efficiency cost of making our source an hybrid telecom heralded source. Finally, considering filtering efficiency and fiber coupling, our hybrid source produces $\sim$ 70 s^{-1} fiber-coupled narrowband telecom-heralded resonant photons. Under the same conditions as in the interaction experiment, the OPO provides 11 000 s^{-1} pairs of such photons (without considering additional losses produced at the ion side). Further differences are seen in the context of the photon-ion interaction. At the ion a much higher absorption rate has been observed for the OPO source. By looking at the effective lifetime of $D_{5/2}$ a maximum absorption rate of 680 s^{-1} was observed compared to 12.5 s^{-1} maximum for the bulk source. Another interesting figure of merit of the interface is the absorption probability per telecom heralding detection (eq. II.3), which for OPO is $P_{\text{OPO}} = 6.6 \cdot 10^{-6}$ while for the combined ion-converter experiment is $P_{\text{conv}} = 4.1 \cdot 10^{-6}$. Although the brightness of the OPO is much higher, heralding probability is reduced by the big number of residual telecom partners of non-resonant photons due to the still broadband filtering of the FBG (1.56 GHz) compared to

the 7 MHz modes. This problem would be solved by a better filtering system. On the other hand converted photons case is affected by the background at the converter, which is high in comparison to the real heralds rate (>20 times). As discussed in the previous chapter, this would be also solved by better filtering after the conversion step. Furthermore, when measuring single-photon heralds, one could use the discrimination method presented in sec. II.4. As discussed early in this thesis, a key resource for the implementation of a quantum network with photon pairs is the generation of entanglement [12, 9]. For our bulk source high-quality polarization entanglement has been demonstrated (sec. I.3), with a fidelity of 97% for the maximally entangled singlet state $|\Psi^-\rangle$. This polarization entanglement, permitted by type II phase-matching conditions, has been used for instance to show polarization selection at single photon-absorption by the ion [21]. As seen in previous chapters, different protocols for photon-to-atom information can be implemented using polarization entanglement and a calcium ion [54, 30]. Moreover, 854 nm entangled photons pairs permit addressing two ions simultaneous for performing a Bell measurement, as shown in the proposal by Sangouard [68]. In this context a big disadvantage of the current OPO setup is that no polarization entanglement can be generated, which limits further implementations with the calcium ion. An alternative for entanglement distribution with the OPO source is the use of Energy-time entanglement (see sec. III.2.2). Energy-time entanglement has been already demonstrated for the OPO photons, with a Franson visibility of 73.3 ± 1.2%. Details are found in [94], although for this source a different memory should be used (temporal mode storage) for instance using Cesium atoms [107, 108], for whose wavelengths the OPO is easily adjusted. Nevertheless, even though polarization entanglement of the photon pairs generated by our bulk source is a very useful tool, it is still limited by the frequency conversion. Frequency conversion process implemented requires a defined input photon polarization. By defining the polarization axis we project out polarization entanglement with the partner particle. For overcoming this problem polarization insensitive conversion or entanglement-conversion strategies have to be implemented [86, 109].

Finally, we see that OPO source supersedes importantly the performance of our bulk source. The SPDC-QFC interface is mainly limited by the low brightness of the SPDC source more than the quantum-frequency conversion. As discussed in for the doubly-heralded interaction (II.6), an increment in a factor 100 could increase importantly the possibilities of this interface by implementing an enhancement cavity. Background reduction can be achieved for both setups by using better filtering devices, e.g. state-of-the-art fiber-bragg gratings. Quantum frequency conversion can also be improved by better pump-coupling lenses, given that enough pump power is available.

The OPO source is a powerful tool for an atom-photon interface: high-brightness, narrowband emission and telecom heralding make it a very attractive option for the connecting nodes of a quantum network. However, entanglement perspectives have to be taken into account and selected according to the desired target memories. On the other hand frequency conversion is a versatile tool since its use is not only limited to a particular quantum system, allowing one to connect any kind of quantum system keeping the necessary non-classical properties for the implementation of a quantum network. Polarization-independant conversion and conversion of ion photons are to be explored.

Chapter V

Conclusions and outlook

In this chapter we review and conclude the presented work, which has covered a number of photonic interfacing experiments involving SPDC photons, quantum frequency conversion and a single trapped ion. Before the final remarks and outlook, we discuss the ion's photon absorption efficiency for the different interaction experiments presented in this thesis.

V.1. Photon absorption efficiency

The probability of a photon absorption by the ion for a given experiment is ruled by the photon rate impinging on the ion R^*_{ph}, the size of the absorption window Δt_{abs} and finally the absorption efficiency.

$$P_{\text{abs}} = 1 - exp(-\eta_{\text{abs}} R^*_{ph} \Delta t_{\text{abs}}) \tag{V.1}$$

The absorption efficiency η_{abs} depends on the overlap between the impinging photon mode and the spatial pattern of the ion's dipolar absorption. In our experiments the photon spectral shape has been adjusted to match the target transition in the calcium ion, and its spatial shape is adjusted with collimation optics and ultimately by the HALO lens. The ion profile depends on its temperature (spatial extension) and also on the spatial-spectral properties. For the particular $D_{5/2} \rightarrow P_{3/2}$ transition, the absorption probability between Zeeman substates is given by the selection rules and the respective Clebsch-Gordan coefficients as shown in Fig. V.1. The maximum is given for σ polarized photons along the quantization axis ($\Delta m = \pm 1$) for the outermost Zeeman sub-levels $\{-\frac{5}{2}, -\frac{3}{2}\}$ and $\{+\frac{5}{2}, +\frac{3}{2}\}$ transitions.

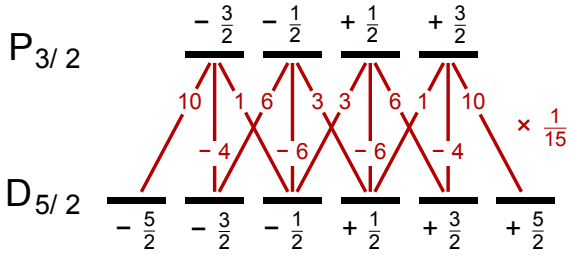

Figure V.1: Clebsch-Gordan coefficients of the $D_{5/2} \rightarrow P_{3/2}$ transitions at 854 nm.

For our experiments, we target the best possible conditions for absorption. To achieve this we chose the transition $\{-\frac{5}{2}, -\frac{3}{2}\}$, meaning we have to prepare the ion in $\left|m = -\frac{5}{2}\right\rangle$ and adjust the photon polarization to σ^+, sending the photon through one HALO along the quantization axis. As

discussed in [27], the maximum absorption efficiency under this conditions is given by the overlap between the HALO and the dipole emission pattern in one direction for σ polarized photons (6%), the oscillator strength (5.87%) and the squared Clebsch-Gordan coefficient (10/15).

$$\eta_{\text{M.abs}} = 6\% \cdot 5.87\% \cdot \frac{10}{15} = 2.35 \cdot 10^{-3} \tag{V.2}$$

In passed experiments [19, 21, 25] an important drawback was related to the fact that the $D_{5/2}$ could not be prepared coherently, but using inhomogeneous decay from $P_{3/2}$ after a three-photon absorption. This necessary involves transitions from $S_{1/2}$ to $P_{1/2}$, $P_{1/2}$ to $D_{3/2}$ and finally from $D_{3/2}$ to $P_{3/2}$ that are coupled by laser light. Avoiding to populate the intermediate states is desired because their branching rates to other levels decrease the probability of exciting the ion to $P_{3/2}$. From the $P_{3/2}$ state, one had to wait for inhomogeneous decay to $D_{3/2}$. This process turns to be rather inefficient, given that the branching ratio of the $P_{3/2}$ state for decaying back to $S_{1/2}$ instead is 16 to 1, i.e. 0.934 for $P_{5/2} \rightarrow S_{1/2}$ compared to 0.0587 for $P_{3/2} \rightarrow D_{5/2}$. Additionally, as the decay from $P_{3/2}$ into $D_{5/2}$ is inhomogeneous, the population is distributed among its different Zeeman substates and therefore a further optical pumping step was needed to prepare the ion into the outermost states, which cannot be achieved with 100% probability. These facts are more extensively discussed in [27], where optimization of polarization, detuning and power of the three coupling lasers for the three photon absorption process has been performed for using the ion as a versatile single photon generation at 393 nm and networking experiments between two $^{40}Ca^{+}$ ions in separated traps [24, 25]. As we now count with a 729 nm, direct coherent preparation into $\left|m = -\frac{5}{2}\right\rangle$ with <99% measured probability, which plays an important role in the ion excitation as we will see from the numbers. For the previous experiments an absorption efficiency of $\sim 5 \cdot 10^{-4}$ was observed (also called absorption probability per photon). We further compare with the result presented in this thesis.

Doubly-heralded absorption

For the doubly-heralded absorption, we calculate the absorption efficiency using the information extracted from the measured coincidences and the characterization parameters presented in chapter II. Using only information of single heralds channel detections is not robust enough since the heralds are strongly screened by dark count detections. Using the total number of coincidences C_T, the interaction time T_{int}, photon generation rate R_{ph}, and known losses (η_{coll} collection efficiency, η_{coup} fiber coupling, η_{fil} filtering cavities, η_{ov} spectral overlap), using II.1 we obtain:

$$\eta_{\text{abs}} = \frac{C_T}{\eta_{coll} \cdot \eta_{coup} \cdot \eta_{fil} \cdot \eta_{ov} \cdot R_{ph} \cdot T_{int}} = 1.1 \cdot 10^{-3} \tag{V.3}$$

This in an average value over the total experimental run, although as commented in the doubly-heralded absorption chapter and observed in II.6, the average calculated number is below the maximum rate (including standard deviation), which leads to an sub-estimation of the absorption efficiency.

Interaction using frequency conversion

For this experiment we use a different approach and we look at the quantum jumps probability into $S_{1/2}$ during the experiment. As shown in III.4, quantum jumps probability during the absorption window is 44.59%, which leads to an absorption rate of 12.5 abs/s. The absorption rate is also calculated from the histogram of Fig. III.14(a), $\frac{1}{0.0855} - \frac{1}{\tau_{sp}} = 10.9$ abs/s. Considering the branching ratio of the $P_{3/2} \rightarrow S_{1/2}$ (93.5%), we obtain absorption rates of 13.36 abs/s and 11.6 abs/s, respectively. Furthermore, the absorption efficiency is given by

$$\eta_{\text{abs}} = \frac{R_{abs}}{R^*_{ph}} \tag{V.4}$$

the ratio between the absorptions rate R_{abs} and the rate of resonant photons impinging on the ion, R^*_{ph}. From the broadband spectral region of photons produced by SPDC, the resonant photon rate is calculated by a characterization measurement that weights the amount of photons within the spectral region of interest by looking at the coincidences with filtered photons. For this particular experiment, $R^*_{ph} \sim 4000$ resonant photons per second. Considering the interaction time (chopper-free, 85%), this leads to $\eta_{\text{abs},1} \approx 2.9 \cdot 10^{-3}$ and $\eta_{\text{abs},2} \approx 2.5 \cdot 10^{-3}$, for the quantum jumps probability and the effective lifetime values, respectively. Absorption efficiency calculated here and in the previous section are for the same 854 nm photons from the bulk SPDC source. As it seen, the latest values are higher than the previously reported and reach the range of the theoretical maximum (they even exceed this value but uncertainty is not determined).

OPO source-ion

For the OPO source-ion experiment, the absorption efficiency is based on the maximum oberved absorption rate. From quantum jumps detection this value corresponds to 680 abs./s. The estimated number of resonant OPO-photons at the ion (weighted within 22 MHz) is 340 000 s^{-1}, which leads to an absorption efficiency of $\approx 2.0 \cdot 10^{-3}$. For this experiment the same transition and geometrical conditions for the photons were used as for the frequency conversion case, however, the resonant OPO photons have a narrower spectral bandwidth of 7 MHz.

Finally, after analyzing the absorption efficiency for three different experiments we observe a higher value compared to previous experiments. This fact is attributed to a better preparation in $D_{5/2}$ using a 729 nm narrow-band laser, since other conditions as focusing and type of photons have been kept the same. From the values obtained it is seen that we come close to the calculated maximum, being $\sim 2 \cdot 10^{-3}$ a reasonable assumption for the absorption efficiency for 854 nm single photons under the current conditions.

V.2. Conclusions and outlook

During this thesis a series of interface experiments in the context of quantum networks have been carried out. These experiments have explored photonic and atomic interfaces which are the basic building blocks of a vision of a quantum communication network based on single-trapped ions as nodes for storing and processing information, and ion and SPDC generated single photons as information carriers and channels connecting the nodes of the network. Moreover, we have shown that using quantum frequency conversion and photon emission in the telecommunications band the transmission capabilities of our interfaces are widened.

In more detail, the results achieved during this thesis are the following: We have shown the doubly heralded absorption of an SPDC photon by a single ion. A SPDC single photon heralds the presence of its partner photon which is sent for absorption by a single ion while a successful absorption event is heralded by a Raman-scattered single photon without altering the final state of the ion. The time correlations between heralds showed an analog 7 ns photon structure for triggering and absorption emitted heralds. A doubly-heralded coincidence rate of $3.6 \cdot 10^{-3} s^{-1}$ has been detected. Furthermore, a powerful general method for background reduction in the heralding process has been proposed and successfully implemented, showing a suppression of the background counts of 16 times for the presented results.

Quantum frequency conversion has been used in a hybrid SPDC+QFC interface. With an 8% overall efficiency, it has shown preservation of time-correlations of broad and narrowband photons and also energy-time entanglement that violates the Bell inequality by 1.6 standard deviations. Heralded single-photon characteristics for different cases and multiplexing of classical and quantum signals has also been demonstrated. Anti-bunching in $g^2(0)$ of 0.0074 ± 0.0037 and 0.19 ± 0.14 have been found for converted broad and narrowband photons, respectively. Furthermore, this interface has been connected to the ion trapping apparatus to show that heralding of an SPDC photon absorption in the telecom band is possible while the absorption is detected via quantum jumps. A rate of $1.9 \cdot 10^{-2} s^{-1}$ of these coincidences has been measured. This way, we completed a set of measurements to propose the use of these tools for a single-photon–single-ion quantum network.

Interaction of OPO generated photons with a single trapped ion was demonstrated, showing that direct heralding at telecom with high absorption rates is possible. A coincidence rate of $1.9 \cdot 10^{-2} s^{-1}$ was measured, with a maximum absorption rate of 680 s^{-1}, the highest reported to date. As a signature of control over the system, a single-photon spectroscopy of the ionic transition has been presented. Wavelength flexibility of this source widens perspectives for compatibility with other types of memory-like systems.

The experiments described here are the result of the combined effort of several persons and different setups. My main contributions regarded operating the bulk SPDC source setup, which has been the central device of the experiments described in this thesis, both conceptually and practically. This task included helping to unmount the experiment at the Institute of Photonic Sciences (ICFO), Spain, and re-mounting it in Saarbrücken, Germany (2010). Further tasks included helping to setup the channels for the combined work with the laboratories of Prof. C. Becher and the coordination of the joint experiments. In our group, S. Kucera contributed specially to the experimental control and data analysis for the experiments with the ion. P. Eich and P. Müller

contributed at the ion side preparing the ion and kept it running for the interaction experiments. In the group of C. Becher most of contributions where coordinated by A. Lenhard, who implemented and operated the frequency conversion setup and with whom the QFC+SPDC experiments where designed and carried out. M. Bock took part by running the OPO source and developing the algorithm for triple-coincidences analysis. Combined experiments between both groups are part of a more general initiative focused in the development of quantum repeaters carried out by professors J. Eschner and C. Becher, at the Saarland University and who supervised the experiments.

Additionally during this thesis, the test of a waveguide photon source has been carried out. Characterization results show that due to broad-band multi-mode behavior this kind of generation enhancement techniques might not be appropriated for narrow-band photon generation purposes, although by dedicated tailored construction this option could still be considered. Finally a comparison of absorption efficiencies at the ion for 854 nm photons has been obtained from the interaction experiments. An absorption efficiency of $\sim 2 \cdot 10^{-3}$ has been observed, which corresponds to an increase of 4-fold respect to previous experiments, due to better ion state preparation for the absorption.

During this doctoral work and together with a set of complementary experiments performed in our group (M. Schug and C. Kurz, [27, 26]), we have shown important necessary steps for a feasible implementation of a long-distance compatible GHz repeater scheme based in the absorption of SPDC photons [12], Fig. V.2. Entangled photon pairs are generated by SPDC and while one of the photons is absorbed by the ion, as shown in the doubly heralded experiment, its heralding partner is sent into a distant point, aided with frequency conversion, for a projective Bell state measurement permitting to swap the entanglement with a distant node. The single blue herald emitted at the ion can be used for the same purpose, but also as indicator of a successful absorption for background reduction, which is protected from dark counts and preparation errors by the presented methods. Quantum frequency conversion has also shown to preserve fundamental properties of the SPDC emission as time correlations, energy-time entanglement and single-photon characteristics confirming that it can be used as a universal tool within the quantum-networks framework for connecting any type of quantum systems. Furthermore, by using a highly tunable OPO source heralding at telecom band is possible at high-rates, and its wavelength flexibility opens up new perspectives for hybrid repeater schemes, for instance, for connecting Cesium and Calcium memories. As an outlook, we comment some of the most important short-term limitations of these systems, in order to project their use for more advanced experiments. One of the main limitations of our setup is the photon rate generated by our bulk SPDC source ($\sim$ 6000 s^{-1} resonant pairs), given that the absorption efficiency of the ion for 854 nm photos under current conditions is low ($\sim 2 \cdot 10^{-3}$). Although stronger photon-atom coupling could be achieved by cavity enhancement at the ion, simplicity suggests to concentrate the experimental efforts in the enhancement of the photon generation rates. An increase in three orders of magnitude as for the OPO source would strongly enhance the interaction thus decreasing the long experimental runs needed for the experiments presented in this thesis ($\sim$ 10 days each), which due to set-up and human conditions were at the limit of our resources. Such an effort is already been pushed forward by a new generation of PhD students. With a high rate of entangled photon pairs (10^6), which might be reached by the implementation of new technologies, entanglement between two ions by swapping photonic entanglement, an old envisioned goal, could be achieved.

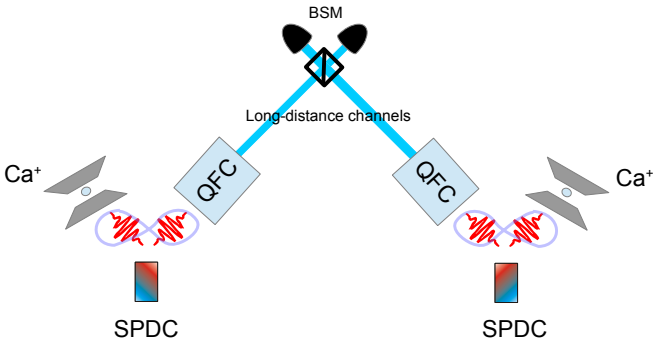

Figure V.2: An adapted network repeater as in [12]. Entanglement preserving frequency conversion allows for a Bell-State measurement and entanglement swapping to remote Calcium ions. One ion can be replaced by another Bell-state measurement between two SPDC photons generated remotely for enhancing long distance communication (quantum relay) [100]. Also, direct entanglement between two ions by entangled-photons absorption is possible. [68].

At the converter setup the main limitation is conversion efficiency due to coupling of the pump beam (38%). This is solved by using better low-absorption optics whose implementation is also going through. This way, conversion of ion-generated photons and the study of its properties is a direct application to be realized. An important pending step is the entanglement preserving conversion, without it, the implementation of a repeater scheme is not possible, meaning is an interesting topic where to focus efforts. For the same reason, using the OPO for interaction with different type of memories is recommendable for exploring hybrid schemes, which are also within the experimental plans for the future.

Appendix A

Waveguide-based photon source

In the present appendix details of a photon source project based on a PPKTP waveguide-crystal are presented. As discussed in chapters II,III and IV there are essential properties required for building an photon-atom interface using a SPDC source . This properties are brightness, narrow spectral bandwidth and high-quality entanglement generation. Although our current bulk source has been useful to show a series of interfacing experiments [19, 21, 69, 83], brightness of this source has shown to be a limit for further implementations, mainly due to reduced absorption efficiency of the ion in the target transition. Strategies for increasing the photon-atom coupling using cavities at the ion as in [62, 110, 99] could be also implemented, but represent an increased experimental effort. As discussed in sec. II.6, an alternative strategy is either the construction of an enhancement cavity or the use of state-of-the-art non-linear optics technology. In the course of the present work a source based on a waveguide non-linear crystal has been studied. As described below, high brightness has been observed for such devices, which made us consider this option for photon generation in our experiments. However, as described in this chapter, this effort has not achieved the expected results due to broad multi-mode spectral behavior of the device, discouraging its use for narrow-band photon generation purposes.

A.1. Overview

First reports of waveguide SPDC sources go back to early 2000s, where high rates of photons pairs have been reported for low pump powers (~μW). Using waveguides in non-linear crystals originally engineered for efficient second-harmonic-generation (SHG) showed that SPDC generation is also enhanced [111, 112, 113, 114]. Altogether with more advances in waveguide sources, in [115] Fiorentino and coworkers reported a 50 times enhancement compared to a bulk PPKTP source and presented a model that explains the enhancement effect.

As suggested in [115, 116], the enhancement effect of the waveguide is seen calculating the spectral brightness

$$\frac{dP_s}{d\lambda_s} = \frac{16\pi^3\hbar d_{\text{eff}}^2 L^2 c P_p}{\epsilon_0 n_s n_i n_p \lambda_s^4 \lambda_i} \frac{1}{A_{wg}} \text{sinc}^2(\Delta k_z L/2) \tag{A.1}$$

where d_{eff} is the effective nonlinear coefficient, L is the length of the crystal, P_p is the pump power, ϵ_0 the permitivity of vacuum, c the speed of light in vacuum , $n_{s,i,p}$ the refractive indices of the crystal for signal, idler and pump wavelengths, and λ_s the signal wavelengths. From the phase-matching conditions, $\Delta k_z = k_p - k_s - k_i - \frac{2\pi}{\Lambda} + \frac{k_{st}^2 + (k_{st}+k_{gt})^2}{k_s} 2$, where $k_{s,i,p}$ are the k vectors of signal, idler and pump and k_{st} and k_{gt} are the transversal components of the signal

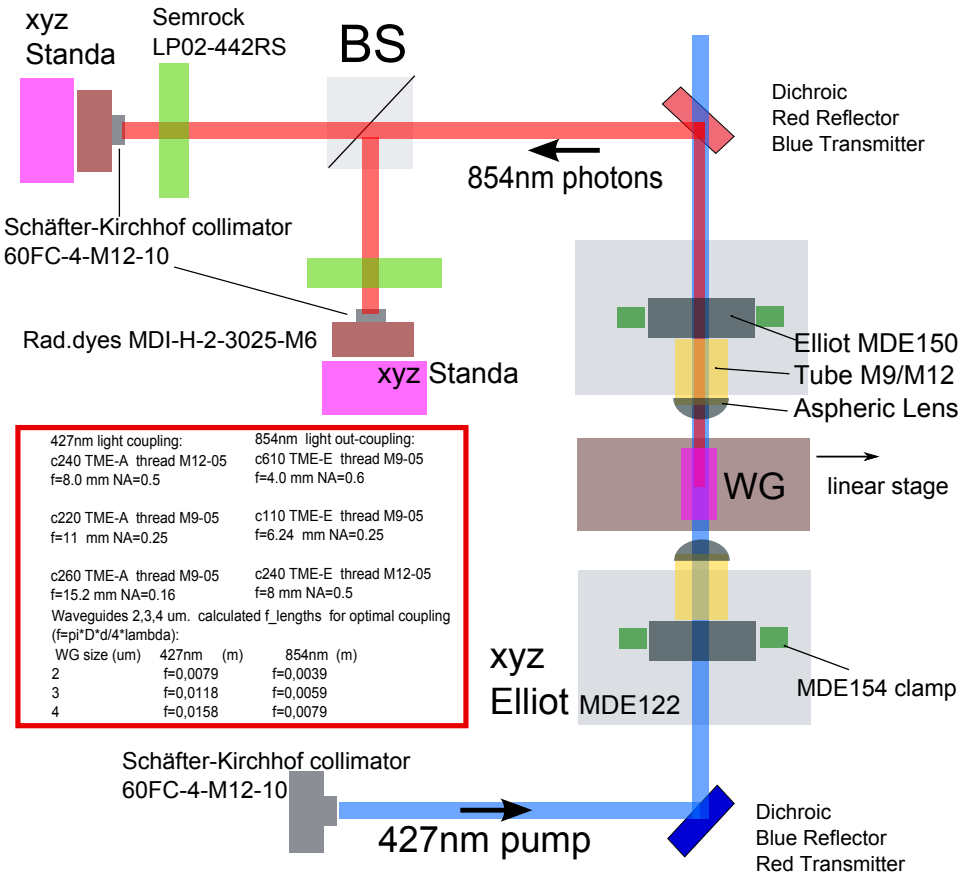

Figure A.1: Simple schematic of the WG set-up. See text for details

and grating wave vectors. The photon generation increase comes from A_{wg}, the cross-section of waveguide area which is reduced to the tight dimensions of the waveguide geometry (typically a few µm in every transversal direction). This implies an energy re-distribution that benefits the converted modes. Following these reports, a number of applications have been implemented for such devices, mostly for generation of photons in the telecom region. A good review that describes perspectives and interesting implementations of waveguide-based photon sources and integrated-photonic waveguides is presented in [117].

A.2. Design

The design of the implemented setup is based in a set of components typically used for precision fiber-coupling which in this case are used for coupling-collimating pump and generated modes in the waveguide. The waveguide is in many aspects similar to an optical fiber, which is also a waveguide with dimension in the micro-metric range and for which high numerical aperture objectives are employed.

A simple schematic of the waveguide setup is shown in figure A.1. Aspheric lenses (Thorlabs) are mounted on x-y-z submicro-metric precision translational stages (MDE122, Elliot-Martok) for

in- and out-coupling to the desired waveguide, matching the 4,5 and 6 μm guides Mode Field Diameter (as detailed in the table of the figure). The waveguide receptacle is fix to a stage with 4 degrees of freedom adjustment (lateral, vertical, inclination and rotation). Dichroic mirrors are used on both side for directing the beams and separating 427 nm from 854 nm light. The waveguide crystal is placed on a copper holder designed for our chip by AdvR. An NTC thermistor element (Redfish RNBR-103F) is attached to it and used for thermal stabilization with a temperature controller (ILX lightwave LDT-5412, ±0.01 C temperature stability). Photons are coupled into single-mode polarization maintaining fibers using fiber collimators (Schäfter-Kirchhof, 60FC-4-M12-10) mounted on custom-made holders (Radiant Dyes) over linear stages (Standa). Razor-edge filters are used for cutting off pump beam residuals (Semrock, LP02-442RS).

Waveguide chip

Our waveguide chip (ITI1102-A27) produced by Advr INC. (Montana, US) consists of a 25mm long periodically-poled KTP crystal with Rb^+ diffused waveguides. Construction of waveguides for non-linear crystal is mainly performed either via ion in-diffusion or by refractive index steps by carving techniques. A general insight into waveguide construction techniques, design and properties is found in [118]. Ours was manufactured following the first approach. A contact mask is used to pattern the crystal surface and furthermore a bath of $RbNO_3$ permits Rb^+ diffusion that replaces K^+ ions, forming and index step relative to the surrounding wafer, which in our case corresponds to 0.01.

Phase-matching conditions were chosen for type-II degenerated SPDC emission at 854 nm (427 nm pump). A periodic poling of 10.780 μm was used for functioning close to room temperature (23 degrees C) and anti-reflection coating was applied for pump (427 nm, R<0.3%) and photons (854 nm, R<0.2%) wavelength on the input facet and only for photons on the output facet. In the waveguide chip, 24 waveguides are distributed in 4 groups, with repeated 4, 5 and 6 μm width and 8 μm height distributed over the 1.5 mm total width of the waveguide as shown in A.2. Refractive index of the KTP wafer is 1.83, which with the index refractive step of the waveguide produces a N.A. of ∼0.2 (depends on the particular waveguide).

A.3. Characterization

At first, a characterization of the efficiency and functioning of the waveguide is performed using second-harmonic generation by coupling 854 nm laser light in the reverse direction of the SPDC for creating 427 nm light. Due to direct wavelength relation between SHG and SPDC, an overview of the functioning of the waveguide and efficiency for the interesting wavelengths can be done this way [119, 120]. Looking at the waveguide modes at SHG turns to be a very important indicator of the accepted spatial modes of the waveguide and is used to characterize them. In figure A.3, the wavelength profile of SHG is observed. A sinc^2 function is expected for a single-mode but the irregular shape observed is an indication of imperfections of the waveguide and the survival of simultaneous modes. This fact has been described in [121], and is attributed to non-uniformity of the periodic grating structure and that becomes more probable as the length of the non-linear crystal increases. We also observe this behavior when characterizing the SHG process as a function of the

Waveguide spacing (AdvR)

NOV11 Basic layout. Layout of a full chip width.

Key features:

Guide	WG Width (µm)	WG Spacing Center to Center (µm)	Comments
1.1	2	35	
1.2	3	35	
1.3	4	35	
1.4	2	35	
1.5	3	35	
1.6	4	75	
Planar	100	75	
2.1	2	35	
2.2	3	35	
2.3	4	35	
2.4	2	35	
2.5	3	35	
2.6	4	75	
3.1	2	35	
3.2	3	35	
3.3	4	35	
3.4	2	35	
3.5	3	35	
3.6	4	75	
4.1	2	35	
Groups 4, 5, 6 are identical to Group 3 with same spacings			
6.6	4	360	Standalone Guide, <180um to edge of chip

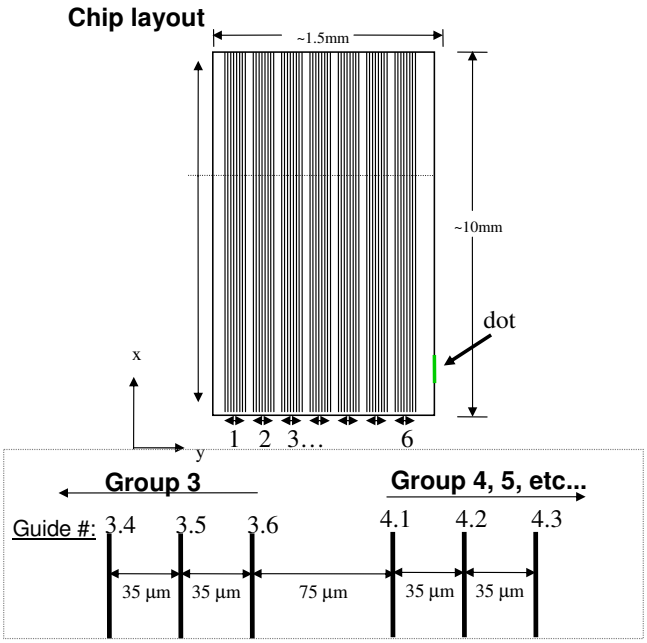

Figure A.2: Manufacture indications for the distribution of waveguides in the crystal with their respective width. Advr specifications sheet.

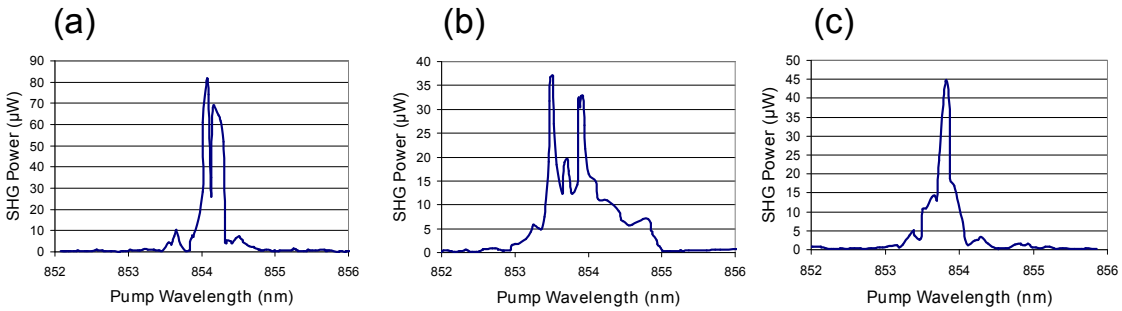

Figure A.3: Characterization of waveguides for SHG (AdvR). (a) Guide 5.1, 25 deg. C, 24 mw pump power. (b) Guide 3.1, 25 deg. C, 7 mW pump power. (c) Guide 4.4, 23 deg. C, 21 mW pump power.

crystal temperature as seen in Fig A.4 for waveguide 2.4, similarly for the rest of the waveguides of the chip. A direct relation between these profiles is expected, as there is a linear dependence between λ and T [122]. At first we attributed these effects to remaining photons of a broadband SPDC emission (a few nm), although as we will see later this is related not to a single broad band mode but multi-mode characteristics of the waveguide emission. Further analysis is done by looking at the spatial modes of the waveguide. This is done by using the waveguide out-coupling lens for imaging the output mode into a CCD camera.

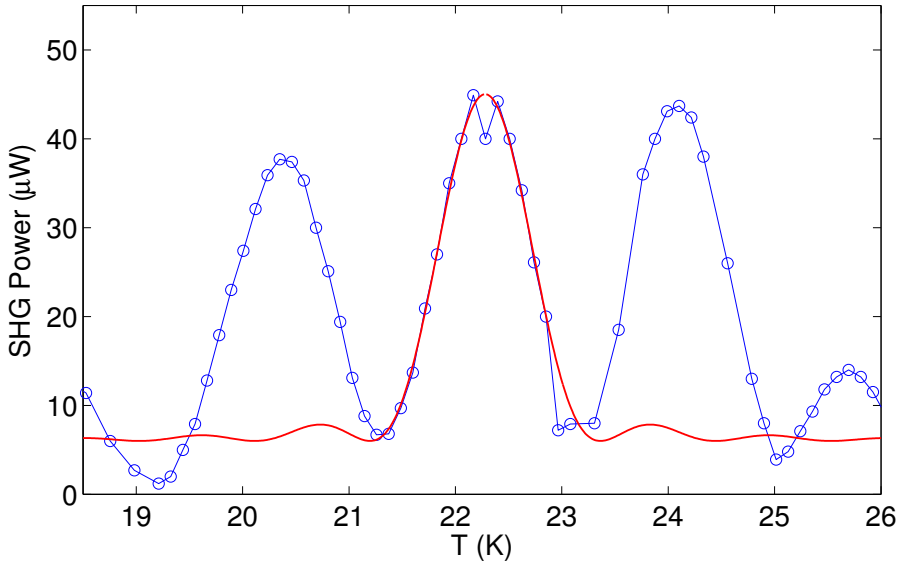

Figure A.4: SHG power as function of the crystal temperature. Blue data points represent detected power at 427 nm. The blue solid line is a guide for the eye. Solid red line represents a sinc^2 function of 0.967 K width. An 854 nm pump power of 6.5 mW is used with transmission of 43%.

In Fig. A.5 spatial modes for the pump and generated photons (427 nm above, 854 nm below) are shown for the waveguides of figure A.3. Our observations confirm the results presented in [121], where spectral filtering is used for selecting desired modes only. We have used razor-edge filters for cutting off remaining pump light which also cuts off some far resonant modes, nevertheless there is still a considerable contribution arriving at the detectors stemming from broadband emission. Unfortunately there are no commercially available band-pass filters that match the SPDC photons at 854 nm within a reasonable window. Filtering cavities can be applied in one arm for spectral selection, but extremely high photon rates at the partner arm saturate detection thus avoiding to reach coincidence rates that outperform the bulk source performance. Photon coincidences reach a maximum of ~18 000 per second for ~2 mW pump power for the full SPDC bandwidth using the waveguide 4.4 which has been indicated by the manufacturer as the one fulfilling the requirements. In order to determine effectively the spectral properties and thus know if within the region of interest (22 Mhz) generation rates can be improved, SPDC spectra are recorded using a spectrometer (Princeton Instruments, AG Becher). Several waveguides are analyzed, an example is shown in figure A.6. This measurement confirms that several modes of the waveguide are excited simultaneously associated to different spectral modes. This phenomenon has been explained in [120, 123], which includes a full characterization of the photon generation in the different modes by using sum frequency generation (up-conversion). This description explains the parity correspondence between spectral and spatial modes observed in the waveguide and moreover, since there is a multiple mode-correlation from the pump mode for their generation, explains how the waveguide can be used for the creating frequency hyper-entangled photon states.

In our case, best conditions from SHG characterization were expected for waveguide 4.4.

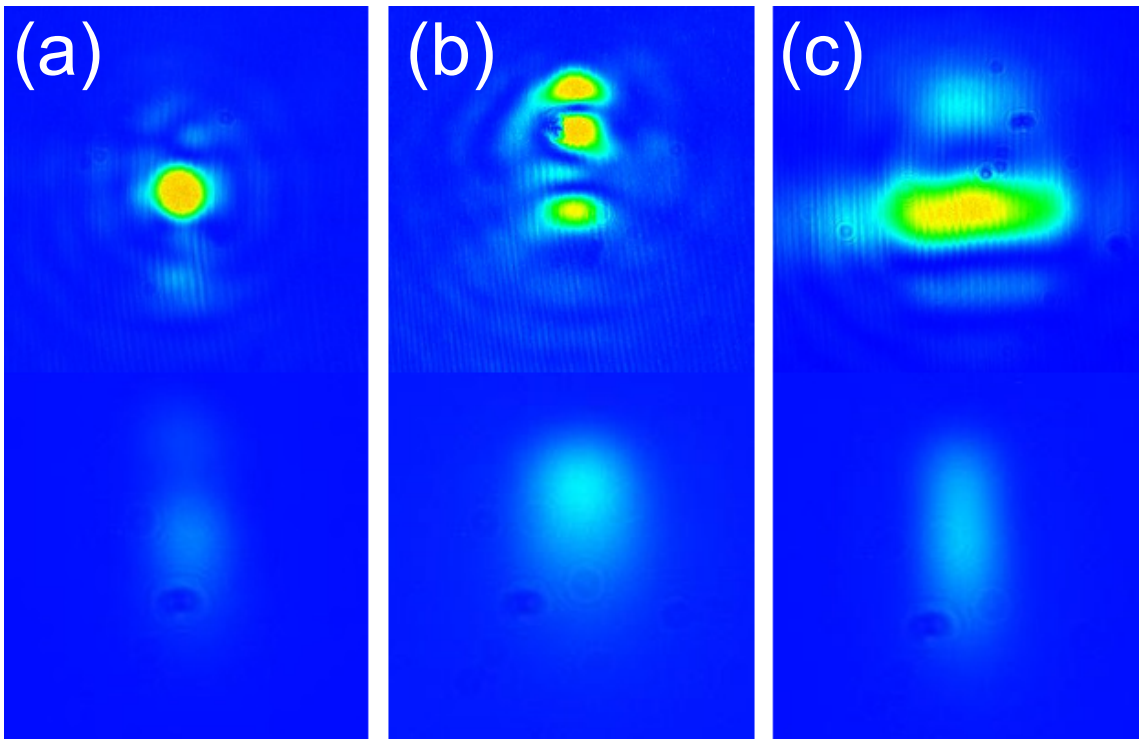

Figure A.5: Spatial modes of coupled waveguide for waveguides: (a) 5.1, (b) 3.1 and (c) 4.4 (see Fig. A.3). Above: transmitted 427 nm pump modes. Below: 854 photons modes.

meaning most of the energy concentrated in the central mode at 854 nm as seen in A.3 but by looking at its SPDC spectrum the irregular broadband emission makes the selection of a single mode at our desired wavelength insufficient. Waveguide 3.1 possesses a mode at the desired wavelength although for waveguides of this size (4μm) the coupling efficiency for a particular pump mode is greatly reduced (<5%), producing very low generation rates (see (b) in Fig.A.5). Anomalies of waveguide 4.4 are attributed by AdvR to an irregularity in the waveguide or damage due to exposure to high-temperature, which might be a consequence of the coating process.

Furthermore, a second uncoated chip (BCT1104-A35) which is originally a failed test for the construction of the initial one was delivered by the manufacturer. This chip should not display the problems of the previously described. As before SHG power as a function of the wavelength, spatial characterization and SPDC spectrum are analyzed for the best waveguide of the chip (5.1) as seen in figures A.7 and A.8. Although multi-mode behavior is observed, conditions for working at 854 nm at the expected temperature are better than the original chip, unfortunately, still most of the spectral power is distributed among other modes outside the region of interest.

For this waveguide a maximum of $\sim$ 16 000 coinc. per second is observed (broadband) with a pump power of 1.5 mW. Since this waveguide is small (4μm) and we have no anti-reflective coating, a maximum of 4% coupling efficiency is reached, with an efficiency per detection arm of $\eta_{1,2} \approx 0.008$, meaning efficiency for common modes in both arms is extremely low. This is to be expected since signal-idler modes are spectrally distributed on opposite sides of the central wavelength, for which our collection optics design is not appropriate. As an important number of

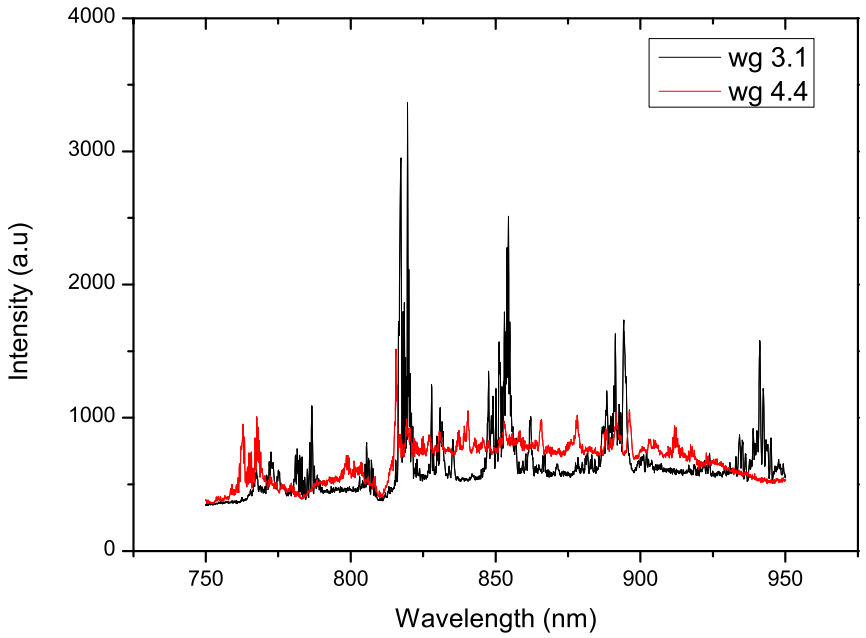

Figure A.6: Spectra of emitted SPDC photons of waveguides 3.1 and 4.4 for T=22.5 C. Several peaks are resolved, corresponding to different spatial modes of the waveguide.

photons belonging to other modes are still detected at the APDs, saturation is reached quickly and no higher coincidence rates are observed. Moreover, we use the high-resolution spectrum of fig. A.8 (red solid line) for looking at the spectral region of interest and making a rough estimation of pair production and spectral brightness. For the central peak at 854 nm we fit a sinc function from which we obtain a width of 0.59 nm, corresponding to an spectral bandwidth of 243 GHz. As shown in figure A.9, the 22 Mhz region (solid magenta) represents $9.4 \cdot 10^{-5}$ of the broadband emission in the selected bandwidth (red solid line). For comparison, 854 nm bulk source measured emission spectrum is plotted in blue line. Furthermore, we use as a reference the detection rates mentioned earlier and scale proportionally. Coarsely, we attribute the maximum coincidences to the central region, which gives us an upper boundary for the brightness. This way, for the 22 Mhz region the amount of detected coincidences is $\sim 1.5\ s^{-1}$.

In order to compare photon generation rates with our bulk source one should take into account the filtering steps needed, which for our filtering cavities reduces counts in 70%, meaning finally 0.45 counts would be detected. This is lower than the rate we observe for the bulk source at maximum power. Nevertheless, the signal channel would be still saturated by photons of other modes. Using a FBG or a monolithic filter [124], this broadband background could be reduced at a low cost of about 80% transmission. Under these conditions a comparison with the bulk source seems unfavorable, however one has to still take into account the spectral brightness. These rate is calculated for a low pump power of 1.5 mW since higher powers saturate the detectors, however

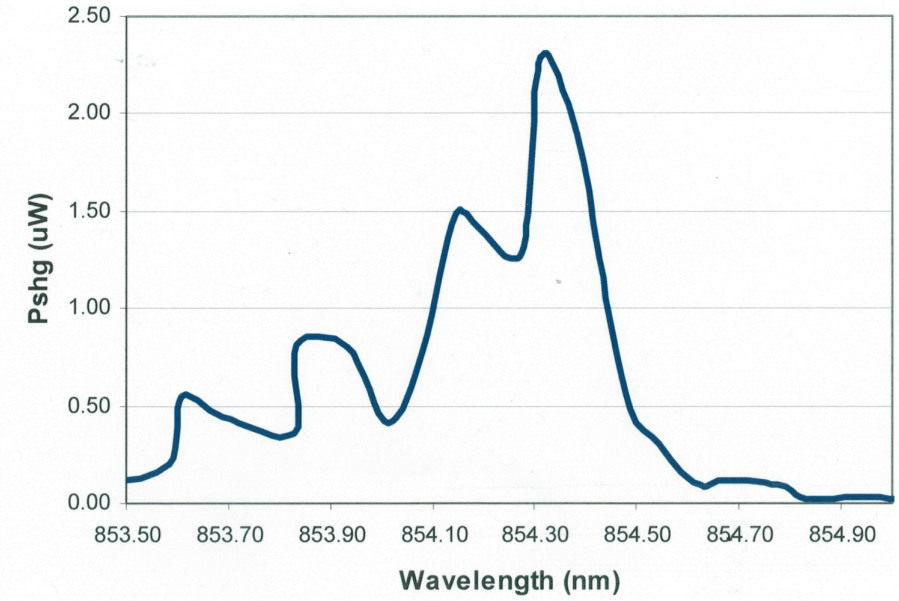

Figure A.7: SHG power for waveguide 5.1 of the second chip for T=23^o C (Advr).

once filtering is applied singles rates are strongly reduced and pump power can be cranked up. In this case, detection will be ultimately limited by rates at the FBG arm. By using a spectral filtering of 1.5 GHz as the FBG used in the OPO experiment, and scaling the spectrum of the singles rates proportionally the power could be increased in a factor of 30, which leads to ~ 13.5 coincidences per second, which is still below the bulk source rate. This is nevertheless a coarse estimation and although conditions could be improved by a better redistribution of the spectral power by improving alignment conditions this is not easy to achieve given the high numerical aperture required for coupling and asymmetrical shape of the waveguide modes. Finally, by using the detected numbers (without filtering) an estimated spectral brightness of 0.045 coinc./(s mW MHz) is determined for the 22 Mhz and 1.5 mW pump power.

A.4. Conclusions

A PPKTP waveguide crystal has been used for degenerate pair creation at 854 nm. From characterization measurements a strong multi-mode behavior has been observed. Although using filtering could help to get a clean single-photon source for ion-interaction experiments, it seems not to be the most convenient tool for narrow-band photons generation. As suggested earlier, single-narrowband photons would require strong filtering in both arms, otherwise photon belonging to different modes produce a strong decrease in the signal-to-background ratio. Although for photon-ion interaction this might not be always required since the ion itself works as a filter, these are necessary for its characterization. Customized bandpass filters centers at 854 nm could be used to cut-off most of the resonant modes far apart (~nm, as seen in the spectra), however the manufacture of these results to be rather expensive, making the use of fiber-Bragg gratings a much better commercially available option. The use of lens-based monolithic filters is also a good option, they present a

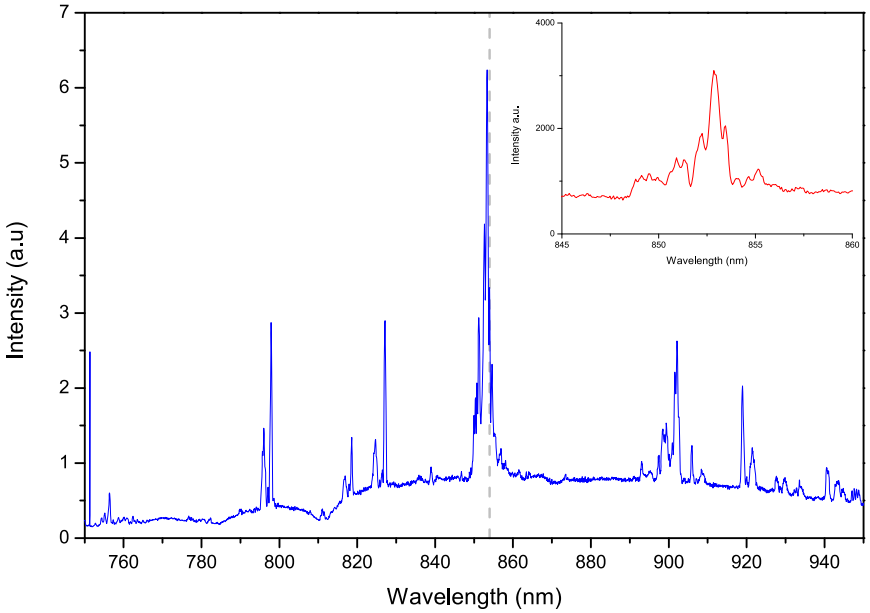

Figure A.8: Spectra of emitted SPDC photons of waveguide 5.1 of the second chip, for T=23 C. The gray dashed line indicates the central wavelength at 854 nm. The inset shows a higher resolution view of the central peak.

convenient efficiency-bandwidth trade-off. These filters have shown good performance when used for similar purposes [124]. Such monolithic filters have been constructed by S. Kucera for an alternative posterior project which could be implemented for such a characterization, although they will not increase the brightness of the source. One could select a very narrow spectral window and increase the power for increasing the photon production proportionally, although this way higher order modes could be excited and the multi-photon generation could spoil statistics and entanglement quality.

Customized manufacture of a PPKTP waveguide could help to improve such problems. As indicated in [121], spectral separation of the modes can be engineered such the modes are produced far apart the region of interest and thus be easily filtered out with bandpass filters. The use of shorter crystals (1 cm) is also recommended, since the probability of uniformities in the grating is higher for longer crystals. Additionally, other applications can be implemented with such a source, QKD protocols, frequency conversion and squeezing as discussed in [117, 125, 126]. Also, the use of the multiple modes for higher-dimension entanglement could be evaluated [123] however these applications are out of the scope of our current experiments. As a conclusion, a more appropriate approach for a high-brightness narrow band photon source seems to be the construction of a photon sourced based in a bulk crystal with cavity enhancement as the OPO source presented in this thesis. Compatibility with degenerate emission would be required, in order to provide polarization entanglement, as discussed in chapter IV. Such a source is in process of implementation by S. Kucera.

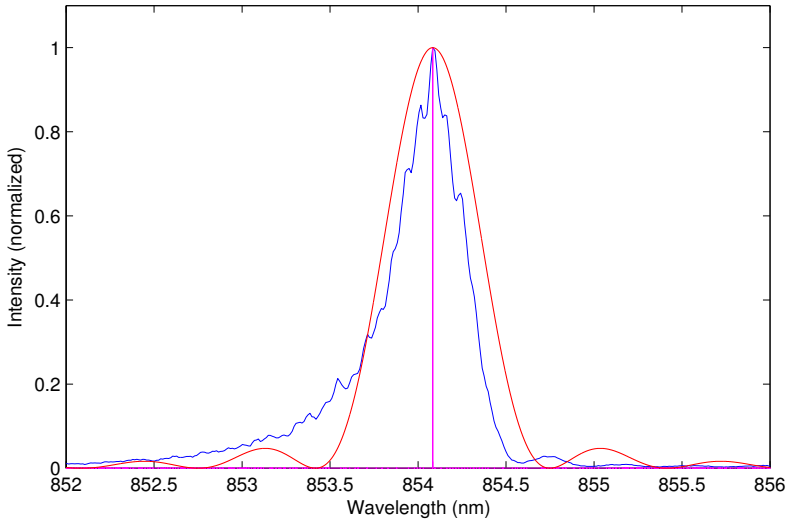

Figure A.9: Spectra of the 854 nm emission for comparison. Solid red line represents the 243 GHz central mode of the waveguide emission in the inset of figure A.8. The solid magenta line corresponds to the 22 MHz bandwidth of interest and blue solid line the measured spectrum of the original bulk SPDC photons.

Appendix B

Journal pre-print versions

In the present appendix, pre-prints of journal versions of results presented in this thesis and whose details are not discussed deeply are attached as complementary information. Further details are given in each section.

B.1. Coherence and entanglement preservation

Results of coherence and Energy-time entanglement preservation using the SPDC-QFC photonic interface have been presented in section III.2.2. Results are presented here in draft format prepared for journal publication including additional details for instance the Time-Bandwidth product of the photons. These data forms part of a set of data also presented in A. Lenhard's thesis [58]. A corrected model for equation (5) exists and corresponding re-analysis of the data in Fig. 6 is pending to be included in the final version of the manuscript.

Coherence and Entanglement Preservation of Frequency-Converted Heralded Single Photons

ANDREAS LENHARD[1], JOSÉ BRITO[1], MATTHIAS BOCK[1], JÜRGEN ESCHNER[1], AND CHRISTOPH BECHER[1,*]

[1]*Fachrichtung 7.2 (Experimentalphysik), Universität des Saarlandes, Campus E2.6, 66123 Saarbrücken, Germany*
[*]*Corresponding author: christoph.becher@physik.uni-saarland.de*

Compiled August 23, 2015

We report on quantum frequency conversion of near infrared photons at a wavelength of 854 nm to the telecommunication O-band at 1310 nm with an over-all conversion efficiency of 8 %. The photons are generated via spontaneous parametric down conversion. One photon is mixed with a strong pump field in a nonlinear ridge waveguide for telecom wavelength conversion. We demonstrate preservation of first and second order coherence of the photons in the conversion process. Based on this we infer the coherence function of the two-photon state and compare it with actual measured one. This measurement demonstrates preservation of time-energy entanglement of the pair. With a visibility of 88 % we further violate a Bell inequality. © 2014 Optical Society of America

OCIS codes:

http://dx.doi.org/10.1364/optica.XX.XXXXXX

1. INTRODUCTION

Long-haul quantum communication requires the transfer of entanglement between remote locations with the help of quantum repeater nodes [1]. Such an architecture relies on photonic qubits to establish entanglement between neighboring nodes [2, 3]. The photons have to be resonant with an atomic transition of the node. As these resonances can usually be found in the near infrared (NIR), the photons will suffer high attenuation in optical fibers. The losses in fibers are minimal at the so called telecom bands between 1260-1650 nm. Quantum frequency conversion (QFC) is a promising technique to bridge the gap between NIR and telecommunication spectral regions by transducing the wavelength of a photonic state. QFC has already been used to transfer single photons between telecommunication wavelengths and NIR either by up conversion [4, 5] or down conversion [6] schemes. Furthermore, the entanglement of a photon with an atomic system [7] as well as with another photon [8–10] is preserved in the conversion process. Hence, next to the development of asymmetric photon pair sources [11], QFC has been demonstrated as a technique to interface quantum memories with telecom wavelengths [12]. Next to storage of qubits, single atoms allow to implement systems for quantum information processing as demonstrated with trapped Calcium ions [13]. With this species further demonstrations of heralded absorption of single photons [14], photonic entanglement in the absorption process [15], bidirectional conversion between atomic and photonic qubits [16–18] and interconnection of distant ions via photons [19–21] have been reported. To implement Ca^+ based nodes into future quantum network infrastructure we here demonstrate QFC between 854 nm, according a transition in Ca^+ and the telecom O-band.

Time-energy or time-bin entanglement seem most feasible for transfer in long-haul fiber networks due to low decoherence. Such qubits have already been used for quantum cryptography with unconditional security [22, 23], as well as for entanglement transfer [24]. QFC is compatible with time-bin [9] or time-energy [8] entanglement as earlier reports have investigated. Time-energy entanglement is an intrinsic property of photon pairs generated by spontaneous parametric down conversion (SPDC). A common way to prove the entanglement is a two-photon interference experiment in a Franson type setup [25]. Similar to single photon interference effects the interference visibility depends on interferometer detunings and Franson interference can thus be used to measure the coherence function of the two-photon state. Apart from such test of fun-

damental quantum properties, Franson interference has been applied for long-range quantum communication [26] based on the time-energy entanglement of photon pair states.

In this article we report on QFC of one photon of a near infrared pair (at resonance wavelength with a transition in Ca^+) to the telecom O-band. We investigate in detail the first and second order coherence of the photons before and after frequency conversion. We further employ Franson interference to demonstrate the time-energy entanglement between the NIR photon and its telecom converted partner and derive the two-photon coherence properties of the pair state. We fond a model connecting the coherence properties of the two-photon state with that of the single photons. All results are affected by spectral filtering during the QFC process which we include in the modeling. With this detailed investigation we demonstrate that QFC is a versatile tool in quantum information processing and networking, preserving initial quantum properties.

2. FREQUENCY CONVERSION

We are aiming on the quantum frequency conversion (QFC) between $\lambda_s = 854$ nm (signal field) and the telcommunications O-band around $\lambda_i = 1310$ nm (idler field). Therefore we use the second-order nonlinear process of difference frequency generation. In this case the down conversion is stimulated by a strong classical pump field at a wavelength around $\lambda_p = 2453$ nm ($1/\lambda_s - 1/\lambda_p = 1/\lambda_i$). The pump field is generated by a home-built continuous wave optical parametric oscillator (OPO). The OPO output wavelength is tunable between 2311 and 2870 nm with single mode, single frequency output powers around 1 W. Hence we can use this feature for tuning of the target wavelength of the conversion process in the entire telecom O-band. The pump power for the conversion process can be controlled by a combination of a polarizer and a waveplate. For efficient down conversion at the single photon level we use ridge waveguide structures (fabricated by NTT), based on a periodically poled lithium niobate core. The chip contains several waveguides with different poling periods for coarse tuning of the phase matching conditions, hence covering the whole telecom O-band. Both, signal and pump field, have to be coupled into the waveguide and good spatial mode overlap is mandatory for high conversion efficiency. The diameter of each beam was individually optimized before combining both on a dichroic mirror. After overlapping, both beams are focused to the waveguide with a single uncoated aspherical lens (Thorlabs A220TM). We reach a coupling efficiency of 84.2 % at 854 nm and 38 % at 2.5 μm (including transmission losses). We suffer from absorption by the lens material resulting in a transmission of only 72.6 % for 2.5 μm. In a future setup we plan to improve this by using ZnSe lenses which have a high transmission over the whole wavelength range. Behind the waveguide the telecom light is collimated by another aspheric lens. Residual signal photons are separated by a dichroic mirror. The coating of all following mirrors is optimized for telecom wavelengths, introducing considerable losses for the pump field. Finally, the telecom photons pass three interference band-pass filters (2x 50 nm FWHM, 1x 12 nm FWHM) with a total transmission of 37 %. This suppresses residual pump light and background photons induced by the pump field via Raman scattering [27], second harmonic generation or higher order nonlinear processes. Then the photons are coupled to a standard telecom fiber (SMF28) with an efficiency of 80 %. We use superconducting single photon detectors (SSPD, Single Quantum EOS X10) with a detection efficiency of 25 % for counting the telecom photons. The complete setup is sketched in Fig. 1.

We generate photons at 854 nm via spontaneous parametric down conversion (SPDC) with a source described earlier in more detail [28, 29]. We start with a diode laser system at 854 nm, actively stabilized to an atomic transition ($^{40}Ca^+$, $3^2D_{5/2} \leftrightarrow 4^2P_{3/2}$). After second harmonic generation (SHG), the laser at 427 nm serves as pump for the SPDC process. We use a 2 cm crystal of bulk, periodically poled KTP (PPKTP) with type-II phase matching conditions to generate frequency degenerate, polarization entangled photon pairs. For the particular experiments we are reporting here, the polarization entanglement is not necessary. Hence we separate signal and idler photons by a polarizing beam splitter. One photon serves as a herald while the other one is coupled to a single mode fiber and sent to the frequency converter setup. The converter is situated in another lab, connected by 90 m of fiber. The spectrum of the photons is shown in the inset of Fig. 2. It was measured with a grating based spectrometer of 1800 lines/mm. The spectrum has a width of 173 GHz (FWHM), which is slightly larger than the phase matching bandwidth of the conversion process (calculated 118 GHz FWHM). Hence the maximum conversion efficiency will be reduced for the outer spectral components. The resulting spectrum of the converted photons will be the product of phase matching and original spectrum. Unfortunately, the resolution of our spectrometer for telecom wavelength range is insufficient to resolve details in the spectrum. Thus we decided to use measurements of first order coherence to gather more information about the spectral properties.

3. FIRST-ORDER COHERENCE

To measure the first order coherence function we set up a Michelson type interferometer. One mirror (M1) is mounted on a linear translation stage moved by a stepper motor and offers a coarse setting of the path length difference of up to 1.7 ns with 7 fs minimum step size. The mirror (M2) in the other arm is mounted on a piezo translator for fine movement. The input and output beam paths are coupled to single mode fibers. We use silver coated mirrors to allow operation over a wide wavelength range. The interferometer can be used for 854 nm as well as for 1310 nm by exchanging the fiber couplers and the 50/50 beam splitter and quick realignment.

We start with a measurement of the first-order coherence function of the original 854 nm SPDC photons. Therefore the delay was set via the translation stage to several values around the zero delay position. At each position the mirror M2 was scanned via the piezo translator and the count rate behind the interferometer was recorded with 100 ms integration time. We observed interference fringes in the count rate. These fringes were fitted by a sine function and the visibility $V = \frac{I_{max}+I_{min}}{I_{max}-I_{min}}$ was calculated from the fit data. In a preparatory measurement with a long-coherence laser we find a maximum visibility of 88 % which we attribute to imperfect alignment and beam overlap in the interferometer. We use this value as an upper limit for the measurement apparatus. The final results for the 854 nm SPDC photons are shown in Fig. 2. We also achieve a maximum visibility of 88 % which means it is limited by the measurement device. As we have additionally measured the spectrum of the photons with high resolution (see inset of Fig. 2) we can derive the envelope of the first order coherence function by Fourier transformation of the power spectrum. The result is shown as solid line in Fig. 2, where the peak height is fitted

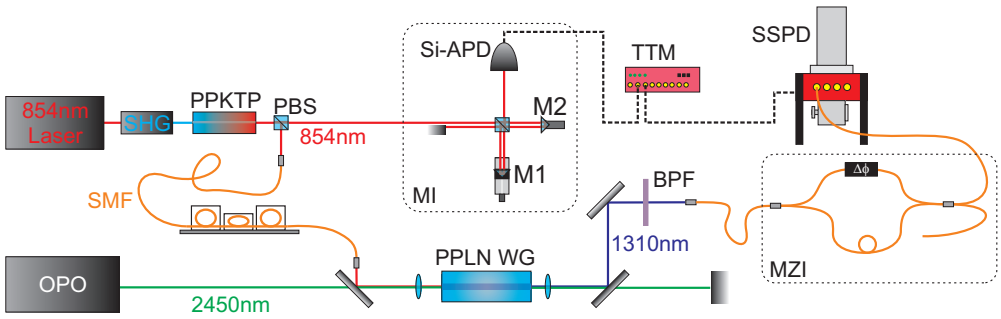

Fig. 1. Experimental setup with SPDC source, frequency converter and interferometers for Franson interference. PBS: polarizing beam splitter; TTM: time tagging module; PPLN WG: PPLN waveguide; BPF: band pass filters.

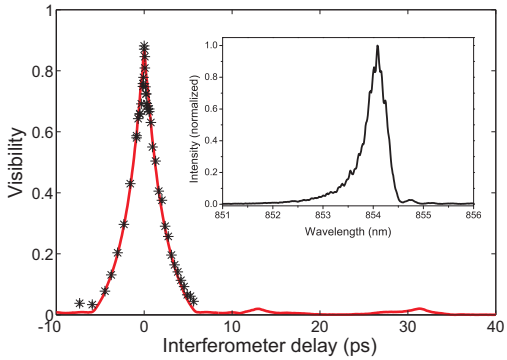

Fig. 2. First order coherence function of the 854 nm single photons. The red solid line shows the calculation derived from the spectrum, shown in the inset. The black stars mark the measured visibilities.

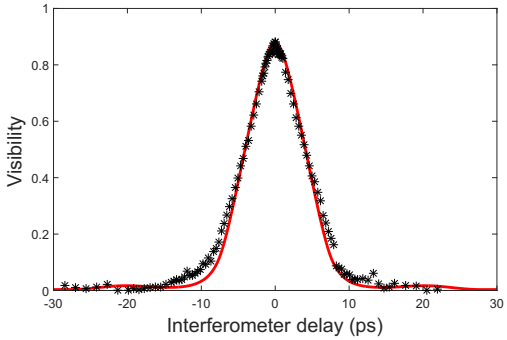

Fig. 3. Measured first order coherence function of the converted 1310 nm telecom single photons (black stars). The solid line shows a model fitted to the data.

to the measured data. The shape of both curves overlap well, proving the consistency of both measurement methods in time and frequency domain. We can estimate the coherence time τ_c via integrating the first order coherence function:

$$\tau_c = \int_{-\infty}^{\infty} dt \left| g^{(1)}(t) \right|^2 \quad \textbf{(1)}$$

With this method we find a coherence time of $\tau_{854} = 3.7$ ps for the 854 nm photons. In analogy we define the spectral bandwidth of the photons by integration of the normalized spectral intensity:

$$\Delta\nu = \int_{-\infty}^{\infty} d\nu I(\nu) / \max(I(\nu)) \quad \textbf{(2)}$$

This gives a more reliable value regarding the dissimilar shapes of the spectra reported in this paper. Here it results in $\Delta\nu_{854} = 308$ GHz. With the help of these two equations we can also define the Time-Bandwidth-Product: $TBP = \tau_c \cdot \Delta\nu$. For the original photons we find $TBP_{854} = 1.14$.

Next, we exchange the optics set of the interferometer as briefly described before and repeat the measurement for the converted photons. The resulting first order coherence function of the telecom photons is shown in Fig. 3. In the same way as for the photons at the original wavelength we determine a coherence time of $\tau_{1310} = 10.5$ ps which is significantly larger than before. This is due to the fact that the phase matching spectrum of the conversion process is more narrow than the spectrum of the SPDC photons. The QFC process here acts as a spectral filter. This results in a reduced bandwidth after the conversion process and hence a larger coherence time. The shape of the coherence function also slightly changed due to the shape of the phase matching curve. We can estimate the spectrum of the converted photons as the product of the original spectrum and the sinc^2-function of the QFC phase matching function ($\Delta\nu_{\mathrm{sinc}^2} = 131.4$ GHz). The resulting spectrum has a bandwidth of $\Delta\nu_{1310} = 101.3$ GHz, corresponding to a $TBP_{854} = 1.06$ which is close to the original one. When we calculate the Fourier transform of this inferred spectrum we end up with an estimate of its coherence function. The result is shown as a solid line in Fig. 3, where we fitted the peak value to the measured data. The good agreement of its shape with the measured data encourages the validity of our model.

4. FRANSON INTERFERENCE

Due to their generation process we expect that the SPDC photon pairs are time-energy entangled. Furthermore we expect this entanglement to be preserved in the frequency conversion

process. This is due to the fact that we use a continuous wave pump field with long coherence time for the conversion. We measured the frequency of the pump field with the help of a wavemeter (High Finesse WS6-200): The peak to peak fluctuations were below 200 MHz over 10 h of measurement time. The Allan deviation of the frequency fluctuations was less 2 MHz for integration times below 100 s. Hence we can state the bandwidth of the pump field is much smaller than that of the signal photons and will not disturb the temporal properties of the photons but only introduce a constant and well-defined frequency shift. However, we already saw that the coherence function changes due to the finite width of the phase matching function. One common procedure to prove the time-energy entanglement of photon pairs was proposed by Franson [25]. This involves sending both photons of the pair through individual interferometers which are equally unbalanced and detecting the photon coincidences at the interferometer outputs. The observation of a visibility exceeding 0.5 is a signature for entanglement [30]. The experimental details will be discussed in the following. Such an experiment, involving frequency up conversion was first reported by Tanzilli [8]. We here report on frequency down conversion and furthermore on the measurement of the coherence function of the photon pair state over a wide delay range. The results are compared with expectations from a theoretical model based on the single photon interference experiments.

To observe Franson interference two interferometers are necessary: For the 854 nm photons we use the Michelson interferometer (MI) described earlier. For the converted photons we set up another interferometer in Mach-Zehnder (MZI) geometry. As it will be operated at telecom wavelengths we set it up from fiber components. It consists of two fiber beam splitters, a phase modulator (Phoenix photonics) and a delay fiber. All components are non-polarization maintaining but we controlled the polarization state by fiber strain. From a preparatory measurement with a laser we find a maxiumum achievable visibility of 94 %. To observe interference fringes in coincidence detection, we have to suppress first order interference effects. This means choosing the delay much larger than the coherence time ($\tau_c = 10.5$ ps). On the other hand, the delay must be smaller than the coherence time of the pump laser generating the photon pairs (line width in the low MHz range). In our case the delay is limited to 1.7 ns by the size of the MI. In particular we here chose a delay of 1.14 ns (fixed length of delay fiber in MZI), fulfilling all requirements. Both photons of the pair are generated simultaneously within the pump coherence time and then travel either the short or the long path in their interferometer. To erase which-path information the delays in both interferometers thus have to be equal. We can set the detuning of the MI to the appropriate value via the motorized mirror (M1). Then we measure coincidences between the 854 nm photons passing the MI and the converted telecom photons passing the MZI. The measured coincidence function is shown as inset in Fig. 4. We observe three peaks due to the different path combinations. The central peak contains the coincidence events from indistinguishable paths, i.e. where both photons travel either the long or the short path in their individual interferometer. Hence we will cut out the coincidences from this central peak in the post processing in a gate window of 512 ps, as indicated by the shaded region. The dips between the peaks do not reach zero coincidences due to the timing jitter of our single photon detectors for 854 nm (Si-APD, jitter ca. 600 ps).

The coincidence rate detected in such a Franson experiment was theoretically described by Ou [31]:

$$R_{AB}^{(2)} \propto 1 + F\left(T_A - T_B\right)\left|\gamma_p\left(\frac{T_A + T_B}{2}\right)\right| \cdot \cdot \cos\left[\omega_p\left(T_A + T_B\right)/2 + \phi_0\right] \quad (3)$$

It oscillates in dependence of the phase between the photons (proportional to the detunings T_A, T_B). The amplitude of the oscillation depends on the coherence of the pump, described by $\gamma_p(\tau)$, which we can set to $\gamma_p = 1$ as we operate the interferometers with delay far below the pump coherence time. In our case the dominating term is:

$$F(\tau) = \frac{\int_{-\infty}^{+\infty} g_A(t)\, g_B^*(t+\tau)\, dt}{\int_{-\infty}^{+\infty} g_A(t)\, g_B^*(t)\, dt} \quad (4)$$

This is the normalized convolution of the first-order coherence functions of photons A and B of the pair. This function has a maximum of one for equally imbalanced interferometer delays and decreases to zero for large differences in the delays. We can attribute this function to the first order coherence of the photon pair state. As we already know the first-order coherence functions of the single photons, we can directly calculate this function from the measured data given earlier (shown in Fig. 2 and Fig. 3). The resulting calculation for $F(\tau)$ is shown as solid line in Fig. 4 (In the figure we fitted the peak value of $F(\tau)$ to best match the experimental data).

In the experiment we coarsely set the difference in delay via mirror M1 in the MI. We then scan the phase via mirror M2 to see fringes in the coincidences. The 854 nm photons behind the MI are detected with a Si-APD (Perkin Elmer SPCM-AQR-14) and the telecom photons are detected with the SSPD. The detection events are recorded by a time-tagging module (TTM8000). The post-processing of the data is implemented in software, operating on the recorded click lists.

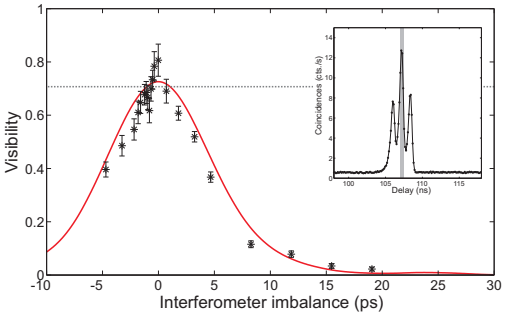

Fig. 4. Two-photon coherence measurement: Measured interference fringe visibility (black stars) for different detunings between the interferometers. The red solid line shows the expected curve calculated from first-order coherence functions. The horizontal line at a visibility of 71 % indicates the upper boundary given by the Bell inequality. The inset shows a long-term average correlation function between the two detectors. The gray shaded area indicates the post-selected time-interval with indistinguishable paths-combinations.

After fitting the peak height of the theoretical curve to the experimental data we see a clear overlap in shape and width

of both curves. With this comparison we bridge the gap between independent measurements concerning the single photon wave functions and the pair state wave function. Deviations can partly emerge from the finite number of data points and measurement range put into the numerical calculations. From the experimental data points we derive a coherence time of $\tau_{\text{pair}} = 12.4$ ps. To calculate the TBP for this measurement we take into account that a convolution of the spectra of both photons of the pair contributes to this coherence function. Following the previous assumptions in the paper we find for this convolution a bandwidth of $\Delta\nu_{\text{pair}} = 84.7$ GHz, resulting in $TBP_{\text{pair}} = 1.05$. Which is again close to the previous results, confirming consistency between the measurement methods. The bandwidth values are summarized in table 1.

	τ_c	$\Delta\nu$	TBP
854 nm	3.7 ps	308.3 GHz	1.14
1310 nm	10.5 ps	101.3 GHz	1.06
Pair	12.4 ps	84.7 GHz	1.05

Table 1. Bandwidth parameters resulting from the first order coherence measurements.

The visibility is ultimately limited by the measurement apparatus, corresponding to the product of the maximum visibilities of both interferometers: $V_{\text{max}} = 0.88 \cdot 0.95 = 84$ %. The maximum visibility of the Franson fringes was found as 80.7 ± 6 %. When the background coincidences are subtracted, this value increases to 83.7 ± 7.7 %. The corrected value thus equals the maximum of $V_{\text{max}} = 84$ % derived from single-photon coherence measurements.

As the visibility exceeds by far the critical value of 50 % we clearly proved the conservation of time-energy entanglement in the frequency down-conversion process. Following the interpretation in [8] we can define an entanglement transfer fidelity of $F = \frac{1+V_{\text{net}}}{2} = 91.9 \pm 3.9$ % for our frequency converter. This value is again limited by the measurement apparatus to $F_{\text{max}} = 92$ %. To this end we have to claim that the original photon pair is in a maximally time-energy entangled state. Unfortunately we could not prove this due to limitations in our measurement devices. In the case of non-ideal fidelity of the input state our result of F gives a lower limit for the actual state transfer fidelity. In any case we can claim that our frequency converter transfers an entangled state from NIR photon pairs to NIR-telecom photon pairs with nearly perfect fidelity. Time-energy entangled photon pairs are also suited to perform Bell-tests. A Bell inequality can be derived depending on the Franson interference visibility [26]. One can find that the Bell inequality defines an upper boundary for the visibility of $V \leq \frac{1}{\sqrt{2}} \approx 70.7\%$. From our experimental findings we see a clear violation of the Bell inequalities as the visibility significantly exceeds the boundary value by 1.7 error margins.

All results shown above for the two-photon interference were achieved by scanning the phase via the piezo mounted mirror M2 in the Michelson interferometer. It is worth mentioning that we observed the same visibility by scanning the phase in the Mach-Zehnder interferometer. Additionally we can scan the phases in both interferometers simultaneously, resulting in a fringe pattern that can be described with the sum of two sin-functions (with two different phase scanning periods). These

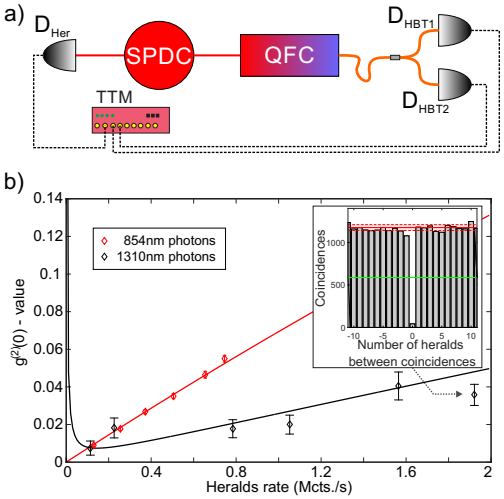

Fig. 5. Measurement of heralded second order correlation $g^{(2)}(0)$ for different heralding rates. a) shows the measurement setup, SPDC: pair source, QFC: quantum frequency conversion. For details see text. b) shows the experimental results of $g^{(2)}(0)$-values. The red data points are measured at 854 nm without QFC. The black data include QFC before the HBT interferometer. The error bars are calculated including $\sqrt{N}$-noise of the coincidences. The solid lines result from the model based on the SBR, as described in the text. The inset exemplary shows a histogram used to calculate $g^{(2)}(0)$.

observations prove that the coincidence rate indeed depends on the sum of the phases of both interferometers, as predicted by equation 3 and demonstrated earlier [26].

5. SECOND-ORDER COHERENCE

After proving the preservation of first-order coherence properties we next check the second-order coherence, i.e. the intensity correlation of the photons. We are especially interested in the correlation at zero time delay ($g^{(2)}(0)$-value) which can be used to describe the purity of a single photon state. A popular application of SPDC is the generation of heralded single photons. In detail this means once a herald photon is detected the corresponding field in the partner mode is projected into a state which can be an arbitrarily close approximation to a single photon Fock state [32]. The deviation from ideal single photons is due to the fact that the creation of pairs by SPDC follows a thermal distribution. Hence there is a non-vanishing probability to generate multiple pairs at the same time. This distribution depends on the pump power of the SPDC process which allows to reduce the multi-pair contribution by reduced pump power. We measure the correlation with a Hanburry-Brown Twiss (HBT) interferometer. Our setup is illustrated in Fig. 5a. The HBT interferometer consists of a 50/50 fiber beam splitter with both outputs connected to a SSPD. We record the detection time tags of the heralds and the HBT detectors and heralding is realized in the post-processing. To analyze the data and calculate the $g^{(2)}(0)$-values we follow the method described in [33].

We first measured the rate of herald photons for different pump powers. Their linear dependence shows that we can neglect multi-photon events. Then we determine the $g^{(2)}(0)$-values for different pump powers of the SPDC source. As a reference we first perform this experiment without frequency conversion, i.e. all detected photons are at 854 nm. The result is shown as red data points in Fig. 5b. Instead of the pump power we use the herald rate as a scaling of the x-axis. Next, we include the frequency converter before the HBT and repeat the measurement. The results are shown as black data points in the same figure 5. There are two results we want to focus: First, the curve for the converted photons increases with a lower slope and second, in the extrapolation to vanishing heralds rate there seems to be an offset in the $g^{(2)}(0)$-value for the converted photons while this is not the case without QFC.

To explain this we first determine the signal to background ratio (SBR, ρ) for each measurement setting. To this end we use the signal-idler correlations i.e. temporal correlations between the herald, measured with D_{Her} and one of the HBT outputs, D_{HBT1} and define the SBR as the ratio between the coincidence rate in the signal bin (Signal) and the average coincidence rate at time bins with larger delay (Background). This is illustrated in the inset of Fig. 6. As a first approximation we assume that

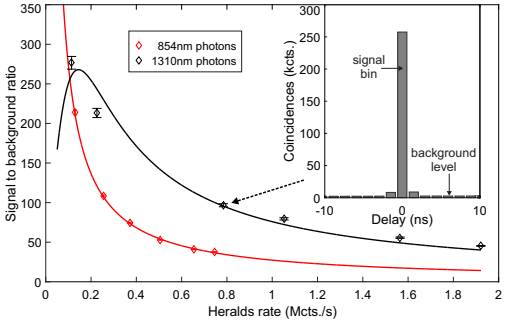

Fig. 6. Signal to background ratio for different SPDC pump powers, calculated from signal-idler coincidences. The solid lines are fits to the data, for details see text. The inset shows an exemplary signal-idler coincidence measurement for the converted photons, used to calculate the SBR.

the signal coincidence rate increases linearly with SPDC pump power. A deviation from this is expected when multi-pair detection events start playing a role. On the other hand we find two contributions to the background: If a background event is formed by coincidence detection of uncorrelated photons, created in a scattering process, its rate increases proportional to the square of the pump power (or the rate of heralds). Furthermore we find coincidences which are independent of the SPDC process and thus described with a constant rate. These can be detector dark counts (which are at negligible low rates, compared to the true coincidences) or noise photons introduced by the QFC process. To this end we can describe the SBR with the following model function:

$$\rho = \frac{R_{Her}}{\alpha \cdot R_{Her}^2 + \beta} \quad \textbf{(5)}$$

Where the fitting parameters α and β are summarized in table 2. The fit curves are shown as solid lines in Fig. 6 and describe our

Wavelength	α (s)	β (s^{-1})
854 nm	$3.655 \cdot 10^{-8} \pm 3.9 \cdot 10^{-10}$	0
1310 nm	$1.29 \cdot 10^{-8} \pm 1.0 \cdot 10^{-9}$	271 ± 41

Table 2. Fit parameters resulting from model describing the SBR of the heralded $g^{(2)}(0)$ measurement.

data very well. The curve of the original photons can be well described without contribution of constant noise (β parameter). In this model the SBR increases to infinity for vanishing heralding rate. This is not the case when β is included. When the pump power is decreased and the signal coincidence rate becomes comparable to the constant background rate, the measured SBR reaches a maximum. For lower pump power the background starts to dominate, decreasing the SBR. On the other hand, the SBR is in general larger for the converted photons than for the original photons. In the model this is accounted for by the lower α parameter. We can explain this again by the spectral filtering effect of the QFC process observed in the first-order coherence measurements affecting both signal and noise photons. Starting from this model we can now describe the results of the heralded second-order coherence measurement. The $g^{(2)}(0)$-value depends on the signal to background ratio ρ via [34]:

$$g^{(2)}(0) = 1 - \left(\frac{\rho}{\rho+1}\right)^2 \quad \textbf{(6)}$$

This curve is plotted as solid line in Fig. 5b. The explanation of the offset of the $g^{(2)}(0)$-values for the QFC measurement at vanishing SPDC pump is due to noise generated in the QFC process. This noise is not correlated to the SPDC signal and will itself deliver $g^{(2)}(0) = 1$. It becomes the dominating part at very low pump powers, increasing the $g^{(2)}(0)$-value. The lower SBR of the converted photons due to the filtering effect then results in lower $g^{(2)}(0)$-values.

We observed a very high SBR and accordingly low $g^{(2)}(0)$-values, even at high pump powers. This proves the applicability of our system as source for heralded single photons at telecom wavelengths.

6. SUMMARY AND CONCLUSION

We demonstrated quantum frequency conversion of heralded single photons at 854 nm to the telecom O-band with a conversion efficiency of 8 %. We then investigated the coherence properties of the photons in detail. Insufficient bandwidth of the conversion process results in spectral filtering affecting first and second-order coherence properties of the photons. In both cases our model could perfectly explain the results. We further used the results from first-order coherence measurements of the single photons to explain the results for the two-photon state showing the dependence of the pair properties on their individual constituents. In summary, via this detailed characterization we demonstrated that the QFC process preserves the coherence properties of the photons.

The SPDC photons are intrinsically time-energy entangled. With the observation of Franson interference we prove that this entanglement is preserved in our frequency converter. The observed raw visibility was high enough to violate the Bell inequality proving fundamental aspects of quantum mechanics, i.e. that the results do not obey a local-realistic theory. The

transfer of the time-energy entanglement between the NIR photon pairs and the NIR-telecom pair can be realized with a fidelity around 92 %. The frequency translation of entanglement is an essential ingredient for long-range, fiber based quantum networks. The high fidelity demonstrates the feasibility to include QFC in quantum information processing.

The preservation of the intensity correlations and especially the observation of $g^{(2)}(0) << 1$ proves the single photon character of the converted photons. The preservation of the single photon state during QFC has been demonstrated earlier [6] and here we were able to extend this observation to photons generated by SPDC. The spectral filtering effect additionally increases single photon purity. This opens the way for our system as a source for heralded single photons at telecom wavelengths.

The frequency conversion of time-energy entanglement between near infrared and telecom wavelengths shows that QFC is a versatile interface for quantum communication and quantum networks. For the source reported here the center wavelength of the SPDC photons is stabilized to an atomic transition in calcium. As we are able to convert the SPDC photons with our frequency converter, preserving temporal correlation, time-energy entanglement and heralded single photon state, we plan to use the converter for a heralded absorption experiment [29] where we convert the heralding photon to a telecom wavelength. Furthermore, with the current setup we are able to convert single photons, emitted from a single trapped ion, to the telecom band. Future developments will include advancements in the setup to enable polarization independent conversion. This would allow the conversion of polarization qubits which are preferred in many quantum communication schemes. The transition at 854 nm in $^{40}Ca^{+}$ seems to be feasible for such atom-photon interfaces [16, 17].

FUNDING INFORMATION

The work was funded by the German federal ministry of science and education within the project "Q.com-Q" (contract No. 16KIS0127). J. Brito acknowledges support by CONICYT.

REFERENCES

1. H.-J. Briegel, W. Dür, J. I. Cirac, and P. Zoller, "Quantum Repeaters: The Role of Imperfect Local Operations in Quantum Communication," Phys. Rev. Lett. **81**, 5932-5935 (1998).
2. L.-M. Duan, M. D. Lukin, J. I. Cirac, and P. Zoller, "Long-distance quantum communication with atomic ensembles and linear optics," Nature **414**, 413-418 (2001).
3. C. Simon, H. de Riedmatten, M. Afzelius, N. Sangouard, H. Zbinden, and N. Gisin, "Quantum Repeaters with Photon Pair Sources and Multimode Memories," Phys. Rev. Lett. **98**, 190503 (2007).
4. M. T. Rakher, L. Ma, O. Slattery, X. Tang, and K. Srinivasan, "Quantum transduction of telecommunications band single photons from a quantum dot by frequency upconversion," Nat. Photon. **4**, 786-791 (2010).
5. S. Ates, I. Agha, A. Gulinatti, I. Rech, M. T. Rakher, A. Badolato, and K. Srinivasan, "Two-Photon Interference Using Background-Free Quantum Frequency Conversion of Single Photons Emitted by an InAs Quantum Dot," Phys. Rev. Lett. **109**, 147405 (2012).

REFERENCES

6. S. Zaske, A. Lenhard, C. A. Keßler, J. Kettler, C. Hepp, C. Arend, R. Albrecht, W.-M. Schulz, M. Jetter, P. Michler, and C. Becher, "Visible-to-Telecom Quantum Frequency Conversion of Light from a Single Quantum Emitter," Phys. Rev. Lett. **109**, 147404 (2012).
7. K. De Greve, L. Yu, P. L. McMahon, J. S. Pelc, C. M. Natarajan, N. Y. Kim, E. Abe, S. Maier, C. Schneider, M. Kamp, S. Höfling, R. H. Hadfield, A. Forchel, M. M. Fejer, and Y. Yamamoto, "Quantum-dot spin–photon entanglement via frequency downconversion to telecom wavelength," Nature **491**, 421-425 (2012).
8. S. Tanzilli, W. Tittel, M. Halder, O. Alibart, P. Baldi, N. Gisin, and H. Zbinden, "A photonic quantum information interface," Nature **437**, 116-120 (2005).
9. R. Ikuta, Y. Kusaka, T. Kitano, H. Kato, T. Yamamoto, M. Koashi, and N. Imoto, "Wide-band quantum interface for visible-to telecommunication wavelength conversion," Nat. Commun. 2:537 doi: 10.1038/ncomms1544 (2011).
10. S. Ramelow, A. Fedrizzi, A. Poppe, N. K. Langford, and A. Zeilinger, "Polarization-entanglement-conserving frequency conversion of photons," Phys. Rev. A **85**, 013845 (2012).
11. J. Fekete, D. Rieländer, M. Cristiani, and H. de Riedmatten, "Ultranarrow-Band Photon-Pair Source Compatible with Solid State Quantum Memories and Telecommunication Networks," Phys. Rev. Lett. **110**, 220502 (2013).
12. B. Albrecht, P. Farrera, X. Fernandez-Gonzalvo, M. Cristiani, and H. de Riedmatten, "A waveguide frequency converter connecting rubidium-based quantum memories to the telecom C-band," Nat. Commun. 5:3376 doi: 10.1038/ncomms4376 (2014).
13. P. Schindler, D. Nigg, T. Monz, J. T. Barreiro, E. Martinez, S. X. Wang, S. Quint, M. F. Brandl, V. Nebendahl, C. F. Roos, M. Chwalla, M. Hennrich, and R. Blatt, "A quantum information processor with trapped ions," New J. Phys. **15**, 123012 (2013).
14. N. Piro, F. Rohde, C. Schuck, M. Almendros, J. Huwer, J. Ghosh, A. Haase, M. Hennrich, F. Dubin, J. Eschner, "Heralded single-photon absorption by a single atom", Nat. Phys. **7**, 17-20 (2011).
15. J. Huwer, J. Ghosh, N. Piro, M. Schug, F. Dubin and J. Eschner, "Photon entanglement detection by a single atom", New J. Phys. **15**, 025033 (2013).
16. A. Stute, B. Casabone, P. Schindler, T. Monz, P. O. Schmidt, B. Brandstätter, T. E. Northup, and R. Blatt, "Tunable ion–photon entanglement in an optical cavity," Nature **485**, 482-485 (2012).
17. C. Kurz, M. Schug, P. Eich, J. Huwer, P. Müller, and J. Eschner, "Experimental protocol for high-fidelity heralded photon-to-atom quantum state transfer," Nat. Commun. 5:5527, doi: 10.1038/ncomms6527 (2014).
18. B. Casabone, K. Friebe, B. Brandstätter, K. Schüppert, R. Blatt, and T. E. Northup, "Enhanced quantum interface with collective ion-cavity coupling", Phys. Rev. Lett. **114**, 023602 (2015).
19. D. L. Moehring, P. Maunz, S. Olmschenk, K. C. Younge, D. N. Matsukevich, L.-M. Duan and C. Monroe, "Entanglement of single-atom quantum bits at a distance", Nature **449**, 68 (2007).
20. M. Schug, J. Huwer, C. Kurz, P. Müller, J. Eschner, "Heralded Photonic Interaction between Distant Sin-

gle Ions", Phys. Rev. Lett. **110**, 213603 (2013).
21. D. Hucul, I. V. Inlek, G. Vittorini, C. Crocker, S. Debnath, S. M. Clark, and C. Monroe, "Modular entanglement of atomic qubits using photons and phonons," Nature Phys. **11**, 37-42 (2015).
22. W. Tittel, J. Brendel, H. Zbinden, and N. Gisin, "Quantum Cryptography Using Entangled Photons in Energy-Time Bell States," Phys. Rev. Lett. **84**, 4737 (2000).
23. Z. Zhang, J. Mower, D. Englund, F. N. C. Wong, and J. H. Shapiro, "Unconditional Security of Time-Energy Entanglement Quantum Key Distribution Using Dual-Basis Interferometry," Phys. Rev. Lett. **112**, 120506 (2014).
24. C. Clausen, I. Usmani, F. Bussieres, N. Sangouard, M. Afzelius, H. de Riedmatten, N. Gisin, "Quantum storage of photonic entanglement in a crystal", Nature **469**, 508 (2011).
25. J. D. Franson, "Bell Inequality for Position and Time," Phys. Rev. Lett. **62**, 2205-2208 (1989).
26. W. Tittel, J. Brendel, N. Gisin, and H. Zbinden, "Long-distance Bell-type tests using energy-time entangled photons," Phys. Rev. A **59**, 4150-4163 (1999).
27. S. Zaske, A. Lenhard, and C. Becher, "Efficient frequency downconversion at the single photon level from the red spectral range to the telecommunications C-band," Opt. Express **19**, 12825-12836 (2011).
28. N. Piro, A. Haase, M. W. Mitchell, and J. Eschner, "An entangled photon source for resonant single-photon–single-atom interaction," J. Phys. B: At. Mol. Opt. Phys. **42**, 114002 (2009) .
29. N. Piro, F. Rohde, C. Schuck, M. Almendros, J. Huwer, J. Ghosh, A. Haase, M. Hennrich, F. Dubin, J. Eschner, "Heralded single-photon absorption by a single atom", Nat. Phys. **7**, 17-20 (2010).
30. J. D. Franson, "Violations of a Simple Inequality for Classical Fields," Phys. Rev. Lett. **67**, 290-293 (1991).
31. Z. Y. J. Ou, "Multi-Photon Quantum Interference," Springer Science+Business Media, New York (2007).
32. A. Christ, and Ch. Silberhorn, "Limits on the deterministic creation of pure single-photon states using parametric down-conversion," Phys. Rev. A **85**, 023829 (2012).
33. S. Fasel, O. Alibart, S. Tanzilli, P. Baldi, A. Beveratos, N. Gisin, and H. Zbinden, "High-quality asynchronous heralded single-photon source at telecom wavelength," New J. Phys. **6**, 163 (2004).
34. C. Becher, A. Kiraz, P. Michler, A. Imamoglu, W. V. Schoenfeld, P. M. Petroff, L. Zhang, and E. Hu, "Nonclassical radiation from a single self assembled InAs quantum dot," Phys. Rev. B **63**, 121312(R) (2001).

B.2. Telecom wavelength multiplexing using frequency conversion

This paper presents results of the multiplexing of classical and quantum states using a common transmission channel in the telecom band, generated using a SPDC+QFC interface. This experiment has been briefly described as in section III.5. Results are also in [74], and published in [85], presented here in a pre-print format.

Single Telecom Photon Heralding by Wavelength Multiplexing in an Optical Fiber

Andreas Lenhard, José Brito, Stephan Kucera, Matthias Bock, Jürgen Eschner, and Christoph Becher
Experimentalphysik, Fachrichtung 7.2, Universität des Saarlandes, Campus E2.6, 66123 Saarbrücken, Germany

We demonstrate the multiplexing of a weak coherent and a quantum state of light in a single telecommunication fiber. For this purpose we make use of spontaneous parametric down conversion and quantum frequency conversion to generate photon pairs at 854 nm and the telecom O-band. The herald photon at 854 nm triggers a telecom C-band laser pulse. The telecom single photon (O-band) and the laser pulse (C-band) are combined and coupled to a standard telecom fiber. Low-background time correlation of the weak coherent and quantum signal behind the fiber shows successful multiplexing.

INTRODUCTION

Today's Internet traffic that is distributed over optical fiber channels mainly concentrates on the telecom C- (1530 - 1565 nm) and L-band (1565 - 1625 nm) because in-line active amplifiers based on erbium-doped fibers offer a feasible way to build repeaters for the signals. Hence there exist a number of telecom frequency bands which are not used, being available for quantum communication.

In state of the art realizations, quantum key distribution (QKD) is possible over 336 km [1] and entanglement distribution was demonstrated with lengths up to 300 km [2]. QKD with such high loss channels became possible only with the development of low-noise detectors [3]. Based on this progress, QKD over existing fiber networks in urban areas has been demonstrated [4–6] as well as entanglement distribution [7] and teleportation [8].

QKD protocols, e.g. BB84 [9], usually involve an exchange of data via a quantum and a classical channel simultaneously to establish the final secret key. Realizing both channels in a single fiber reduces the demand for fiber infrastructure at the cost of slightly increasing the device complexity at sending and receiving stations. In first experimental demonstrations, weak coherent pulses at the single photon power level in the telecom O-band (1260 - 1360 nm) were multiplexed with a common data channel in the C-band and sent via several kilometers of installed fiber [10] with an acceptable error rate of the quantum channel. The dominant noise source in that scheme is anti-Stokes Raman scattering of the strong classical pulses into the quantum channel [11]. Furthermore, it is also possible to transmit the O-band photons through a fiber link equipped with active erbium amplifiers. The spontaneous emission of the amplifiers at O-band wavelengths is quite low and the amount of additional noise photons in the quantum channel can be neglected after narrow spectral filtering [12]. However, each amplifier attenuates the O-band photons (e.g. 11 dB loss in [12]). Nevertheless, in such a configuration the distribution of entangled states was demonstrated [12]. In recent work [13] a scheme was presented where the amplifiers were by-passed and noise in the O-band was investigated in detail.

The telecom C-band is divided into a grid of equally spaced channels for dense wavelength multiplexing (12.5 GHz - 100 GHz spacing in ITU-grid [14]). Each of these channels can be used independently for classical communication and filters are available to separate and demultiplex individual channels. However, the suppression of such common filters is not high enough (20-40 dB) to protect a quantum channel from neighboring classical states of light. If such a fiber link includes an amplifier, a quantum channel in the C-band will also be classically amplified which destroys its quantum state (no cloning theorem). From these considerations, transmitting the quantum channel in the O-band (taking losses into account) and classical data in the C-band seems the best solution.

To establish a quantum network, quantum nodes like single trapped atoms or ions, emitting in the visible or near infrared spectral region, have to be interconnected via photons. To this end, bridging the gap between low loss telecom wavelengths for long-range communication and the atomic wavelengths quantum frequency conversion (QFC) is necessary [15–17]. In the present experiment we produce frequency-degenerate photon pairs, generated by spontaneous parametric down conversion (SPDC), resonant with an atomic transition of $^{40}Ca^{+}$ at 854 nm. One of these photons is frequency converted to the telecom O-band. Its partner photon triggers a telecom C-band laser pulse which is overlapped with the converted photon and transmitted through a long single mode fiber. This means we here multiplex a quantum state of light at a wavelength in the telecom O-band with a coherent light field in the telecom C-band. We measure time correlations between the laser pulse and the converted photon at the fiber output, which arise from the original non-classical time correlation of the SPDC pair, maintained along frequency conversion, multiplexing and fiber transmission. This technique is also a proof of principle for all-optical distribution of a signal for heralding single photons.

FIBER CHARACTERIZATION

To examine the different properties of fibers in the O- and C-band in a preliminary experiment, we use correlated photon pairs in each of these bands. For this purpose, we pump a lithium niobate waveguide [18] at a wavelength of 708 nm to generate SPDC photons at 1535 nm and 1313 nm with sinc^2-shaped spectrum and a bandwidth of approximately 870 GHz (FWHM), respectively (details about SPDC in this particular device can be found in [18]). Both photons are sent through long single mode fibers (SMF-28e) before separating them with a wavelength division multiplexer (WDM). Each output of the WDM is connected to a single photon detector. In the post processing of the data we correlate the arrival times of the photons to measure the coincidences between O-band and C-band photons. The fiber has a different refractive index in the O- and C-band and thus the delay between the photons will depend on the length of the fiber. Hence the position of the coincidence peak will move. The result is shown in Fig. 1. As we used the same measurement time for all fiber lengths the total number of coincidences reduces due to losses. Additionally, due to the broadening the coincidences are spread over a larger number of time bins in the graph. Both effects result in an increased measurement uncertainty and reduced signal to background ratio, assuming a square root error model for the number of coincidences. This becomes visible in the broadening of the curves in the figure. We attribute the side peaks visible for fiber lengths above 20 km to reflections in the optical path. Furthermore, even the individual spectral components of each photon will experience different phase velocities leading to pulse broadening. The dispersion minimum of SMF-28 fibers is in the telecom O-band ($1310 < \lambda_0 < 1324$ nm, [19]). Hence we expect negligible pulse broadening there but the temporal shape of the C-band photon will significantly broaden due to dispersion. The results of the correlation measurement show that the delay between the O-band and C-band photons increases by 1.861 ± 0.004 ns/km. This value was measured at the peak positions and thus holds for every pulse-pair with 1535 nm and 1313 nm central wavelength. With the help of the effective group refractive indices of the optical fiber given in the data sheet [19] ($n_{1310} = 1.4676$, $n_{1550} = 1.4682$) we estimate a dispersion of 2 ns/km, in agreement with our experimental findings. For the pulse broadening of the C-band photons we find a value of 108 ± 0.8 ps/km which depends on the particular spectral shape. Again we can estimate a value from the parameters given in the data sheet [19]. The dispersion is given as ≤ 18.0 ps/(nm·km). A FWHM of 870 GHz corresponds to a spectral bandwidth of 7 nm, resulting is a dispersion of ≤ 126 ps/km. This is compatible with our measurement results.

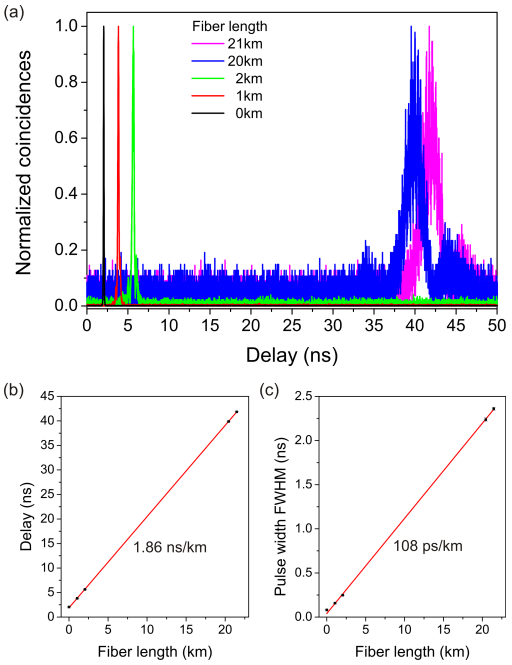

FIG. 1. Dispersion effects in the telecom fiber. a) shows correlation measurements between O-band and C-band photon pairs sent through different fibers. b) shows the shift of the coincidence peak and c) the broadening of this peak for the different fibers. The red solid lines in b) and c) are linear fits to the experimental data.

In practical realizations such effects can hamper the applicability. In internet communication the link between two nodes can be reconfigured on demand to reduce data traffic in certain channels and optimize speed and workload. Hence the optical distance between two nodes might change. For the idea of multiplexing quantum and classical channels this means the delay between these data packets might also change. There exist techniques to synchronize measurements which were referenced to independent clocks via the time-correlation of photon pairs [20]. A similar algorithm could be implemented here to track the correlation signal.

QUANTUM AND CLASSICAL SIGNAL IN A SINGLE FIBER

To demonstrate the multiplexing of two optical signals in a single fiber (SMF-28e), we implemented the experiment described in the following and illustrated in Fig. 2.

We use spontaneous parametric down conversion (SPDC) to generate photon pairs at 854 nm. This source

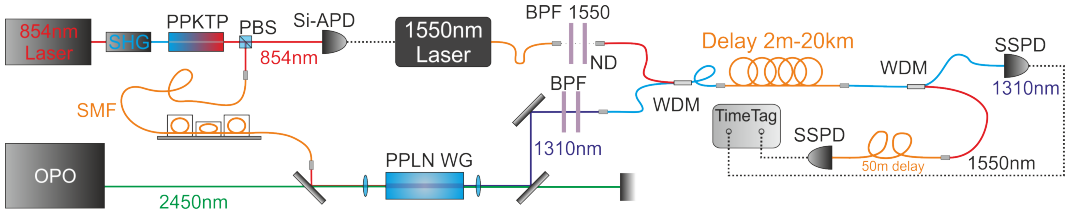

FIG. 2. Experimental setup for correlation measurements between converted photons and an optical clock signal. For abbreviations see text.

has been described earlier in more detail [21, 22] where it has been used to herald the absorption of a single-photon by a single trapped ion. It consists of a diode laser system at 854 nm which is actively stabilized to an atomic transition in calcium ($^{40}Ca^+$, $3^2D_{5/2} \leftrightarrow 4^2P_{3/2}$). The second harmonic (SHG) of this laser field serves as pump field for the SPDC process. This allows to generate frequency-degenerate photons resonant with the transition in Ca^+. The down conversion is realized via type-II phase matching conditions in a 2 cm long periodically poled KTP (PPKTP) crystal. The photons are thus polarization entangled. However, for the experiments reported here this kind of entanglement is not used and we employ a polarizing beam splitter (PBS) to effectively separate the signal and idler photons. One photon serves as a herald, which is detected by a silicon avalanche photon detector (Si-APD, Perkin Elmer SPCM-AQR-14, 30 % detection efficiency at 854 nm), while its partner photon is sent to the frequency converter setup. For frequency conversion we make use of difference frequency generation in a periodically poled lithium niobate ridge waveguide (similar to the device described in [16]). The conversion from $\lambda_s = 854$ nm to the telecommunications O-band around $\lambda_i = 1310$ nm is stimulated by a strong coherent pump field at a wavelength of $\lambda_p = 2453$ nm ($1/\lambda_s - 1/\lambda_p = 1/\lambda_i$). This pump field is generated by a continuous wave optical parametric oscillator (OPO). From calibration measurements we determine the overall conversion efficiency to approximately 8 % (including coupling of signal photons to the waveguide and telecom photons to the output fiber). Finally, we use superconducting single photon detectors (SSPD, Single Quantum EOS X10) for counting the telecom photons (detection efficiency of 25 % at 1310 nm). Although the efficiency of frequency conversion is only 8 % here, the overall transmission efficiency (including conversion and fiber transmission losses) benefits from the small fiber losses in the O-band (measured as 0.25 dB/km at 1310 nm, compared to approx. 2 dB/km at 854 nm) and equals the transmission efficiency of the unconverted photons at a fiber length of 6.5 km. After 20 km of fiber the advantage of the conversion scheme amounts to 24 dB. These numbers illustrate that low-loss transmission of quantum states through fibers benefits from QFC.

To multiplex classical and quantum states of light in a single fiber, we connect the heralding detector (Si-APD) to a diode laser (Thorlabs LPSC-1550-DC) emitting at 1550 nm in the telecom C-band. In detail the diode was biased with a DC current of 11 mA and the TTL-pulses were added via a bias-T and a 50 Ohm load resistor. This is enough to drive the diode above threshold (36 mA). The bias current reduces fluctuations of the pulse shape without finally introducing excess noise by continuous photons. The shape of the generated optical pulse (Fig. 3c) follows the electrical current. The laser pulse is transmitted through 1550 nm bandpass-filters (BPF, 20 nm FWHM) to suppress noise at other telecom wavelengths, generated by the laser. Then the pulses are sent to the lab where the converter is hosted. There, the laser pulses are combined with the converted photons via a WDM as shown in Fig. 2. After combination, both optical fields travel in the same delay fiber which can be set to various lengths between 2 m and 20 km. After this fiber link both fields are again separated by a single WDM. These WDMs (Thorlabs WD202B-FC) have a minimal isolation of 16 dB between the two bands. We first performed the correlation measurement with non-attenuated laser pulses and additional filters before the single photon detector at the O-band. In this case we were able to detect the C-band laser pulses with a standard photodiode (Thorlabs DET10C), thus proving that single photon sensitivity is not necessary in the clock channel. Unfortunately, the background in the single-photon O-band channel drastically increased due to channel cross-talk. With this configuration we were not able to clearly prove the preservation of the temporal correlation between the single photons and the laser pulses. The experimental setup could be optimized by including narrowband filters (e.g. fiber Bragg gratings) and WDMs with higher isolation. A similar result was observed in a recent paper where Raman scattering of the strong pulses was identified as main noise source [13].

One way to reduce this noise is to reduce the power of the laser pulses and use detectors with higher sensitivity. Superconducting single photon detectors are a current state-of-the art technology to register single photons. Their advantage is a low timing jitter in the order of 50 ps and high detection efficiency at telecom wavelengths. As

we already use such a device for the O-band channel the system complexity only marginally increases by adding a second device for the C-band channel. To observe the temporal correlations between O-band and C-band signals we thus reduce the power of the C-band pulses by adding neutral density filters and connect both output channels to the SSPDs, as illustrated in Fig. 2. The C-band channel has an additional delay of 50 m of fiber to reduce cross-talk effects in detection. In a preparatory measurement the rate of herald events was measured directly at the Si-APD. Then the laser pulses were attenuated by six orders of magnitude which, for the heralding channel, resulted in a comparable count rate on the SSPD as on the Si-APD before. We collect the detection events on both SSPD in a list of time-stamps using a fast counting electronics (Roithner Laser TTM8000) and correlate both later. For comparison a background measurement was performed by blocking the input of 854 nm photons in the converter and repeating the measurements with the same settings (red curves in Fig. 3). When the laser pulses arrive at the WDM the major part is directed to the C-band output port. However, a small fraction of the pulse (given by the WDM isolation) will also be directed to the O-band port. As the coherent pulse consists of many photons this leakage results in a coincidence detection on both detectors. The shape of this coincidence peak is given by the auto-correlation of the laser pulse and the position of the peak is given by the difference in optical delay between the WDM and the individual detectors. The background measurement makes this effect visible as the true single photon signal is blocked. Furthermore, we expect a very low constant noise floor by accidental coincidences between telecom O-band noise photons generated in the converter and C-band spontaneous emission of the laser, as well as detector dark counts in both channels. The laser pulses have a rectangular shape of 30 ns width (see Fig. 3c). Hence we expect a triangular auto-correlation with a width of 60 ns at the base. This corresponds well with the experimental width of 62 ns. The results for simultaneous transmission of classical and quantum signals are shown as gray bars in Fig. 3(a,b) for the shortest and longest available fiber lengths, respectively. In both examples we can identify two coincidence peaks. We inserted an additional 50 m delay fiber between the two SSPD channels (measured to introduce 244 ns delay). Hence we can identify the peak around 240 ns to stem from the fraction of the C-band laser pulse leaking into the O-band detection channel. This is proved by the background coincidence rate (red lines in Fig. 3) which shows that this peak is completely independent of the frequency converted photons. In contrast, the neighboring peak (gray shaded area) stems from the correlation between the laser pulses and the converted single photons. The center of mass of this peak shifts by 43 ns which is comparable to the shift expected from the earlier results (37.2 ns for 20 km, see Fig. 1). For the correlation signal of interest we expect a convolution between the short photon pulse (coherence time 5 ps) and the laser pulse (30 ns). The measured width at the base of the 20 km delayed pulse is 34 ns, corresponding well with the estimated value (30 ns + 20 km·108 ps/km = 32 ns). We can attribute the modulation of the pulse height to saturation and dead-time effects in the detectors. The coherent laser pulse consists of more than one photon on average which means that possibly more than one detection event can be triggered by a single pulse on the SSPD. In particular, the dead time of the SSPD is around 10 ns which is shorter than the pulse width, giving rise to the three-fold peak structure of the 30 ns long coincidence peak.

An effective separation of the signal of interest and the background is possible by gated detection, where the position and width of the gate window are adapted to position and shape of the signal coincidence peak.

CONCLUSION

To summarize the results, we have shown a basic experiment demonstrating a way to multiplex classical and quantum channels in a single fiber. We demonstrated the correlation of the SPDC photons by transmitting the timing information by an optical clock pulse in the telcom C-band. Moreover, we used quantum frequency conversion to the telecom O-band to tackle the high transmission losses of quantum-memory compatible photons. Both QFC and mapping of the detection event to a laser pulse, preserve the time correlation of the original 854 nm partner photons. This is an important proof-of-principle demonstration for distribution of quantum information using existing fiber network infrastructure.

Regarding a practical application, we should use gated detection and choose the gate width and position to cut out the coincidence peak with the true signal only, thereby discarding the detection channel cross-talk effects we observed. For fibers with several kilometers of length the delay is large enough to make this feasible. The laser pulses used in this proof of principle demonstration were generated by direct electrical connection of the APD to the laser. A further improvement is to use much shorter laser pulses that decrease timing jitter as well as reduce dead time effects in detection. Together with the gating this would decrease noise background. As pointed out in a recent publication temporal gating combined with spectral filtering makes multiplexing of a quantum channel and a standard communication channel in a single fiber feasible [13]. Those improvements can also be applied to our scheme.

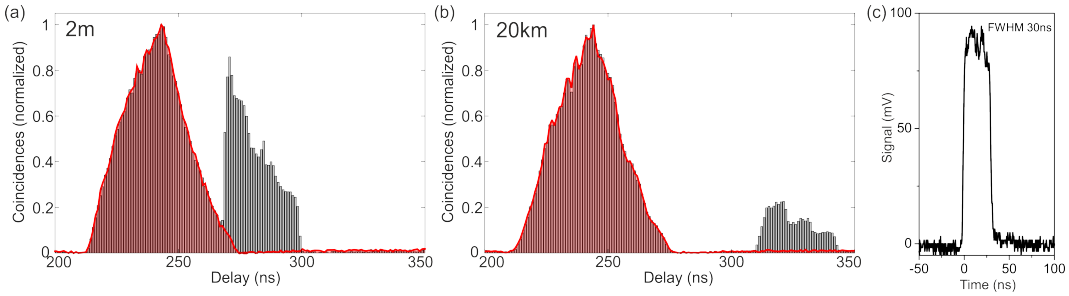

FIG. 3. Converted single photons at telecom O-band and laser herald pulses in the telecom C-band multiplexed in a single fiber. a) shows the results for 2 m of delay, as reference, and b) shows the long-range measurement over 20 km. The red solid lines show measurements of the background, the gray bars show the measurement results including O-band single photons. The red shaded areas are a guide for the eye and indicate the cross-talk coincidences of the laser pulses. Detections in the O-band channel were used as start and in the C-band channel as stop triggers for the correlation measurements. c) shows a measurement of the laser pulse intensity with a standard photo diode and an oscilloscope (2 m fiber delay).

ACKNOWLEDGMENTS

The work was funded by the German Federal Ministry of Science and Education (BMBF) within the projects "Q.com-Q" (contract No. 16KIS0127). J. Brito acknowledges support by CONICYT.

[1] H. Shibata, T. Honjo, and K. Shimizu, "Quantum key distribution over a 72 dB channel loss using ultralow dark count superconducting single-photon detectors," Opt. Lett. **39**, 5078-5081 (2014).

[2] T. Inagaki, N. Matsuda, O. Tadanaga, M. Asobe, and H. Takesue, "Entanglement distribution over 300 km of fiber," Opt. Express **21**, 23241-23249 (2013).

[3] H. Takesue, S. Nam, Q. Zhang, R. H. Hadfield, T. Honjo, K. Tamaki, and Y. Yamamoto, "Quantum key distribution over a 40-dB channel loss using superconducting single-photon detectors," Nature Phot. **1**, 343-348 (2007).

[4] M. Peev, C. Pacher, R. Alleaume, C. Barreiro, J. Bouda, W. Boxleitner, T. Debuisschert, E. Diamanti, M. Dianati, J. F. Dynes, S. Fasel, S. Fossier, M. Fürst, J.-D. Gautier, O. Gay, N. Gisin, P. Grangier, A. Happe, Y. Hasani, M. Hentschel, H. Hübel, G. Humer, T. Länger, M. Legre, R. Lieger, J. Lodewyck, T. Lorünser, N. Lütkenhaus, A. Marhold, T. Matyus, O. Maurhart, L. Monat, S. Nauerth, J.-B. Page, A. Poppe, E. Querasser, G. Ribordy, S. Robyr, L. Salvail, A. W. Sharpe, A. J. Shields, D. Stucki, M. Suda, C. Tamas, T. Themel, R. T. Thew, Y. Thoma, A. Treiber, P. Trinkler, R. Tualle-Brouri, F. Vannel, N. Walenta, H. Weier, H. Weinfurter, I. Wimberger, Z. L. Yuan, H. Zbinden and A. Zeilinger, "The SECOQC quantum key distribution network in Vienna," New J. Phys. **11**, 075001 (2009).

[5] M. Sasaki, M. Fujiwara, H. Ishizuka, W. Klaus, K. Wakui, M. Takeoka, S. Miki, T. Yamashita, Z. Wang, A. Tanaka, K. Yoshino, Y. Nambu, S. Takahashi, A. Tajima, A. Tomita, T. Domeki, T. Hasegawa, Y. Sakai, H. Kobayashi, T. Asai, K. Shimizu, T. Tokura, T. Tsurumaru, M. Matsui, T. Honjo, K. Tamaki, H. Takesue, Y. Tokura, J. F. Dynes, A. R. Dixon, A. W. Sharpe, Z. L. Yuan, A. J. Shields, S. Uchikoga, M. Legre, S. Robyr, P. Trinkler, L. Monat, J.-B. Page, G. Ribordy, A. Poppe, A. Allacher, O. Maurhart, T. Länger, M. Peev, and A. Zeilinger, "Field test of quantum key distribution in the Tokyo QKD Network," Opt. Express **19**, 10387-10409 (2011).

[6] A. Rubenok, J. A. Slater, P. Chan, I. Lucio-Martinez, and W. Tittel, "Real-World Two-Photon Interference and Proof-of-Principle Quantum Key Distribution Immune to Detector Attacks," Phys. Rev. Lett. **111**, 130501 (2013).

[7] W. Tittel, J. Brendel, H. Zbinden, and N. Gisin, "Violation of Bell Inequalities by Photons More Than 10 km Apart," Phys. Rev. Lett. **81** 3563-3566 (1998).

[8] I. Marcikic, H. de Riedmatten, W. Tittel, H. Zbinden, and N. Gisin, "Long-distance teleportation of qubits at telecommunication wavelengths," Nature **421**, 509-513 (2003).

[9] C. H. Bennett, and G. Brassard in Int. Conf. Computers, Systems & Signal Processing, Bangalore 175-179 (1984).

[10] P.D. Townsend, "Simultaneous quantum cryptographic key distribution and conventional data transmission over installed fibre using wavelength-division multiplexing," Electr. Lett. **33**, 188-190 (1997).

[11] T. E. Chapuran, P. Toliver, N. A. Peters, J. Jackel, M. S. Goodman, R. J. Runser, S. R. McNown, N. Dallmann, R. J. Hughes, K. P. McCabe, J. E. Nordholt, C. G. Peterson, K. T. Tyagi, L. Mercer, and H. Dardy, "Optical networking for quantum key distribution and quantum communications," New J. Phys. **11**, 105001 (2009).

[12] M. A. Hall, J. B. Altepeter, and P. Kumar, "Drop-in compatible entanglement for optical-fiber networks," Opt. Express **17**, 14558-14566 (2009).

[13] S. Aleksic, F. Hipp, D. Winkler, A. Poppe, B. Schrenk, and G. Franzl, "Perspectives and limitations of QKD integration in metropolitan area networks," Opt. Express **23**, 10359-10373 (2015).

[14] International Telecommunication Union, "Spectral grids for WDM applications: DWDM frequency grid, ITU-T G.694.1", version 02/2012.

[15] Z. Y. Ou, "Efficient conversion between photons and between photon and atom by stimulated emission," Phys. Rev. A **78**, 023819 (2008).

[16] S. Zaske, A. Lenhard, C. A. Keßler, J. Kettler, C. Hepp, C. Arend, R. Albrecht, W.-M. Schulz, M. Jetter, P. Michler, and C. Becher, "Visible-to-Telecom Quantum Frequency Conversion of Light from a Single Quantum Emitter," Phys. Rev. Lett. **109**, 147404 (2012).

[17] S. Blum, G. A. Olivares-Renteria, C. Ottaviani, C. Becher, and G. Morigi, "Single-photon frequency conversion in nonlinear crystals," Phys. Rev. A **88**, 053807 (2013).

[18] M. Bock, A. Lenhard, and C. Becher, Manuscript in preparation, (2015).

[19] Corning SMF-28e+ Optical Fiber with NexCor Technology - Product Information, Document PI1463, December 2007, Corning Inc.

[20] C. Ho, A. Lamas-Linares, and C. Kurtsiefer, "Clock synchronization by remote detection of correlated photon pairs," New J. Phys. **11**, 045011 (2009).

[21] N. Piro, A. Haase, M. W. Mitchell, and J. Eschner, "An entangled photon source for resonant single-photon-single-atom interaction," J. Phys. B: At. Mol. Opt. Phys. **42**, 114002 (2009) .

[22] N. Piro, F. Rohde, C. Schuck, M. Almendros, J. Huwer, J. Ghosh, A. Haase, M. Hennrich, F. Dubin, J. Eschner, "Heralded single-photon absorption by a single atom", Nat. Phys. **7**, 17-20 (2010).

B.3. OPO source photon-to-atom interaction

This paper presents results of the OPO source characterization and interaction experiments with the calcium ion as discussed in chapter IV. The respective results are published [74].

Telecom-heralded single photon absorption by a single atom

Andreas Lenhard, Matthias Bock, and Christoph Becher*
Quantenoptik, Fachrichtung 7.2, Universität des Saarlandes, Campus E2.6, 66123 Saarbrücken, Germany

Stephan Kucera, José Brito, Pascal Eich, Philipp Müller, and Jürgen Eschner†
Quantenphotonik, Fachrichtung 7.2, Universität des Saarlandes, Campus E2.6, 66123 Saarbrücken, Germany

We present, characterize, and apply the architecture of a photonic quantum interface between the near infrared and telecom spectral regions. A singly resonant optical parametric oscillator (OPO) operated below threshold, in combination with external filters, generates high-rate ($> 2.5 \cdot 10^6$ s^{-1}) narrowband photon pairs (~ 7 MHz bandwidth); the signal photons are tuned to resonance with an atomic transition in Ca^+, while the idler photons are at telecom wavelength. Interface operation is demonstrated through high-rate absorption of single photons by a single trapped ion (~ 670 s^{-1}), heralded by coincident telecom photons.

I. INTRODUCTION

The vision of a quantum network integrates the concepts of classical communication with the potentialities of quantum physics, thereby opening up qualitatively new opportunities for data transmission and processing [1, 2]. For long-range information broadcasting in quantum networks, the use of telecom fiber-compatible photons is highly desirable, due to the particular sensitivity of quantum information to loss. On the other hand, quantum information storage and processing makes use of optical transitions in atomic systems that often lie in the near-infrared (NIR) region. In order to interface atom-based stationary quantum bits with flying qubits realized by telecom photons, quantum frequency conversion techniques between the respective wavelengths may be used [3]. Another attractive approach, as presented in the following, is to interface the two spectral regions by (possibly entangled) photon pairs generated via spontaneous parametric down conversion (SPDC) [4–6].

Sources for photon pairs based on SPDC are available at telecom [7, 8] and near infrared wavelengths [9–13], and also based on integrated optics technology [7, 14, 15]. The SPDC process, however, is intrinsically too broadband (∼100 GHz) for compatibility with atomic transitions (∼10 MHz). Spectral shaping may either be achieved by external filtering [10, 16], or by a resonant enhancement approach: Here one places the SPDC medium inside an optical cavity where a pump photon spontaneously decays into signal and idler photons of which at least one is resonant with a cavity mode. The latter scheme corresponds to an optical parametric oscillator (OPO) operated below threshold and was first demonstrated by Ou and coworkers [17]. OPO-based photon pair sources have been realized with bandwidths in the MHz range [9, 11, 12, 18, 19], and entangled photons compatible with atomic transitions in Cs [11] or Rb [9, 12] and at telecom wavelengths [14] have been generated. Most of these sources generate frequency degenerate photon pairs in doubly resonant cavities; spectral filtering of a non-degenerate OPO was introduced recently to generate photon pairs compatible with quantum memories and telecom networks [6] and to demonstrate mapping of these photons to a solid-state quantum memory [20]. Whereas OPO-based photon pair sources generally offer spectral tunability, fixed-frequency photon pairs including telecom wavelengths may also be obtained from atomic cascade transitions [21].

On the atomic side, trapped Ca^+-ions provide a paradigmatic platform for implementing fundamental components of quantum information processing [22]. In the context of quantum networks, recent experiments showed the heralded absorption of single photons from a SPDC source by a single Ca^+ ion [23], the manifestation of photonic entanglement in the absorption process [24], bidirectional atom-photon state conversion [25–27], and the interconnection of ions via photonic channels [28–30]. Here we report the architecture of a photonic quantum interface based on an OPO source of non-degenerate photon pairs that bridges the NIR and telecom spectral regions and enables single-photon absorption in a Ca^+ ion heralded by a photon in the telecom range.

II. DEVICE CHARACTERIZATION

The optical parametric oscillator (OPO) is based on a design originally developed for experiments in quantum frequency conversion at telecom wavelengths [31]. Its heart is a 30 mm long crystal of periodically poled, MgO-doped stoichiometric lithium tantalate, whose end facets are cut under 2° angle and anti-reflection coated for pump, signal, and idler wavelengths. Its pump source is a frequency-doubled solid state laser system (532 nm, max. 10 W). Six equally spaced poling periods between $\Lambda_1 = 8.1$ μm and $\Lambda_6 = 8.6$ μm allow for OPO operation anywhere between 1202 nm and 1564 nm idler wavelength and 806–954 nm signal wavelength. The crystal is placed in a four-mirror bow-tie type ring cavity [32]. Three mirrors are coated for high reflectivity at 790–995 nm and

* christoph.becher@physik.uni-saarland.de
† juergen.eschner@physik.uni-saarland.de

high transmission at the pump and idler wavelengths; an output-coupling mirror with 97 % reflectivity at the signal wavelength allows us to operate the OPO below threshold (2.8 W) as a SPDC-source of individual signal and idler photon pairs. For the experiments reported here we use 300 mW pump power, as a trade-off between high pair generation rate and low multi-pair probability. The OPO covers the telecom O-, E-, S- and C-band and simultaneously the NIR region where transitions of atoms and atom-like systems such as Ca^+ (854 nm), Cs (894 nm), InAs/GaAs quantum dots (900-940 nm) [33, 34], or solid state quantum memories (883 nm) [35] are found.

We expect the spectrum of the signal photons to be a convolution of the Airy-function of the cavity with the phase matching function of the OPO crystal. While the free spectral range of the cavity, ~ 1 GHz, is not resolved by our grating spectrometers (resolution: 20 GHz), it is reflected in the temporal shape of the photon wave packet: if a photon pair is generated in the nonlinear crystal, the idler photon will leave the cavity immediately while the signal photon is likely to be reflected at the output coupling mirror. As shown in Fig. 1a, the temporal correlation between idler and signal photon detection reveals the cavity round-trip and the cavity ring-down. An exponential fit to the envelope yields a cavity decay time of 22.7 ± 3.6 ns, corresponding to a linewidth of 7.2 ± 1.1 MHz. The well-separated peaks are spaced by the cavity round-trip time of 939 ± 4 ps. The width of these lines is resolution-limited due to detection jitter in the APDs.

To gain more insight into the photons' spectral properties we measure the first-order coherence function of the signal field using a Michelson interferometer. Figure 1b shows the interferogram (visibility as a function of delay) around zero delay. In the long-range scan (main graph) peaks appear with a spacing of 942 ± 1 ps, confirming the previous result for the round trip time of the OPO cavity. The inset shows a high-resolution scan; a two-sided exponential fit yields 1.4 ps coherence time, which corresponds well to the measured spectral width of 275 GHz (FWHM). This width is mainly determined by the phase matching conditions of the nonlinear process. The contrast and the comb structure visible in the temporal and coherence function are in good agreement with the theoretical prediction [36].

According to these results, the width of a single mode from the comb-like spectrum is 7.2 MHz, already compatible with atomic resonances. To reduce the background from other, non-resonant modes, the resonant single line is extracted by narrowband filtering of the coincident idler photon that serves as a herald for its atom-resonant partner [6, 10–12, 15, 18]. As we target a transition in Ca^+ at 854 nm, the corresponding idler wavelength is at 1411 nm, within the standard telecom E-band. We use a narrowband tunable filter system (AOS GmbH) based on two cascaded fiber Bragg gratings (FBG). This device has a Lorentzian transmission window of 1.56 GHz

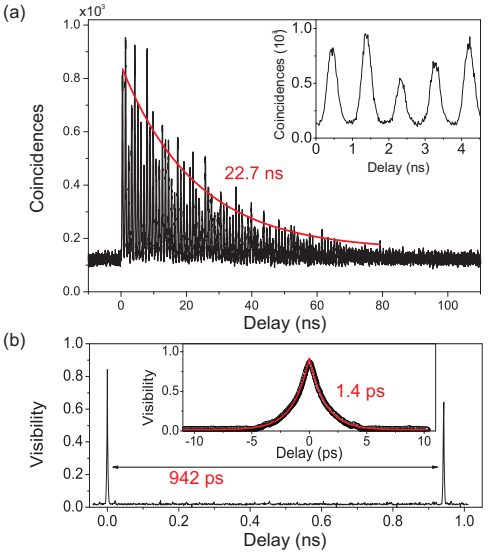

FIG. 1. (Color online) Temporal characteristics of the photon pairs: a) Time correlation between the heralding idler and the signal photons. The idler photon is detected by an InGaAs avalanche photo diode (APD) and used as a start trigger for time-tagged single photon counting of the signal photon which is detected by a Si-APD. The inset is a close-up of the data. b) First order coherence function of the signal photons. Inset: high resolution scan of the peak at zero delay, with an exponential fit function. No noise subtraction is applied. The maximum visibility of 0.904 ± 0.004 is mainly limited by dark counts. The detection rate in both plots was $1.7 \cdot 10^4$ cts/s.

(FWHM) and a rejection band exceeding by far the total width of the idler spectrum. The filter system has 20 % maximum transmission, including coupling loss between the OPO and a single mode fiber. As the filter width exceeds the OPO free spectral range, neighbouring modes are also partially transmitted and will contribute a background of heralds that are not coincident with a resonant photon. From numerical calculations we expect a signal to background ratio around 1.

To characterize the narrowband photon pairs we also filter the signal photons down to a single mode. The filter system is described in [10, 16]. It consists of two cascaded Fabry-Pérot cavities with different free spectral ranges resulting in a transmission bandwidth of 22 MHz, tailored to match the linewidth of the $D_{5/2}$–$P_{3/2}$ transition of the $^{40}Ca^+$-ion at 854 nm. Both filter cavities are actively stabilized to a laser which is resonant with the atomic transition. Transmitted photons are detected by a Si-APD. Thus this filtering system serves to emulate the calcium transition of interest by detecting only photons from the resonant single mode of the OPO spectrum. The result of the correlation measurement between filtered idler and signal photons is shown in Fig. 2. The data is well de-

scribed by a convolution of two exponential decays, as shown. The first time constant is the filter cavity decay time, 7.0 ns, while the second time constant corresponds to the width of the photon wave packet, 22.7 ns, as determined above. Since the loss factors between the OPO and the two detectors were not fully characterized in this measurement, we defer the analysis for the generated pair rate until the next section.

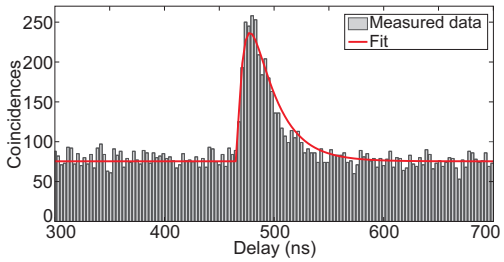

FIG. 2. (Color online) Correlation measurement of narrowband idler (filtered by FBG, start) and signal (cavity filter, stop) photons. Time bin size is 3 ns, total measurement time is 30 minutes.

III. HERALDED ABSORPTION

A sketch of the full experimental setup is displayed in Fig. 3. The OPO and the ion trap are located in different labs connected via a 90 m single mode fiber (SMF) link. At its output, a fiber beam splitter guides half of the 854 nm idler photons to the ion and the other half to the cavity filtering system described above. The detection rate behind the filter is utilized in a feedback loop to stabilize the center frequency of the OPO against fluctuations and drifts due to environmental conditions. The photons sent to the ion do not pass any filter.

The calcium ion is prepared for single-photon absorption in the meta-stable $D_{5/2}$ fine-structure manifold (lifetime 1.17 s), see Fig. 4. Absorption of an 854 nm photon on the $D_{5/2}$ to $P_{3/2}$ transition, followed by spontaneous decay to $S_{1/2}$, induces a quantum jump of the ion signalled by the onset of atomic fluorescence (at 397 nm

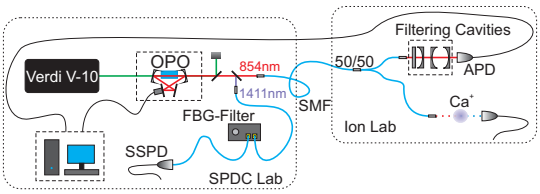

FIG. 3. (Color online) Schematic drawing of the experimental setup. The two labs (dashed boxes) are separated by 90 m. For details see text.

wavelength, see [23]). Single-photon absorption is detected with about 94% efficiency, set by the branching fraction for decay of the $P_{3/2}$ level to $S_{1/2}$.

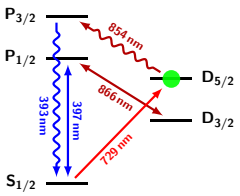

FIG. 4. (Color online) Relevant energy levels and transition wavelengths of $^{40}Ca^{+}$. The green dot denotes the initial state for the single-photon interaction.

In detail, we repeat the following experimental sequence with a rate of 140 Hz: after an initial Doppler-cooling period of 200 μs, the ion is optically pumped during 60 μs into the $|S_{1/2}, m = -\frac{1}{2}\rangle$ Zeeman sub-level of the ground state. Afterwards, a 2.2 μs long narrowband laser pulse at 729 nm transfers population to the $|D_{5/2}, m = -\frac{5}{2}\rangle$ state. Three additional pulses clean out any remaining $S_{1/2}$ population to other $D_{5/2}$ sub-levels; in total, preparation in $D_{5/2}$ happens in 11 μs with measured 99.99(1) % probability (see Appendix B). Then the cooling lasers at 397 nm and 866 nm, driving the transitions $S_{1/2}$–$P_{1/2}$ and $D_{3/2}$–$P_{1/2}$, respectively, are switched on, and the ion is exposed to the photons from the OPO for 7 ms. Ion-photon coupling is optimised by the use of a high-aperture laser objective (HALO). The fluorescence at 397 nm, whose onset serves as evidence for the absorption, is collected by two HALOs and detected by two photomultiplier tubes (PMT) with 1.5% overall efficiency, resulting in 4.3 μs temporal resolution for the detection of a quantum jump. After the interaction time the sequence starts again. The probability for spontaneous decay from $D_{5/2}$ to $S_{1/2}$ during the interaction time is 0.6 %.

In parallel the telecom idler photons transmitted by the narrowband FBG filter are detected by a superconducting single photon detector (SSPD). Both the 397 nm fluorescence photons and the detected telecom heralds are recorded with time-tagged photon counting electronics. The quantum jumps are found in the post-processing of the data [37] and then correlated with the detection times of the telecom photons. The result is shown in Fig. 5. For the coincidence peak around zero delay we find a signal-to-noise ratio of 6.7. The result clearly manifests the temporal correlation between the quantum jumps and the telecom photons, i.e., the heralded absorption of single OPO photons by the single ion. The delay-independent background is produced by accidental coincident or time-shifted detection of a telecom photon and an uncorrelated quantum jump. Its high value is a result of the large loss factors between generated photon pairs and detection events. A comprehensive quantitative analysis is provided in Appendix A. Dark counts play a

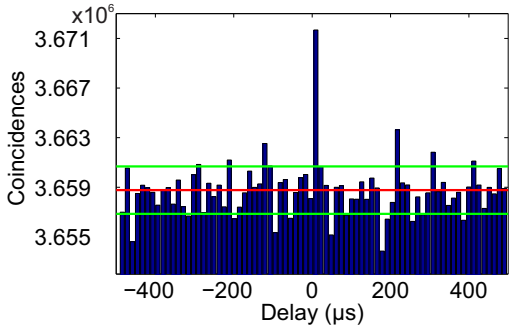

FIG. 5. (Color online) Coincidences of quantum jumps and filtered telecom photons. The red line indicates the background level, and the green lines the Poissonian noise interval of the background. Time bin size is 13 μs, total measurement time is 310 min.

negligible role. From the observed peak values of the absorption rate, 671(46) s^{-1}, and the detection rate on the Si-APD, 6,500 s^{-1}, and taking into account the known losses, we estimate the resonant pair generation rate of the OPO to be at least $2.5 \cdot 10^6$ s^{-1} of which 340,000 resonant photons/s are available in front of the ion trap for absorption. Divided by the OPO pump power this results in 8,400 pairs/(s·mW); this value exceeds the performance reported for other state-of-the-art OPO SPDC devices [6, 9, 11]. The absorption probability per resonant photon sent into the ion trap is $\sim 2 \cdot 10^{-3}$ and the absorption probability per telecom detection event is $6.6 \cdot 10^{-6}$. These probabilities are mainly limited by the numerical aperture of the collection lens and the oscillator strength of the $D_{5/2}$–$P_{3/2}$ transition. An analysis based on signal and idler detection rates confirms these numbers. Details are provided in Appendix A. Quantum information transfer to the ion becomes possible if, instead of quantum jump detection, the heralding method of [26] is used. Taking the $\sim$ 1% heralding probability from that work and our rate of 680 s^{-1} absorptions, and assuming that the telecom herald is detected with low loss, the expected qubit transfer rate is on the order of 10 s^{-1}.

IV. SINGLE PHOTON SPECTROSCOPY

To demonstrate interface operation with our photon pair source we use the narrowband photons from the OPO for spectroscopy of the atomic transition. In particular, we study how the lifetime of the metastable $D_{5/2}$ level is shortened by the single-photon excitation, compared to its value $\tau_{sp} = 1.17$ s in the absence of resonant photons. Controlled tuning of the OPO is effected by varying the center frequency of the cavity filters to which the OPO is stabilized via a side-of-fringe lock. We measure the effective lifetime $\tau_{eff}(\Delta)$ of the $D_{5/2}$ state vs. the detuning Δ as follows: the ion is prepared as described in the previous section, and the time between the preparation and the quantum jump (onset of fluorescence) is measured. The histogram of this time distribution is used for a Bayesian estimation of the decay probability, which is then fit by an exponential function yielding the effective lifetime, τ_{eff}. The absorption rate is derived as $R_{abs} = (\tau_{eff}^{-1} - \tau_{sp}^{-1})/0.94$, which corrects for spontaneous decay from $D_{5/2}$ to $S_{1/2}$ and for the fraction of undetected absorptions (6%) that lead to decay back to $D_{5/2}$. The result is shown in Fig. 6.

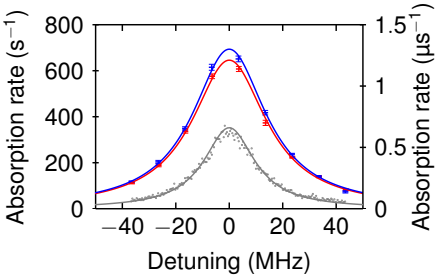

FIG. 6. (Color online) Spectroscopy of the atomic line with single photons from the OPO. Absorption rate as a function of OPO detuning. In order to compensate for frequency drifts of the OPO, individual data sets are recorded for detuning to higher (blue, left axis) and lower (red, left axis) frequencies; Lorentzian fits are shown. For comparison, a laser excitation spectrum is also shown (grey points and line, right axis).

From the two Lorentzian fits to the data we find a mean peak absorption rate $R_{abs} = 670(17)$ s^{-1}, and a mean linewidth of 33.6 ± 0.6 MHz (FWHM). Convoluting the natural line width, 23 MHz [38], with the photon linewidth of 7.2 ± 1.1 MHz and the 4 MHz residual frequency fluctuations of the stabilized OPO results in an expected Lorentzian width of 34.2 ± 1.1 MHz, in very good agreement with the experimental finding. For comparison, Fig. 6 also shows an absorption line measured with a narrowband diode laser; its width of 24.6 MHz is very close to the natural line width. The on-resonance single-photon absorption rate of 670 s^{-1} coincides well with the measurement from the heralded absorption. It is about three orders of magnitude larger than what has been reached before with Ca^+ [23, 24] and within the same order of magnitude as compared to recent experiments on single photon absorption by single atoms or ions [39–41].

V. SUMMARY AND CONCLUSION

In summary we presented an OPO-based, high-rate source of time-correlated, narrowband, widely tunable photon pairs interfacing the near infrared spectral region with the telecom bands. We demonstrated an essential

building block of quantum networks, the heralded absorption of a single photon by a single atom; most importantly, the heralding photon is at a telecom wavelength, enabling long-range heralding in fiber networks. About $2.5 \cdot 10^6$ s^{-1} resonant pairs are generated in 7 MHz bandwidth; they effect an absorption rate close to 700 s^{-1}. As the photon pairs produced here show energy-time entanglement (for details see Appendix C) they can be employed for quantum cryptography with unconditional security [42, 43] where the entanglement is preserved over large distances as one of the photons is within a low-loss, low-dispersion telecom band. The transfer of energy-time photonic entanglement to material qubits has been demonstrated before [35] such that we expect a similar quantum interfacing to the trapped-ion qubit to be feasible. Such a quantum interface operation requires strong reduction of the losses in the transmission channel between photon source and ion and better spectral filtering to reduce the background contributions. Both measures are within technical reach.

Appendix A: Derivation of photon pair rate

Here we explain in more detail the method to derive the generated photon pair rate from the heralded absorption measurement including coincidence detection between quantum jumps and telecom photons.

The OPO SPDC source produces photon pairs at a rate P, split in signal and idler mode. There is additional background noise generated which we account for by the rates $B_{1,2}$ (we hereby neglect background generated by the detectors in accordance with the experiment). Both signal and background photons suffer losses $\eta_{1,2}$ before being detected individually at detectors $D_{1,2}$. The factors $\eta_{1,2}$ include the detection efficiencies. The connection of these parameters is sketched in Fig. 7. We

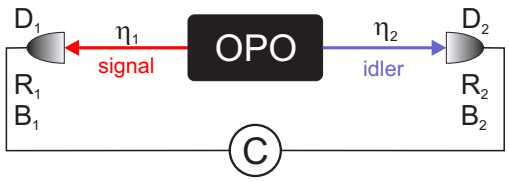

FIG. 7. (Color online) Schematic diagram of the setup indicating the definitions of rates and efficiencies. The index 1 denotes parameters at the signal wavelength branch (854 nm), while index 2 denotes idler wavelengths (1411 nm). For details see text.

can either detect singles-rates $R_{1,2}$ or measure the coincidence rate C between signal and idler arm. This scheme also holds for quantum jump detection at the trapped ion in one of the arms.

In the paper we aim at deriving the generated pair rate P and generated background rates $B_{1,2}$ from the measured single rates $R_{1,2}$ and coincidence rate C. Setting $\beta_{1,2} = B_{1,2}/P$, we identify the relations

$$R_{1,2} = (P + B_{1,2})\eta_{1,2} = P(1 + \beta_{1,2})\eta_{1,2} \tag{A1}$$

and

$$C = P\eta_1\eta_2 \tag{A2}$$

We use the measured $g^{(2)}$ function to derive C (total counts in the coincidence peak divided by the total measurement time T), as well as the background rate per bin, BG (average number of counts per bin of size Δt, divided by T). Consistency demands that $BG = R_1 R_2 \Delta t$.

From the measured values R_1, R_2, and C, we cannot derive all unknowns, but if we take known values for η_1 and β_1, then

$$P = \frac{R_1}{\eta_1(1 + \beta_1)} \tag{A3}$$

and

$$\eta_2 = \frac{C}{P\eta_1} \tag{A4}$$

and finally

$$1 + \beta_2 = \frac{R_2}{P\eta_2} \tag{A5}$$

We apply this to the quantum jumps-telecom coincidence data of Fig. 5 using subscripts 1 for the quantum jumps and 2 for the telecom SSPD counts. We measured

$$R_1 = 111 \text{ s}^{-1}$$

$$R_2 = 136,000 \text{ s}^{-1}$$

$$C = \frac{16,692}{310 \cdot 60 \text{ s}} = 0.90 \text{ s}^{-1}$$

and we suppose that we know the loss between OPO and ion (specified below), as well as the background at 854 nm, which we assume to be $B_1 = 0$.

The background coincidence rate expected from these numbers is $BG = R_1 R_2 \Delta t = 196$ s^{-1}, which in the total measurement time of 310 min corresponds to $3.65 \cdot 10^6$ background counts per bin, consistent with the value of $3.66 \cdot 10^6$, as observed in Fig. 5.

The calculation of P is not done directly from Eq. A3, because the ion is not immediately re-prepared after a quantum jump. This means further absorptions cannot be detected until the next preparation cycle. Instead we get P via the maximum observed absorption rate. In analogy to the spectroscopy measurement we generate a histogram of the time distribution of quantum jumps and use this data to calculate the absorption rate via the effective lifetime (the procedure is explained in more detail in [29]). This rate is $R_{\text{abs}} = 671(46)$ s^{-1}. The "dark time" after a quantum jump is equivalent to an additional

efficiency factor, $\eta_{\rm sat} = R_1/R_{\rm abs} = 0.165$, contributing to the loss on the ion side, which otherwise is given by

$$\eta_1 = \eta_{\rm SMF}\eta_{\rm fbs}\eta_{\rm ion}\eta_{\rm sat} = 4.4 \cdot 10^{-5} \qquad \text{(A6)}$$

with measured values $\eta_{\rm SMF} = 0.27$, $\eta_{\rm fbs} = 0.5$, and $\eta_{\rm ion} = 0.002$ for the fiber coupling and transmission loss between OPO and ion laboratory, the fiber beam splitter in front of the ion, and the absorption probability of the ion per arriving OPO photon, respectively.

From this we get the estimated pair rate

$$P = \frac{R_1}{\eta_1} = \frac{R_{\rm abs}}{\eta_{\rm SMF}\eta_{\rm fbs}\eta_{\rm ion}} = 2.52 \cdot 10^6 \text{ s}^{-1} \qquad \text{(A7)}$$

and the other parameters according to Eqs. (A4,A5) are

$$\eta_2 = 8.1 \cdot 10^{-3}$$

and finally

$$\beta_2 = 5.7$$

Regarding η_2 there are known contributions, the OPO to SSPD coupling and transmission loss $\eta_{\rm OPO-SSPD} = 0.2$ and the SSPD detection efficiency $\eta_{\rm SSPD} = 0.25$, such that there remains an unknown contribution

$$\eta_{\rm unknown} = \frac{\eta_2}{\eta_{\rm OPO-SSPD}\eta_{\rm SSPD}} = 0.16$$

We can identify several possible contributions to this unknown factor. First, the SSPDs show a strong polarization dependance of detection efficiency. For the non-optimal polarization, the efficiency drops down to 50% of the maximum efficiency, caused by the orientation of the meander structure of the superconducting nanowires with respect to the photon polarization. As this effect was not well characterized at the time the experiments were performed, the polarization was not optimized. Second, the maximum SSPD efficiency of 25% is specified by the manufacturer for the telecom O-band around 1310 nm. The efficiency definitely drops down for longer wavelengths but we do not have the ability to measure a reliable value. A third loss channel might be the fiber-fiber-couplers of the SSPD and the FBG, which depend strongly on the mechanical adjustment of the fibers. In a latter experiment we obtained an additional loss factor of up to 0.5 for the whole series of fiber couplers.

Multiplying the estimated pair rate P, Eq. A7, with the transmission loss $\eta_{\rm SMF}$ and $\eta_{\rm fbs}$ results in a rate of $\sim 340,000$ s^{-1} resonant photons available at the ion trap for experiments. This value is consistent with the results of the spectroscopy experiment, where we record about $8,000$ s^{-1} photons on the APD (with ~ 0.3 detection efficiency) after the filter cavities (with about 0.6 transmission and 0.13 coupling efficiency). Using an asymmetric rather than 50/50 beam splitter between ion and filter cavities would increase the rate of ion-resonant photons up to 2-fold.

Appendix B: Efficiency of ion state preparation

We here explain the efficiency of the state preparation of the ion into the $D_{5/2}$ level. Fig. 8 shows the laser pulses used for the preparation of the ion in the $D_{5/2}$ level. The efficiencies of the individual pulses were measured via fluorescence detection, using 500 repetitions: optical pumping into $|S_{1/2}, m = -\frac{1}{2}\rangle$ (pulse (1)) happens with 99.6(3) % efficiency, pulses (2), (3), (4), and (5) have 99.2(3) %, 98.2(6) %, 97.8(7) %, and 97.6(7) % transfer probability, respectively. From these numbers we calculate an overall preparation probability of 99.99(1) %. This value was confirmed in a fluorescence measurement with $n = 10^5$ preparation cycles in which $k = 5$ events of failed preparation were recorded.

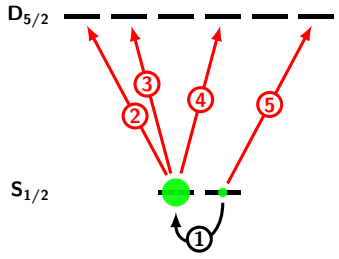

FIG. 8. (Color online) Excitation pulses for preparing the ion in the D5/2 level. Pulse (1) optically pumps the population into $|S_{1/2}, m = -\frac{1}{2}\rangle$; pulse (2) transfers it to $|D_{5/2}, m = -\frac{5}{2}\rangle$. Pulses (3) and (4) clear out the remaining population from $|S_{1/2}, m = -\frac{1}{2}\rangle$ by transferring it to $|D_{5/2}, m = -\frac{3}{2}\rangle$ and $|D_{5/2}, m = +\frac{1}{2}\rangle$, respectively, while pulse (5) empties $|S_{1/2}, m = +\frac{1}{2}\rangle$ to $|D_{5/2}, m = +\frac{5}{2}\rangle$. The efficiency of the procedure is explained in the text.

Appendix C: Energy-time entanglement of photon pairs

As discussed in the main text, the transfer of quantum information from a photon of the pair source to the ion is an interesting extension of our experiment. We propose to utilize the energy-time entanglement of the photons, which is an intrinsic property of the SPDC process. Accordingly, to confirm that our photons are in fact energy-time entangled, we perform a Franson-type [44] interference experiment. Such an experiment uses one interferometer for each of the photons where the interferometer path length difference needs to be larger than the photon's first-order coherence time. In our interference measurement the photons were not filtered, neither by the OPO cavity (which was blocked), nor by external spectral filters. The reason for this is that the filtered photons have such a long coherence time that interferometer delays of more than 10 m length would be required, leading to instability in the measurements. The

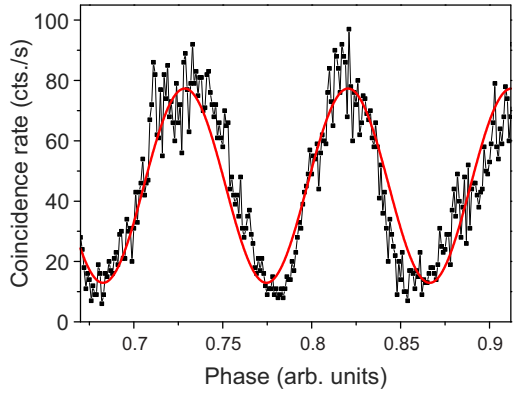

FIG. 9. (Color online) Franson interference experiment: signal-idler coincidence rate vs. phase of the Michelson interferometer (at a fixed phase of the Mach-Zehnder interferometer). The visibility of the interference fringes is 72.3±1.2 %.

expected coherence time is now limited by the phase-matching bandwidth of the nonlinear crystal, yielding a coherence time of ≈ 1.4 ps (corresponding to a coherence length of 0.4 mm). For the Franson interference experiment we set up two interferometers: In the idler arm (1411 nm) a fiber-based Mach-Zehnder interferometer with a fixed delay of 1.14 ns is inserted. The phase is fine-tuned via a fiber-based phase shifter in one arm. In the signal arm (854 nm), we use the free-space Michelson interferometer already mentioned in the main text. The maximum visibility of the Franson interference appears if both interferometers are equally unbalanced. Therefore, the delay of the Michelson interferometer is also set to 1.14 ns. In coincidence detection of the interferometer outputs the typical 3–peak–structure with a peak separation of 1.14 ns and a peak width of 1 ps (broadened by detection jitter to ≈ 500 ps) appears. Scanning one of the interferometers (here the Michelson interferometer) yields oscillations of the central correlation peak height, i.e. the coincidence rate, giving rise to interference fringes. Fig. 9 shows these Franson interference fringes with a visibility of $72.3 \pm 1.2\%$ (with background subtraction: 75.2±1.2%). The background-corrected visibility is close to the maximum possible value of 76.5%, which is determined by the product of the single photon interference visibilities (90% for the fiber interferometer, 85% for the Michelson interferometer). This result is a clear signature of energy-time entanglement of our photon pairs. If one repeated this experiment with filtered photons, as used in the heralded absorption experiments, one would expect a larger coherence time but the same visibility. Thus, we can safely assume that also the filtered photons show energy-time entanglement.

ACKNOWLEDGMENTS

The work was funded by the German Federal Ministry of Science and Education (BMBF) within the projects "Q.com-Q" (contract No. 16KIS0127) and "QSCALE" (contract No. 01BQ1107). J. Brito acknowledges support by CONICYT.

[1] H. J. Kimble, "The quantum internet", Nature **453**, 1023 (2008).
[2] L.-M. Duan, C. Monroe, "Quantum networks with trapped ions", Rev. Mod. Phys. **82**, 1209-1224 (2010).
[3] S. Zaske, A. Lenhard, C. A. Keßler, J. Kettler, C. Hepp, C. Arend, R. Albrecht, W.-M. Schulz, M. Jetter, P. Michler, and C. Becher, "Visible-to-Telecom Quantum Frequency Conversion of Light from a Single Quantum Emitter," Phys. Rev. Lett. **109**, 147404 (2012).
[4] C. Clausen, F. Bussières, A. Tiranov, H. Herrmann, C. Silberhorn, W. Sohler, M. Afzelius, and N. Gisin, "A source of polarization-entangled photon pairs interfacing quantum memories with telecom photons", New J. Phys. **16**, 093058 (2014).
[5] E. Saglamyurek, J. Jin, V. B. Verma, M. D. Shaw, F. Marsili, S. W. Nam, D. Oblak, and W. Tittel, "Quantum storage of entangled telecom-wavelength photons in an erbium-doped optical fibre", Nature Photonics **9**, 83 (2015).
[6] J. Fekete, D. Rieländer, M. Cristiani, and H. de Riedmatten, "Ultranarrow-Band Photon-Pair Source Compatible with Solid State Quantum Memories and Telecommunication Networks," Phys. Rev. Lett. **110**, 220502 (2013).
[7] S. Fasel, O. Alibart, S. Tanzilli, P. Baldi, A. Beveratos, N. Gisin, and H. Zbinden, "High-quality asynchronous heralded single-photon source at telecom wavelength," New J. Phys. **6**, 163 (2004).
[8] E. Pomarico, B. Sanguinetti, T. Guerreiro, R. Thew, and H. Zbinden, "MHz rate and efficient synchronous heralding of single photons at telecom wavelengths", Optics Express, **20**, 23846.
[9] X.-H. Bao, Y. Qian, J. Yang, H. Zhang, Z.-B. Chen, T. Yang, and J.-W. Pan, "Generation of Narrow-Band Polarization-Entangled Photon Pairs for Atomic Quantum Memories," Phys. Rev. Lett. **101**, 190501 (2008).
[10] A. Haase, N. Piro, J. Eschner, and M. W. Mitchell, "Tunable narrowband entangled photon pair source for resonant single-photon single-atom interaction," Opt. Lett. **34**, 55-57 (2009).
[11] M. Scholz, L. Koch, R. Ullmann, and O. Benson, "Single-mode operation of a high-brightness narrow-band single-photon source", Appl. Phys. Lett. **94**, 201105 (2009).
[12] F. Wolfgramm, Y. A. de Icaza Astiz, F. A. Beduini, A. Cer, and M. W. Mitchell, "Atom-Resonant Heralded Single Photons by Interaction-Free Measurement," Phys. Rev. Lett. **106**, 053602 (2011).
[13] F. Steinlechner, P. Trojek, M. Jofre, H. Weier, D. Perez, T. Jennewein, R. Ursin, J. Rarity, M. W. Mitchell, J.

P. Torres, H. Weinfurter, and V. Pruneri, "A high-brightness source of polarization-entangled photons optimized for applications in free space", Optics Express **20**, 9640.
[14] E. Pomarico, B. Sanguinetti, N. Gisin, R. Thew, H. Zbinden, G. Schreiber, A. Thomas, and W. Sohler, "Waveguide-based OPO source of entangled photon pairs," New J. Phys. **11**, 113042 (2009).
[15] S. Krapick, H. Herrmann, V. Quiring, B. Brecht, H. Suche, and Ch. Silberhorn, "An efficient integrated two-color source for heralded single photons," New J. Phys. **15**, 033010 (2013).
[16] N. Piro, A. Haase, M. Mitchell and J. Eschner, "An entangled photon source for resonant single-photon single-atom interaction", J. Phys. B: At. Mol. Opt. Phys. **42**, 114002 (2009).
[17] Z. Y. Ou, and Y. J. Lu, "Cavity Enhanced Spontaneous Parametric Down-Conversion for the Prolongation of Correlation Time between Conjugate Photons," Phys. Rev. Lett. **83**, 2556-2559 (1999).
[18] M. Scholz, F. Wolfgramm, U. Herzog and O. Benson, "Narrow-band single photons from a single-resonant optical parametric oscillator far below threshold", Appl. Phys. Lett. **91**, 191104 (2007)
[19] F. Monteiro, A. Martin, B. Sanguinetti, H. Zbinden, and R. T. Thew, "Narrowband photon pair source for quantum networks", Opt. Express **22**, 4371 (2014).
[20] D. Rieländer, K. Kutluer, P. M. Ledingham, M. Gündogan, J. Fekete, M. Mazzera, and H. de Riedmatten, "Quantum Storage of Heralded Single Photons in a Praseodymium-Doped Crystal," Phys. Rev. Lett. **112**, 040504 (2014).
[21] T. Chanelière, D.N. Matsukevich, S.D. Jenkins, T.A.B. Kennedy, M.S. Chapman, and A. Kuzmich, "Quantum Telecommunication Based on Atomic Cascade Transitions", Phys. Rev. Lett. **96**, 093604 (2006).
[22] P. Schindler, D. Nigg, T. Monz, J. T. Barreiro, E. Martinez, S. X. Wang, S. Quint, M. F. Brandl, V. Nebendahl, C. F. Roos, M. Chwalla, M. Hennrich, and R. Blatt, "A quantum information processor with trapped ions," New J. Phys. **15**, 123012 (2013).
[23] N. Piro, F. Rohde, C. Schuck, M. Almendros, J. Huwer, J. Ghosh, A. Haase, M. Hennrich, F. Dubin, J. Eschner, "Heralded single-photon absorption by a single atom", Nat. Phys. **7**, 17-20 (2011).
[24] J. Huwer, J. Ghosh, N. Piro, M. Schug, F. Dubin and J. Eschner, "Photon entanglement detection by a single atom", New J. Phys. **15**, 025033 (2013).
[25] A. Stute, B. Casabone, P. Schindler, T. Monz, P. O. Schmidt, B. Brandstätter, T. E. Northup, and R. Blatt, "Tunable ion-photon entanglement in an optical cavity", Nature **485**, 482 (2012).
[26] C. Kurz, M. Schug, P. Eich, J. Huwer, P. Müller and J. Eschner, "Experimental protocol for high-fidelity heralded photon-to-atom quantum state transfer", Nat. Commun. **5**, 5527 (2014).
[27] B. Casabone, K. Friebe, B. Brandstätter, K. Schüppert, R. Blatt, and T. E. Northup, "Enhanced quantum interface with collective ion-cavity coupling", Phys. Rev. Lett. **114**, 023602 (2015).
[28] D. L. Moehring, P. Maunz, S. Olmschenk, K. C. Younge, D. N. Matsukevich, L.-M. Duan and C. Monroe, "Entanglement of single-atom quantum bits at a distance", Nature **449**, 68 (2007).
[29] M. Schug, J. Huwer, C. Kurz, P. Müller, J. Eschner, "Heralded Photonic Interaction between Distant Single Ions", Phys. Rev. Lett. **110**, 213603 (2013).
[30] D. Hucul, I. V. Inlek, G. Vittorini, C. Crocker, S. Debnath, S. M. Clark, and C. Monroe, "Modular entanglement of atomic qubits using photons and phonons," Nature Phys. **11**, 37-42 (2015).
[31] S. Zaske, A. Lenhard, C. Becher, "Efficient frequency downconversion at the single photon level from the red spectral range to the telecommunications C-band", Optics Exp. **19**, 12825-12836 (2011).
[32] S. Zaske, D.-H. Lee, and C. Becher, "Green-pumped cw singly resonant optical parametric oscillator based on MgO:PPLN with frequency stabilization to an atomic resonance," Appl. Phys. B **98**, 729-735 (2010).
[33] C. Matthiesen, A. N. Vamivakas, M. Atatüre, "Subnatural Linewidth Single Photons from a Quantum Dot", Phys. Rev. Lett. **108**, 093602 (2012).
[34] A. Ulhaq, S. Weiler, S. M. Ulrich, R. Roßbach, M. Jetter, P. Michler, "Cascaded single-photon emission from the Mollow triplet sidebands of a quantum dot", Nat. Phot. **6**, 238-242 (2012).
[35] C. Clausen, I. Usmani, F. Bussieres, N. Sangouard, M. Afzelius, H. de Riedmatten, N. Gisin, "Quantum storage of photonic entanglement in a crystal", Nature **469**, 508 (2011).
[36] U. Herzog, M. Scholz, O. Benson, "Theory of biphoton generation in a single-resonant optical parametric oscillator far below threshold", Phys. Rev. A **77**, 023826 (2008).
[37] N. Piro and J. Eschner, "Single photon absorption by a single atom: from heralded absorption to polarization state mapping", in *Engineering the Atom-Photon Interaction*, edited by A. Predojević and M.W. Mitchell (Springer, Cham, 2015), ch. 5.
[38] J. Jin, and D. A. Church, "Precision Lifetimes for the Ca^+ 4p ^{2}P Levels: Experiment Challenges Theory at the 1 % Level," Phys. Rev. Lett. **70**, 3213-3216 (1993).
[39] N. Kalb, A. Reiserer, S. Ritter, and G. Rempe, "Heralded Storage of a Photonic Quantum Bit in a Single Atom," Phys. Rev. Lett. **114**, 220501 (2015).
[40] H. M. Meyer, R. Stockill, M. Steiner, C. Le Gall, C. Matthiesen, E. Clarke, A. Ludwig, J. Reichel, M. Atatüre, and M. Köhl, "Direct Photonic Coupling of a Semiconductor Quantum Dot and a Trapped Ion," Phys. Rev. Lett. **114**, 123001 (2015).
[41] S. A. Aljunid, G. Maslennikov, Y. Wang, H. L. Dao, V. Scarani, and C. Kurtsiefer, "Excitation of a Single Atom with Exponentially Rising Light Pulses," Phys. Rev. Lett. **111**, 103001 (2013).
[42] W. Tittel, J. Brendel, H. Zbinden, and N. Gisin, "Quantum Cryptography Using Entangled Photons in Energy-Time Bell States," Phys. Rev. Lett. **84**, 4737 (2000).
[43] Z. Zhang, J. Mower, D. Englund, F. N.C. Wong, and J. H. Shapiro, "Unconditional Security of Time-Energy Entanglement Quantum Key Distribution Using Dual-Basis Interferometry," Phys. Rev. Lett. **112**, 120506 (2014).
[44] J. D. Franson, "Bell inequality for position and time", Phys. Rev. Lett. **62**, 2205 (1989).

Bibliography

[1] A. Einstein, B. Podolsky, N. Rosen. *Can quantum-mechanical description of physical reality be considered complete?* Phys. Rev. A **47**, 777 (1935).

[2] J. Bell. *On the Einstein-Podolsky-Rosen paradox*. Physics **1**, 195 (1964).

[3] R. Feynmann. *Simulating physics with computers*. International Journal of Theoretical physics **21**, 6 (1982).

[4] B. Schumacher. *Quantum coding*. Phys. Rev. A **51**, 4 (1995).

[5] H. Kimble. *The Quantum Internet*. Nature **453**, 1023 (2008).

[6] P. Shor. *Algorithms for quantum computation: Discrete logarithms and factoring*. Proceedings of the 35th Annual Symposium on Foundations of Computer Science **124** (1994).

[7] D. DiVincenzo. *The physical implementation of quantum computation*. Fortschritte der Physik **489**, 9 (2000).

[8] W. Wootters, W. Zurek. *A single quantum cannot be cloned*. Nature **299**, 802 (1982).

[9] N. Sangouard, C. Simon, H. de Riedmatten, N. Gisin. *Quantum repeaters based on atomic ensembles and linear optics.* Rev. Mod. Phys. **83**, 33 (2011).

[10] L. Duan, M. Lukin, J. Cirac, P. Zoller. *Long-distance quantum communication with atomic ensembles and linear optics*. Nature **414**, 413 (2001).

[11] N. Sangouard, C. Simon, J. Minar, H. Zbinden, H. de Riedmatten, N. Gisin. *Analysis of a quantum memory for photons based on controlled reversible inhomogeneous broadening*. Phys. Rev. A (2007).

[12] C. Simon, H. de Riedmatten, M. Afzelius, N. Sangouard, H. Zbinden, N. Gisin. *Quantum Repeaters with Photon Pair Sources and Multimode Memories*. Phys. Rev. Lett. **98**, 190503 (2007).

[13] M. Lettner, M. Mücke, S. Riedl, C. Vo, C. Hahn, S. Baur, J. Bochmann, S. Ritter, S. Dürr, G. Rempe. *Remote Entanglement between a Single Atom and a Bose-Einstein Condensate*. Phys. Rev. Lett. **106**, 210503 (2011).

[14] S. Ritter, C. Nölleke, C. Hahn, A. Reiserer, A. Neuzner, M. Uphoff, M. Mücke, E. Figueroa, J. Bochmann, G. Rempe. *An elementary quantum network of single atoms in optical cavities*. Nature **484**, 195 (2012).

[15] S. Tanzilli, W. Tittel, M. Halder, O. Alibart, P. Baldi, N. Gisin, H. Zbinden. *A photonic quantum information interface*. Nature **437**, 1 (2005).

[16] F. Bussieres, C. Clausen, A. Tiranov, B. Korzh, V. B. Verma, S. W. Nam, F. Marsili, A. Ferrier, P. Goldner, H. Herrmann, C. Silberhorn, W. Sohler, M. Afzelius, N. Gisin. *Quantum teleportation from a telecom-wavelength photon to a solid-state quantum memory*. Nature Photon. **8**, 775–778 (2014).

[17] B. Albrecht, P. Farrera, X. Fernandez-Gonzalvo, M. Cristiani, H. de Riedmatten. *A waveguide frequency converter connecting Rubidium-based quantum memories to the telecom C-band*. Nature Commun. **5**, 3376 (2014).

[18] C. Schuck, F. Rohde, N. Piro, M. Almendros, J. Huwer, M. Mitchell, M. Hennrich, A. Haase, F. Dubin, J. Eschner. *Resonant interaction of a single atom with single photons from a down-conversion source*. Phys. Rev. A **81**, 011802 (2010).

[19] N. Piro, F. Rohde, C. Schuck, M. Almendros, J. Huwer, J. Ghosh, A. Haase, M. Hennrich, F. Dubin, J. Eschner. *Heralded single-photon absorption by a single atom*. Nat. Phys. **7**, 17 (2011).

[20] N. Piro. *Controlled absorption of heralded single photons by a single atom: Towards entanglement distribution in quantum networks*. Ph.D. thesis, ICFO - The Institute of Photonic Scienes Universidad politecnica de Catalunya (2010).

[21] J. Huwer, J. Ghosh, N. Piro, M. Schug, F. Dubin, J. Eschner. *Photon entanglement detection by a single atom*. New J. Phys. **15**, 025033 (2013).

[22] J. Huwer. *Experimental tools for quantum networking operations with single photons and single ions*. Ph.D. thesis, Universidad Politecnica de Catalunya - ICFO/ Universität des Saarlandes (2013).

[23] M. Almendros, J. Huwer, N. Piro, F. Rohde, C. Schuck, M. Hennrich, F. Dubin, J. Eschner. *Bandwidth-Tunable Single-Photon Source in an Ion-Trap Quantum Network*. Phys. Rev. Lett. **103**, 213601 (2009).

[24] C. Kurz, J. Huwer, M. Schug, P. Müller, J. Eschner. *A high-rate source for single photons in a pure quantum state*. New J. Phys. **15**, 055005 (2013).

[25] M. Schug, J. Huwer, C. Kurz, P. Müller, J. Eschner. *Heralded Photonic Interaction between Distant Single Ions*. Phys. Rev. Lett. **11**, 213603 (2013).

[26] C. Kurz. *Quantum networking with single ions and single photons interfaced in free space*. Ph.D. thesis, Universität des Saarlandes (2015).

[27] M. Schug. *Single photons from single ions: quantum interference and distant ion interaction*. Ph.D. thesis, Universität des Saarlandes (2015).

[28] P. Müller et al. *Measurement of the scattering phase of a single (spontaneous) Raman photon.* In preparation (2016).

[29] L. M. Duan, C. Monroe. *Quantum networks with trapped ions*. Rev. Mod. Phys. **82**, 1209 (2010).

[30] C. Kurz, M. Schug, P. Eich, J. Huwer, P. Müller, J. Eschner. *Experimental protocol for high-fidelity heralded photon-to-atom quantum state transfer*. Nature Commun. **5**, 5527 (2014).

[31] C. Chou, D. Hume, J. Koelemeij, D. Wineland, T. Rosenband. *Frequency Comparison of Two High-Accuracy Al^+ Optical Clocks*. Phys. Rev. Lett. **104**, 070802 (2010).

[32] N. Huntemann, M. Okhapkin, B. Lipphardt, S. Wyers, C. Tamm, E. Peik. *High-accuracy optical clock based on the octupole transition in* $171Yb^+$. Phys. Rev. Lett. (2012).

[33] R. Gerritsma, G. Kirchmair, F. Zähringer, E. Solano, R. Blatt, C. Roos. *Quantum simulation of the Dirac equation*. Nature **463**, 68 (463).

[34] S. Gulde et al. *Implementation of the Deutsch-Jozsa algorithm on an ion trap quantum computer*. Nature **421**, 48 (2003).

[35] R. Blatt, C. Roos. *Quantum simulation with trapped Ions*. Nat. Phys. **8**, 277 (2012).

[36] H. Häffner, C. Roos, R. Blatt. *Quantum computing with trapped ions*. Physics Reports **469**, 4 (2008).

[37] P. Schindler, D. Nigg, T. Monz, J. T. Barreiro, E. Martinez, S. X. Wang, S. Quint, M. Brandl, V. Nebendahl, C. Roos, M. Chwalla, M. Hennrich, R. Blatt. *A quantum information processor with trapped ions*. New J. Phys. **15**, 123012 (2013).

[38] J. Cirac, P. Zoller. *Quantum computations with cold trapped ions*. Phys. Rev. Lett. **74**, 20 (1995).

[39] W. Paul. *Nobel Lecture: Electromagnetic Traps for Charged and Neutral Particles* (1989).

[40] H. Naegerl, C. Roos, H. Rohde, D. Leibfriedm, J. Eschner, F. Schmidt-Kaler, R. Blatt. *Addressing and ccoolin of single ions in Paul Traps*. Fortschr. Phys. **48**, 623 (2000).

[41] P. Ghosh. *Ion Traps*. Oxford University Press (1995).

[42] J. Eschner, G. Morigi, F. Schmidt-Kaler. *Laser cooling of trapped Ions*. J. Opt. Soc. B **20**, 5 (2003).

[43] F. Rohde. *Remotete ion traps for quantum networking*. Ph.D. thesis, ICFO - The Institute of Photonic Sciences - Universidad politecnica de Catalunya (2009).

[44] M. Almendros. *Towards long-distance quantum communication*. Ph.D. thesis, ICFO - The Institute of Photonic Scienes - Universidad politecnica de Catalunya (2009).

[45] D. Magde, H. Mahr. *Study in ammonium dihydrogen phosphate of spontaneous paremetric interaction tunable from 4400 to 16000 A*. Phys. Rev. Lett. **18**, 905 (1967).

[46] P. Kwiat, A. M. Steinberg, R. Chiao. *High-visibility interference in a Bell-inequality experiment for energy and time*. Phys. Rev. A **47**, 4 (1993).

[47] P. Kwiat et al. *New high-intensity source of polarization entangled photons pairs*. Phys. Rev. Lett. **75**, 4337 (1995).

[48] J. Armstrong, N. Bloembergen, J. Ducuing, P. Pershan. *Interactions between light waves in a nonlinear dielectric*. Phys. Rev. A **127**, 6 (1962).

[49] Z. Ou. *Multi-photon quantum interference*. Springer Science Business media (2007).

[50] M. Förtsch, J. Fürst, C. Wittmann, D. Strekalov, A. Aiello, M. Chekhova, C. Silberhorn, G. Leuchs, C. Marquardt. *A versatile source of single photons for quantum information processing*. Nat. Commun. **4**, 1818 (2013).

[51] S. Fasel, O. Alibart, S. Tanzilli, P. Baldi, A. Beveratos, N. Gisin, H. Zbinden. *High-quality asynchronous heralded single-photon source at telecom wavelength*. New J. Phys. **6**, 163 (2004).

[52] A. Haase, N. Piro, J. Eschner, M. Mitchell. *Tunable narrowband entangled photon pair source for resonant single-photon single-atom interaction*. Opt. Lett. **34**, 1 (2009).

[53] N. Piro, A. Haase, M. Mitchell, J. Eschner. *An entangled photon source for resonant single-photon-single-atom interaction*. J. Phys. B: At. Mol. Opt. Phys. **42**, 114002 (2009).

[54] P. Müller, J. Eschner. *Single calcium-40 ion as quantum memory for photon polarization: a case study*. Appl. Phys. B **114**, 303 (2013).

[55] T. Kim, M. Fiorentino, F. Wong. *Phase-stable source of polarization-entangled photons using a polarization Sagnac interferometer*. Phys. Rev. A **73**, 012316 (2006).

[56] J. Franson. *Bell inequality for position and time*. Phys. Rev. Lett. **62**, 19 (1989).

[57] B. Brecht, A. Eckstein, A. Christ, H. Suche, C. Silberhorn. *From quantum pulse gate to quantum pulse shaper - engineered frequency conversion in nonlinear optical waveguides*. New J. Phys. **13**, 065029 (2011).

[58] A. Lenhard. *Quantum Photonic Interfaces between Atomic and Telecommunication Wavelengths*. Ph.D. thesis, Universität des Saarlandes (2015).

[59] Y. Nishida, H. Miyazawa, M. Asobe, O. Tadanaga, H. Suzuki. *Direct-bonded QPM-LN ridge waveguide with high damage resistance at room temperature*. Electr. Lett. **39**, 609–611 (2003).

[60] A. D. Boozer, A. Boca, R. Miller, T. E. Northup, H. Kimble. *Reversible State Transfer between Light and a Single Trapped Atom*. Phys. Rev. Lett. **98**, 193601 (2007).

[61] C. Langer et al. *Long-Lived Qubit Memory Using Atomic Ions*. Phys. Rev. Lett. **95**, 060502 (2005).

[62] A. Stute, B. Casabone, P. Schindler, T. Monz, P. O. Schmidt, B. Brandstätter, T. E. Northup, R. Blatt. *Tunable ion-photon entanglement in an optical cavity*. Nature **485**, 482 (2012).

[63] D. Hucul, I. Inlek, G. Vittorini, C. Crocker, S. Debnath, S. Clark, C. Monroe. *Modular entanglement of atomic qubits using photons and phonons*. Nat. Phys. **11**, 37 (2014).

[64] M. Moehring, P. Maunz, S. Olmschenk, K. C. Younge, D. N. Matsukevich, L. Duan, C. Monroe. *Entanglement of single-atom quantum bits at a distance*. Nature **44910**, 68 (2007).

[65] B. Weber, H. P. Specht, T. Müller, J. Bochmann, M. Mücke, D. L. Moehring, G. Rempe. *Photon-Photon Entanglement with a Single Trapped Atom*. Phys. Rev. Lett. **102**, 030501 (2009).

[66] N. Kalb, A. Reiserer, S. Ritter, G. Rempe. *Heralded Storage of a Photonic Quantum Bit in a Single Atom*. Phys. Rev. Lett. **114**, 220501 (2015).

[67] S. Lloyd, M. S. Shahriar, J. H. Shapiro, P. R. Hemmer. *Long distance, unconditional teleportation of atomic states via complete Bell state measurements*. Phys. Rev. Lett. **87**, 167903 (2001).

[68] N. Sangouard, J.-D. Bancal, P. Müller, J. Ghosh, J. Eschner. *Heralded mapping of photonic entanglement into single atoms in free space: proposal for a loophole-free Bell test*. New J. Phys. **15**, 085004 (2013).

[69] J. Brito, S. Kucera, P. Eich, P. Müller, J. Eschner. *Doubly-heralded single-photon absorption by a single atom*. Accepted for publication in Appl. Phys. B (2016).

[70] F. Rohde, M. Almendros, C. Schuck, J. Huwer, M. Hennrich, J. Eschner. *A diode laser stabilization scheme for $^{40}Ca^{+}$ single-ion spectroscopy*. J. Phys. B: At. Mol. Opt. Phys. **43**, 115401 (2010).

[71] F. Wolfgramm, Y. A. de Icaza Astiz, F. Beduini, A. Cere, M. Mitchell. *Atom-Resonant Heralded Single Photons by Interaction-Free Measurement*. Phys. Rev. Lett. **106**, 053602 (2011).

[72] C. Clausen, F. Bussieres, H. Herrmann, C. Silberhorn, W. Sohler, M. Afzelius, N. Gisin. *A source of polarization-entangled photon pairs interfacing quantum memories with telecom photons*. J. Phys. **16**, 093058 (2014).

[73] B. Lauritzen, J. Minár, H. de Riedmatten, M. Afzelius, N. Sangouard, C. Simon, N. Gisin. *Telecommunication-Wavelength Solid-State Memory at the Single Photon Level*. Phys. Rev. Lett. **104**, 080502 (2010).

[74] A. Lenhard, M. Bock, C. Becher, S. Kucera, J. Brito, P. Eich, P. Müller, J. Eschner. *Telecom-heralded single photon absorption by a single atom.* Phys. Rev. A **92**, 063827 (2015).

[75] E. Saglamyurek, J. Jin, V. Verma, M. Shaw, F. Marsili, W. N. S., W. Oblak, D.and Tittel. *Quantum storage of entangled telecom-wavelength photons in an erbium-doped optical fibre*. Nature Photonics **8**, 83–87 (2015).

[76] A. G. Radnaev, Y. O. Dudin, R. Zhao, H. H. Jen, S. D. Jenkins, A. Kuzmich, T. A. B. Kennedy. *A quantum memory with telecom-wavelength conversion*. Nat. Phys. **6**, 894 (2010).

[77] M. T. Rakher, L. Ma, O. Slattery, X. Tang, K. Srinivasan. *Quantum transduction of telecommunicationsband single photons from a quantum dot by frequency upconversion*. Nat. Photon. **4**, 786–791 (2010).

[78] S. Zaske, A. Lenhard, C. A. Kessler, J. Kettler, C. Hepp, C. Arend, R. Albrecht, W. Schulz, M. Jetter, P. Michler, C. Becher. *Visible-to-Telecom Quantum Frequency Conversion of Light from a Single Quantum Emitter*. Phys. Rev. Lett. **109**, 147404 (2012).

[79] X. Fernandez-Gonzalvo, G. Corrielli, B. Albrecht, M. Grimau, M. Cristiani, H. de Riedmatten. *Quantum frequency conversion of quantum memory compatible photons to telecommunication wavelengths*. Opt. Express **21**, 17 (2013).

[80] N. Maring, K. Kutluer, J. Cohen, M. Cristiani, M. Mazzera, P. Ledingham, H. de Riedmatten. *Storage of up-converted telecom photons in a doped crystal*. New J. Phys. **16**, 113021 (2014).

[81] K. De Greve, L. Yu, P. L. McMahon, J. S. Pelc, C. M. Natarajan, N. Young Kim, E. Abe, S. Maier, C. Schneider, M. Kamp, R. H. Höfling, S. Hadfield, A. Forchel, M. M. Fejer, Y. Yamamoto. *Quantum-dot spin-photon entanglement via frequency downconversion to telecom wavelength*. Nature **491**, 421 (2012).

[82] K. De Greve, P. L. McMahon, L. Yu, J. S. Pelc, C. Jones, C. M. Natarajan, N. Young Kim, E. Abe, S. Maier, C. Schneider, M. Kamp, R. H. Höfling, S. Hadfield, A. Forchel, M. M. Fejer, Y. Yamamoto. *Complete tomography of a high-fidelity solid-state entangled spin-photon qubit pair*. Nat. Commun **4**, 2228 (2013).

[83] J. Brito, A. Lenhard, S. Kucera, P. Müller, P. Eich, C. Becher, J. Eschner. *Quantum frequency conversion for an atom-photon based quantum network*. In preparation (2016).

[84] A. Lenhard, J. Brito, M. Bock, J. Eschner, C. Becher. *Coherence and Entanglement Preservation of Frequency-Converted Heralded Single Photons*. In preparation (2016).

[85] A. Lenhard, J. Brito, S. Kucera, M. Bock, J. Eschner, C. Becher. *Single telecom photon heralding by wavelength multiplexing in an optical fiber*. Appl. Phys. B **122**, 20 (2016).

[86] S. Ramelow, A. Fedrizzi, A. Poppe, N. K. Langford, A. Zeilinger. *Polarization-entanglement-conserving frequency conversion of photons*. Phys. Rev. A **85**, 013845 (2012).

[87] P. Kwiat. *Non-classical effects from spontaneous parametric down-conversion*. Ph.D. thesis, University of California (1993).

[88] J. Franson. *Violations of a simple inequality for classical field*. Phys. Rev. Lett. **67**, 3 (1991).

[89] W. Tittel, J. Brendel, N. Gisin, H. Zbinden. *Long-distance Bell-type tests using energy-time entangled photons*. Phys. Rev. A **59**, 4150 (1999).

[90] M. Eisaman, J. Fan, A. Migdall, S. Polyakov. *Single-photon sources and detectors*. Rev. Sci. Inst. **82**, 071101 (2011).

[91] I. Blauensteiner, B. Herbauts, S. Bettelli, A. Poppe, H. Hübel. *Photon bunching in parametric down-conversion with continuous-wave excitation*. Phys. Rev. A **79**, 063846 (2009).

[92] A. Christ, C. Silberhorn. *Limits on the deterministic creation of pure single-photon states using parametric down-conversion*. Phys. Rev. A **85**, 023829 (2012).

[93] B. Lounis, M. Orrit. *Single-photon sources*. Rep. Prog. Phys. **68**, 2005 (2005).

[94] M. Bock. *Aufbau und charakterisierung einer SPDC Photonenpaarquelle*. Master's thesis, Universität des Saarlandes (2014).

[95] S. Krapick, H. Herrmann, V. Quiring, B. . Brecht, H. Suche, C. Silberhorn. *An efficient integrated two-color source for heralded single photons*. New J. Phys. **15**, 033010 (2013).

[96] C. Bennett, G. Brassard. *Quantum cryptography: Public key distribution and coin tossing*. Proceedings of IEEE International Conference on Computers, Systems and Signal Processing **175**, 8 (1984).

[97] D. Bouwmeester, J.-W. Pan, K. Mattle, M. Eibl, H. Weinfurter, A. Zeilinger. *Experimental quantum teleportation*. Nature **390**, 575 (1997).

[98] F. Wolfgramm, X. Xing, A. Cerè, A. Predojevic, A. M. Steinberg, M. W. Mitchell. *Bright filter-free source of indistinguishable photon pairs*. Opt. Express **16**, 22 (2008).

[99] M. Steiner, H. M. Meyer, J. Reichel, M. Köhl. *Photon Emission and Absorption of a Single Ion Coupled to an Optical-Fiber Cavity*. Phys. Rev. Lett. **113**, 263003 (2014).

[100] H. de Riedmatten, I. Marcikic, J. van Houwelingen, W. Tittel, H. Zbinden, N. Gisin. *Long-distance entanglement swapping with photons from separated sources*. Phys. Rev. A **71**, 050302 (2005).

[101] N. Sangouard, C. Simon, B. Zhao, Y. Chen, H. de Riedmatten, J.-W. Pan, N. Gisin. *Robust and efficient quantum repeaters with atomic ensembles and linear optics*. Phys. Rev. A **77**, 062301 (2008).

[102] N. Sinclair et al. *Spectral Multiplexing for Scalable Quantum Photonics using an Atomic Frequency Comb Quantum Memory and Feed-Forward Control*. Phys. Rev. Lett. **113**, 053603 (2014).

[103] H. Krovi et al. *Practical Quantum Repeaters with Parametric Down-Conversion Sources*. ArXiv 1505.03470v1 (2015).

[104] C. Howson, P. Urbach. *Scientific Reasoning: The Bayesian Approach*. Open Court Publishing company (2005).

[105] J. R. D. Fekete, M. Cristiani, H. de Riedmatten. *Ultranarrow-Band Photon-Pair Source Compatible with Solid State Quantum Memories and Telecommunication Networks*. Phys. Rev. Lett. **110**, 220502 (2013).

[106] X.-H. Bao, Y. Qian, J. Yang, H. Zhang, Z.-B. Chen, T. Yang, J.-W. Pan. *Generation of Narrow-Band Polarization-Entangled Photon Pairs for Atomic Quantum Memories*. Phys. Rev. Lett. **101**, 190501 (2008).

[107] K. Choi, H. Deng, J. Laurat, H. Kimble. *Mapping photonic entanglement into and out of a quantum memory*. Nature **452**, 6 (2008).

[108] K. Reim, P. Michelberger, K. Lee, J. Nunn, N. Langford, I. Walmsley. *Single-photon-level qunatum memory at room temperature*. Phys. Rev. Lett. **107**, 053603 (2011).

[109] R. Ikuta, Y. Kusaka, T. Kitano, H. Kato, T. Yamamoto, M. Koashi, N. Imoto. *Wide-band quantum interface for visible-to-telecommunication wavelength conversion*. Nature Commun. **2**, 537 (2011).

[110] B. Casabone, V. Friebe, B. Brandstätter, K. Schüppert, R. Blatt, T. E. Northup. *Enhanced Quantum Interface with Collective Ion-Cavity Coupling*. Phys. Rev. Lett. **114**, 023602 (2015).

[111] S. Tanzilli, H. de Riedmatten, W. Tittel, H. Zbinden, P. Baldi, M. de Micheli, D. Ostrowsky, N. Gisin. *Highly efficient photon-pair source using periodically poled lithium niobate waveguide*. Electr. Lett. **37**, 28 (2001).

[112] K. Sanaka, K. Kawahara, T. Kuga. *New High-Efficiency Source of Photon Pairs for Engineering Quantum Entanglement*. Phys. Rev. Lett. **86**, 5620 (2001).

[113] K. Banaszek, A. U'ren, I. Walmsley. *Generation of correlated photons in controlled spatial modes by downconversion in nonlinear waveguides*. Opt. Lett. **26**, 1367 (2001).

[114] A. U'ren, C. Silberhorn, K. Banaszek, I. Walmsley. *Efficient Conditional Preparation of High-Fidelity Single Photon States for Fiber-Optic Quantum Networks*. Phys. Rev. Lett. **93**, 093601 (2004).

[115] M. Fiorentino, S. Spillane, R. Beausoleil, T. Roberts, P. Battle, M. Munro. *Spontaneous Parametric Down-Conversion in periodically poled KTP waveguide and bulk crystals*. Opt. Express **15**, 12 (2007).

[116] T. Zhong, F. Wong, T. Roberts, P. Battle. *High performance photon-pair source based on a fiber-coupled peridocally poled KTiOPO waveguide*. Opt Express **17**, 14 (2009).

[117] S. Tanzilli, A. Martin, F. Kaiser, M. De Micheli, O. Alibart, D. Ostrowsky. *On the genesis and evolution of integrated quantum optics*. Laser & Photonics Reviews **6**, 115 (2012).

[118] T. Suhara, M. Fujimura. *Waveguide nonlinear-optics devices*. Springer (2003).

[119] L. Helt, M. Liscidini, J. Sipe. *How does it scale? Comparing quantum and classical nonlinear optical processes in integrated devices*. J. Opt. Soc. B. **29**, 8 (2012).

[120] M. Karpinski, C. Radzewicz, K. Banaszek. *Experimental characterization of three-wave mixing in a multimode nonlinear KTiOPO waveguide*. Appl. Phys. Lett, **94**, 181105 (2009).

[121] T. Zhong, F. Wong, A. Restelli, J. Bienfang. *Efficient single-spatial-mode periodically-poled KTiOPO waveguide source for high-dimensional entanglement-based quantum key distribution*. Opt. Express **20**, 24 (2012).

[122] A. Jechow, S. McNeil, C. Kaleva, D. Skoczowsky, R. Menzel. *Highly efficient single pass blue light generation at 488 nm using a PPKTP waveguide crystal and high brightness diode lasers*. Proc. of SPIE **7197**, 719707 (2009).

[123] P. Mosley, A. Christ, A. Eckstein, C. Silberhorn. *Direct Measurement of the Spatial-Spectral Structure of Waveguided Parametric Down-Conversion*. Phys. Rev. Lett. **103**, 233901 (2009).

[124] A. Ahlrichs, C. Berkemeier, B. Sprenger, O. Benson. *A monolithic polarization-independent frequency-filter system for filtering of photon pairs*. Appl. Phys. Lett. **103**, 241110 (2013).

[125] A. Eckstein, A. Christ, P. Mosley, C. Silberhorn. *Realistic g(2) measurement of a PDC source with single photon detectors in the presence of background*. Phys. Status Solidi **4**, 1216 (2011).

[126] S. Euler, M. Beier, M. Sinther, T. Walther. *Spontaneous Parametric Down-Conversion in waveguide chips for quantum information*. AIP Conf. Proc. **1363**, 323 (2010).

Acknowledgements

There are many people who have to be acknowledged at the end of a challenge like this. This work was mainly performed by a team and every contribution was really valuable to reach the results presented here.

First of all, thanks to my supervisor, Jürgen Eschner. Thanks for this opportunity and sharing your knowledge, for trusting someone coming from the other end of the world to contribute to these experiments. Although the story started in Chile[1] and involved Spain, we wind up in the welcoming grounds of the Saarland. I also thank you for your support and tolerance for my participation in external activities which have been an important part of my development as a person and scientist. Finally I thank you for your patience and contributions to our mutual understanding, despite personality, style and cultural differences. I keep for future years many things I've learned working with you.

Furthermore, I would like to thank the people I worked with operating the photon source during these years: Joyee, for your welcome at the beginning, the adventures during the move from Barcelona and moreover introducing me in the different details of the source. Stephan, who joined later, thanks for contributing with your impressive technical skills and injecting energy in moments where motivation was not the highest. Thanks also for the patience and support with my slowness at the computer. I'm certain you will succeed carrying out the projects you have in mind.

I also thank to the rest of the quantum photonics team, the ion guys were always there for pushing further our ideas for interaction experiments, most of which we carried out successfully. Michael and Christoph, with whom I shared many years of funny useless discussions and very relevant physics insights. Pascal and Philipp, for your support and contributions during the experiments and the always particular sense of humor which helped moving on during harsh times. Also Jan, for always sharing your experience and suggestions in a constructive way during the first years.

Moreover, this work would have not be the same without the collaboration with Andreas Lenhard from C. Becher's group and with whom I share many results. Thanks for the energy and patience given for carrying out all these experiments and ideas. We might have given the first steps towards major future advances in the field of quantum networks at the Saarland university. Thanks also to M. Bock for its participation and for continuing the work initiated during these years.

I have to give a special mention to Michael and Hannes for our sport adventures outside the lab: crazy ideas like singing in choirs, collecting magic mushrooms, shooting guns, hunting deers, running marathons, alpine ascents in one day or climbing protected with knots won't be forgotten so easily. Thanks for your friendship and support offered during all these years.

I want also to thank the other persons who belonged to our group during all these years and the younger members of our group: Jan, Konstantin and Matthias, I wish you success in your undergoing and future projects. A special mention is also reserved for Frau Michel, our secretary,

[1] This thesis was co-funded by a BecasChile fellowhsip, from Programa de capital humano Avanzado, Chile.

who has helped me uncountable times to solve the most unimaginable bureaucratic issues, always very willing and helpful, *vielen Dank, Frau Michel!*.

Thanks as well to Prof. Christoph Becher for allowing us to carry out this collaborative project, for his contributions to our work and the help given in the last weeks of revision.

Last but not least I want to thank all the friends who stood by me outside the lab and were like my family in Saarbrücken: Carlos, Bárbara, Emilio, Oxana, Cecilia, Beta, Mossy, Mau, Annette, Josh and John for you unconditional support, and also los montagpoleros J.D, Miguel y Fidel, gracias por la motivación a siempre ser mejor. Also to my friends from Chile, especially Alvaro, Pablo, Victoria y Carla Valentina. To all those who contributed to keep me up during these years and helped me feeling welcome in this (Saar)land: Stefan Ritz, Marc, Endre, Simon, Michi, Dominik, Lena, Sinan, Audrey, Mo, Scott and many others. Thanks very much.

The last lines I reserve for my closest circle, gracias familia: Berta, Francisco, Claudio y Gustavo, también Adriana y Nora por su apoyo incondicional, los consejos y la preocupación. Danke Julia für deine Unterstützung in den letzten Monaten, mit dir ist alles viel schöner geworden.